



**HAL**  
open science

# AGREGATION DE PROTEINES DE SOIE DANS UN ENVIRONNEMENT MICROFLUIDIQUE

Anne Martel

► **To cite this version:**

Anne Martel. AGREGATION DE PROTEINES DE SOIE DANS UN ENVIRONNEMENT MICROFLUIDIQUE. Data Analysis, Statistics and Probability [physics.data-an]. Université Joseph-Fourier - Grenoble I, 2008. English. NNT: . tel-00322259

**HAL Id: tel-00322259**

**<https://theses.hal.science/tel-00322259>**

Submitted on 17 Sep 2008

**HAL** is a multi-disciplinary open access archive for the deposit and dissemination of scientific research documents, whether they are published or not. The documents may come from teaching and research institutions in France or abroad, or from public or private research centers.

L'archive ouverte pluridisciplinaire **HAL**, est destinée au dépôt et à la diffusion de documents scientifiques de niveau recherche, publiés ou non, émanant des établissements d'enseignement et de recherche français ou étrangers, des laboratoires publics ou privés.

UNIVERSITE JOSEPH FOURIER – GRENOBLE I  
ECOLE DOCTORALE DE CHIMIE ET SCIENCES DU VIVANT  
EUROPEAN SYNCHROTRON RADIATION FACILITY

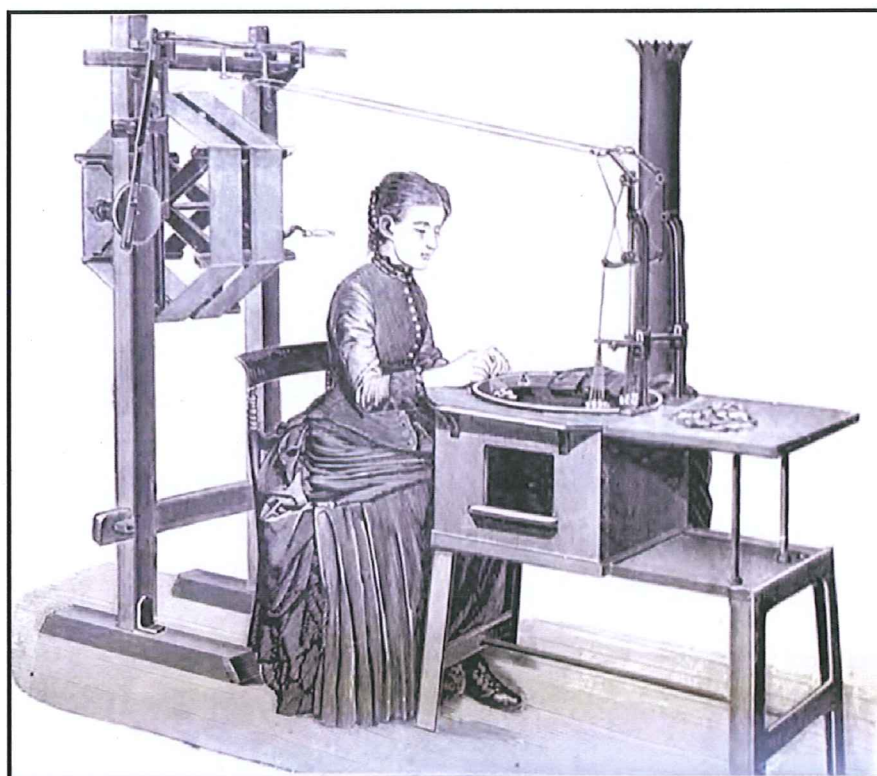
DOCTOR OF PHILOSOPHY DEGREE

Scientific field: Life Science  
Specialty: Structural Biology and Nano-Biology

Anne MARTEL

*Thesis supervised by Christian RIEKEL  
Defense on September the 10<sup>th</sup>, 2008*

## Silk Protein Aggregation in a Microfluidic Environment



### JURY:

E. PEBAY-PEYROULA	Institut de Biologie Structurale, Grenoble	Member
M. MUELLER	Institut für Experimentelle und Angewandte Physik, Kiel	Reporter
J.B. SALMON	Laboratory of Future, Bordeaux	Reporter
G. FREDDI	Stazione Sperimentale per la Seta, Milano	Member
C. RIEKEL	European Synchrotron Radiation Facility, Grenoble	Thesis Supervisor



The cover picture represents “a cocoon-reeling machine simplified and arranged for cottage use”. It comes from “*Silk: its Entomology, History and Manufacture, as exemplified at the Royal Jubilee Exhibition*”, 1887, Thomas Wardle.

---

# Aggregation of Silk Protein in a Microfluidic Environment

## Abstract:

Silk is a biopolymer spun by several arthropods. This fibre is made of protein arranged in a semi-crystalline microstructure and has remarkable mechanical properties. The main axis of this thesis work concerns the comprehension of silk fibre formation. *Bombyx mori* silk has been used as a model. The protein component of *B. mori* silk, named Fibroin, has been spun into a fibre in a microfluidic device designed to mimic the silkworm spinning apparatus. The silk formation process has been followed by synchrotron radiation scattering (SAXS and WAXS) and Raman spectroscopy. It starts with an aggregation phase. The size of aggregates is around 100 nm. Inside these particles, the Fibroin is compacted. This aggregation is followed by a phase of compaction of the aggregates. Later, within a few hours, the Fibroin undergoes a conformational transition from a mainly amorphous structure (Silk I) to the semi-crystalline structure characteristic of the natural fibre (Silk II). This process is proposed as a possible model of silk formation *in vivo*. The second axis of this work is dedicated to the investigation of the physical properties of natural *B. mori* silk. Its resistance to high temperature is studied from a molecular, structural and mechanical point of view. The semi-crystalline structure of the fibre remains stable up to carbonization although its mechanical properties and the Fibroin's integrity are affected at lower temperature. The effect of high pressure on the fibre structure is also presented : throughout the pressure increase, the crystallites can compact slightly before their disorganization.

**Keywords:** Silk, *Bombyx mori*, Fibroin, Microfluidics, X-rays scattering, Raman spectroscopy, high temperature, high pressure.

**Laboratory:** ID13, Microfocus beamline  
European Synchrotron Radiation Facility,  
6, rue Jules Horowitz, BP 220  
38043 Grenoble cedex 9  
FRANCE



UNIVERSITE JOSEPH FOURIER – GRENOBLE I  
ECOLE DOCTORALE DE CHIMIE ET SCIENCES DU VIVANT  
EUROPEAN SYNCHROTRON RADIATION FACILITY

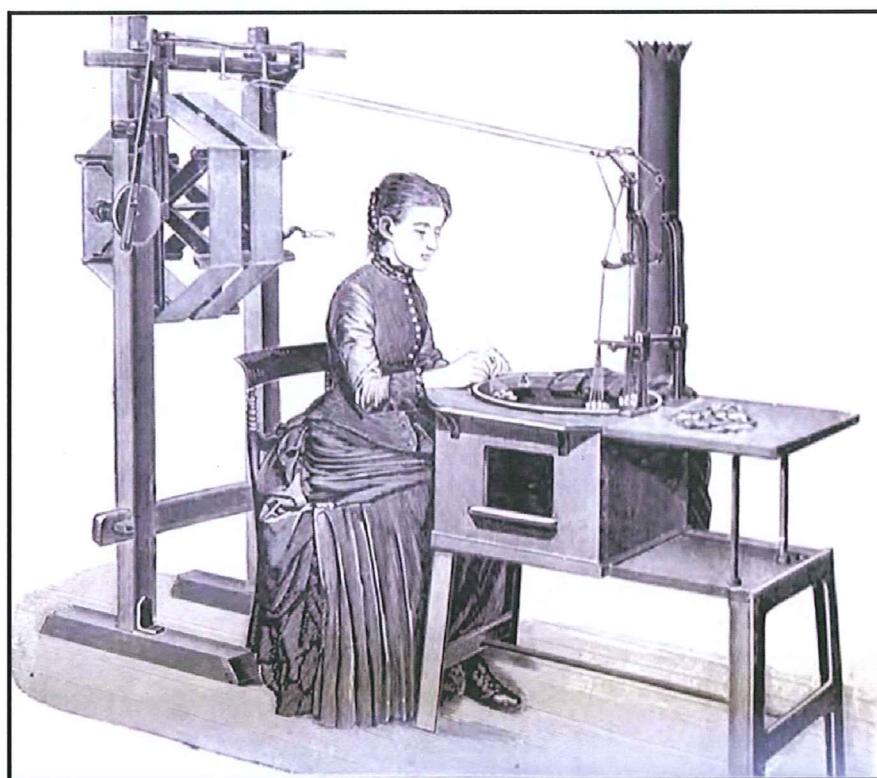
THESE DE DOCTORAT

Discipline : Sciences du Vivant  
Spécialité : Biologie Structurale et Nanobiologie

Anne MARTEL

*Thèse dirigée par Christian RIEKEL  
Soutenue le 10 septembre 2008*

## Agrégation des Protéines de Soie dans un Environnement Microfluidique



### COMPOSITION DU JURY :

E. PEBAY-PEYROULA	Institut de Biologie Structurale, Grenoble	Examineur
M. MUELLER	Institut für Experimentelle und Angewandte Physik, Kiel	Rapporteur
J.B. SALMON	Laboratory of Future, Bordeaux	Rapporteur
G. FREDDI	Stazione Sperimentale per la Seta, Milano	Examineur
C. RIEKEL	European Synchrotron Radiation Facility, Grenoble	Directeur de thèse

L'image de couverture représente "une machine à filer les cocons simplifiée et arrangée pour l'utilisation domestique". Elle est tirée du livre "*Silk: its Entomology, History and Manufacture, as exemplified at the Royal Jubilee Exhibition*", 1887, Thomas Wardle.



---

# Agrégation des Protéines de Soie dans un Environnement Microfluidique

## Résumé :

La soie est un biopolymère synthétisé par certains arthropodes. Cette fibre est constituée de protéines arrangées en une microstructure semi-cristalline et possède d'intéressantes propriétés mécaniques. L'axe principal de ce travail de thèse concerne la compréhension du processus de formation de la fibre de soie. La soie de *Bombyx mori* a été choisie comme modèle. Sa protéine, nommée Fibroïne, a été utilisée pour produire une fibre dans une cellule microfluidique construite pour mimer l'appareil de filage du ver à soie. Le processus de formation de la soie a été suivi par des techniques de diffusion des rayons X (SAXS et WAXS) et par spectroscopie Raman. Elle débute par une étape d'agrégation. La taille des agrégats est de l'ordre de 100 nm. Dans ces particules, la Fibroïne est sous une forme compactée. Cette agrégation est suivie d'une phase de compaction des agrégats. Plus tard, à une échelle de temps de quelques heures, la Fibroïne subit une transition conformationnelle depuis une structure principalement amorphe (Silk I) vers la structure caractéristique de la soie naturelle (Silk II). Ce processus est proposé comme un modèle de la formation de la fibre de soie *in vivo*. Le second axe de ce travail est orienté vers la connaissance des propriétés physiques de la soie naturelle de *B. mori*. Sa résistance aux hautes températures est étudiée d'un point de vue structural, moléculaire et mécanique. La structure semi-cristalline de la fibre demeure stable jusqu'à la carbonisation, alors même que ses propriétés mécaniques et l'intégrité de la Fibroïne sont altérées à plus basse température. L'effet des hautes pressions sur la structure de la fibre de soie est aussi présentée : tout au long de l'augmentation de pression, les cristallites se compactent légèrement avant de se désorganiser.

**Mots clés :** Soie, *Bombyx mori*, Fibroïne, Microfluidique, diffusion des rayons X, spectroscopie Raman, hautes températures, hautes pressions.

**Laboratoire :** ID13, Microfocus beamline  
European Synchrotron Radiation Facility,  
6, rue Jules Horowitz, BP 220  
38043 Grenoble cedex 9  
FRANCE

---

## Résumé Substantiel :

La soie est un biopolymère synthétisé par certains arthropodes, dont les plus connus sont les araignées et les larves de papillon. Cette fibre est constituée de protéines arrangées en une microstructure semi-cristalline, c'est-à-dire en petites cristallites incluses dans une matrice amorphe. La synthèse de ce polymère a lieu *in vivo*, ce qui implique qu'elle ne requière pas de conditions de température ou de pression élevées, et ne nécessite pas de solvants polluants, contrairement à la production de polymères synthétiques équivalents. Les propriétés mécaniques de fibre de soie allient une grande élasticité et une grande solidité. Ces propriétés en font un polymère aux applications potentielles diverses, dans le domaine médical et l'ingénierie des matériaux par exemple.

Bien que ses propriétés mécaniques soient moins attractives que celles de la soie d'araignée, la soie de *Bombyx mori* a été choisie comme modèle de ce polymère dans cette étude. Ce choix s'explique par la facilité d'obtention des protéines de soie de *B. mori* comparée aux protéines de soie d'araignée. Il est validé par la similarité de structure entre ces deux soies.

La protéine de soie de *B. mori*, nommée Fibroïne, est constituée de deux chaînes peptidiques liées par un pont disulfure. Sa structure primaire est modulaire avec des régions hautement répétitives riches en glycine et alanines, alternées de régions plus hydrophiles. Selon le modèle généralement accepté, les régions riches en GA se replient en feuillets  $\beta$  qui s'empilent en cristallites, le reste de la séquence constituant une matrice amorphe. La structure de la Fibroïne dans cette fibre semi-cristalline est appelée Silk II.

Le processus de formation de la soie est encore mal connu. Ses principaux facteurs seraient une baisse de pH, le changement de concentration de certains ions métalliques et des forces de cisaillement. Au cours de ce processus, la Fibroïne passerait par un intermédiaire conformationnel, appelé Silk I, dont la structure est largement débattue actuellement. Certains modèles proposent une structure en coude  $\beta$ , d'autres en feuillets  $\beta$  très lâches, d'autres encore en hélice. A une plus large échelle, l'arrangement des molécules de Fibroïne en micelles a été proposé sur la base du profil d'hydrophobicité de cette protéine. Ces micelles seraient ensuite étirées sous l'effet des forces de cisaillement pour former une fibre. La séquence temporelle entre la formation des micelles et la transition conformationnelle Silk I  $\rightarrow$  Silk II reste à explorer.



---

L'axe principal de ce travail de thèse concerne la compréhension du processus de formation de la fibre de soie. Dans ce cadre, une cellule microfluidique a été développée pour mimer le canal de filage de *Bombyx mori*. Il s'agit d'une cellule « tube-dans-tube », c'est-à-dire constituée de deux tubes insérés l'un dans l'autre. Cette cellule se rapproche de la forme du canal de filage de *B. mori* par sa géométrie concentrique. Elle permet de mimer la baisse de pH observée dans les conditions naturelles de production de la soie en injectant dans le tube externe un tampon acide et dans le tube interne la solution de Fibroïne. Les deux flux se mélangent par diffusion. L'ajustement des débits de chaque solution permet la compression du flux de protéine, comme observée dans le canal du ver à soie.

Les premières étapes de l'agrégation de la Fibroïne dans cette cellule microfluidique ont été suivies par SAXS. Elles montrent la formation d'agrégats dans lesquels la Fibroïne est sous une forme compactée par rapport à sa forme en solution. La taille de ces agrégats est de l'ordre de 100 nm. Dans un deuxième temps, ces agrégats semblent se compacter. Ces observations sont en accord avec le modèle de formation de micelles.

La fibre ainsi formée a été conservée dans le bain de collecte pendant différentes durées avant d'être séchée à l'air et caractérisée par WAXS et spectroscopie Raman. Cette incubation dans l'eau permet une évolution conformationnelle de la protéine. Ces deux techniques montrent que la soie séchée immédiatement après sa fabrication a une structure majoritairement amorphe de conformation Silk I. Cependant avec l'augmentation du temps d'incubation dans l'eau, la Fibroïne évolue vers une conformation Silk II et une structure semi-cristalline se développe. D'après l'analyse menée ici, cette évolution se fait sans autre intermédiaire conformationnel et résulte du réarrangement de régions désorganisées et d'hélices  $3_1$  en feuillets  $\beta$ . Cette transition s'accompagne d'un changement d'environnement des tyrosines depuis un milieu très hydrophobe vers un milieu plus hydrophile où elles se trouvent impliquées dans de fortes liaisons hydrogène via le groupement hydroxyle de leur chaîne latérale.

Ce processus en trois temps - agrégation des Fibroïnes - compaction des agrégats - transition conformationnelle et structurale - est proposé comme un modèle possible de formation de la soie *in vivo*.

---

Le second axe de ce travail est orienté vers l'amélioration des connaissances des propriétés physiques de la soie, en particulier sa résistance aux hautes températures et pressions.

L'effet de la température est étudié selon deux stratégies expérimentales. La première consiste à observer par WAXS les changements structuraux de la fibre *in situ* pendant l'augmentation de température. Cette stratégie montre que les cristallites subissent une expansion selon la direction d'empilement des feuillets  $\beta$  et la direction des liaisons hydrogène liant les brins  $\beta$  en feuillets. La seconde stratégie, permettant d'atteindre de plus hautes températures, consiste à analyser, à température ambiante, des fibres qui ont été préalablement chauffées dans un four. Elle met en évidence les effets irréversibles de la température. Les méthodes d'analyses utilisées sont 1) le WAXS, qui renseigne sur les changements structuraux des cristallites et de la matrice amorphe, 2) le SDS-PAGE, qui renseigne sur l'intégrité de la chaîne peptidique des protéines, et 3) les tests mécaniques, qui renseignent sur les propriétés de tension de la fibre. Les résultats de ces analyses montrent que les cristallites restent stables jusqu'à la température de carbonisation. Cependant, en dessous de cette température, la matrice amorphe subit une transition vitreuse précédée d'une augmentation du nombre de liaisons entre les chaînes peptidiques rendant la fibre plus rigide. La chaîne peptidique de la Fibroïne se dégrade dans le même intervalle de températures que les propriétés mécaniques.

L'effet des hautes pressions sur la structure de la soie est étudié par WAXS en utilisant une cellule Anvil diamant. Les résultats de ces analyses montrent que la structure des cristallites est capable de se compacter légèrement, principalement dans la direction des liaisons hydrogène liant les brins  $\beta$  en feuillets, avant de se désorganiser.

Les principales perspectives de ce travail sont une amélioration de la cellule microfluidique afin de se rapprocher des conditions *in vivo* et un élargissement de l'utilisation de cette technique à l'étude d'autres protéines.

---

# CONTENTS

<b>Abstract</b>	<b>3</b>
<b>Résumé</b>	<b>7</b>
<b>Résumé substantiel</b>	<b>8</b>
<b>CONTENTS</b>	<b>11</b>
<b>ABBREVIATIONS</b>	<b>15</b>
<b>INTRODUCTION</b>	<b>17</b>
In.1. Overview	17
In.2. Structure of thesis report	18
In.3. Thématique générale	18
In.4. Structure de ce manuscrit	19
<b>CHAPTER I- GENERAL BACKGROUND</b>	<b>21</b>
I.1. Silk: a biopolymer optimized for specific functions	23
I.2. Fibrous protein component	26
I.3. Silk fibre formation	29
I.4. Silk fibre properties and structure	35
I.5. Attempts to mimic natural silk spinning	40
<b>CHAPTER II- TECHNIQUES</b>	<b>47</b>
II.1. Protein preparation	49
II.2. Microfluidics	51
II.3. X-ray scattering	57
II.4. Raman spectroscopy	64



---

**CHAPTER III- ARTIFICIAL SPINNING OF SILK:**

<b>Fibroin Aggregation</b>	<b>69</b>
III.1. Experiments	71
III.1.1 Fibroin characterization by SAXS	71
III.1.2 Fibroin Aggregation observed by SAXS	72
III.2. Results and discussion	74
III.2.1 Fibroin characterization by SAXS	74
III.2.2 Fibroin Aggregation observed by SAXS	79

**CHAPTER IV- ARTIFICIAL SPINNING OF SILK:**

<b>Fibroin Conversion</b>	<b>85</b>
IV.1. Experiments	87
IV.1.1. Fibres production	87
IV.1.2. Raman Spectroscopy experiments	87
IV.1.3. WAXS experiments	87
IV.2. Results and discussion	89

**CHAPTER V- ARTIFICIAL SPINNING OF SILK:**

<b>Model of silk formation</b>	<b>99</b>
V.I. Proposed model	101
V.II. Comparison with other models	101
V.III. Perspectives to refine this model	102

---

**CHAPTER VI- PHYSICAL PROPERTIES OF SILK:**

<b>The Effects of temperature</b>	<b>105</b>
VI.1. Introduction	107
VI.1. Experiments	108
VI.2.1 Samples	108
VI.2.2 Heating conditions	109
VI.2.3 Gel electrophoresis	109
VI.2.4 Mechanical tests	110
VI.2.5 Synchrotron Radiation Scattering	110
VI.2. Results and discussion	113
VI.3.1 <i>In situ</i> heating experiment	113
VI.3.2 Pre-heated Fibres Analysis	115
VI.4 Conclusions	120

**CHAPTER VII- PHYSICAL PROPERTIES OF SILK:**

<b>Effect of pressure</b>	<b>123</b>
III.1. Experiments	125
VII.1.1 Sample and sample environment	125
VII.1.2 Diffraction experiment	127
III.2. Results and discussion	128

**CONCLUSION AND PERSPECTIVES** 133

<b>APPENDIX I.</b> Common protein secondary structures	<b>139</b>
<b>APPENDIX II.</b> ID13 and ID02 beamline layouts	<b>141</b>
<b>APPENDIX III.</b> Calculation of flow diffusion	<b>145</b>

---

<b>APPENDIX IV.</b>	<b>A microfluidic cell for studying the formation of regenerated silk by synchrotron radiation small- and wide-angle X-ray scattering</b>	<b>147</b>
<b>APPENDIX V.</b>	<b>SDS-PAGE solutions</b>	<b>159</b>
<b>APPENDIX VI.</b>	<b>Thermal Behavior of Bombyx mori Silk: Evolution of Crystalline Parameters, Molecular Structure, and Mechanical Properties</b>	<b>161</b>
<b>Acknowledgments</b>		<b>183</b>

---

## ABBREVIATIONS

A	Alanine
Be	Beryllium
DAC	diamond anvil cell
DLS	dynamic light scattering
ESRF	European synchrotron radiation facility
FibH	Fibroin heavy chain
FibL	Fibroin light chain
Fig.	figure
G	Glycine
GA	Glycine-Alanine
GPa	gigaPascal
LOF	Laboratory of future (Rhodia-CNRS-Bordeaux University, Pessac)
MW	molecular weight
Pa	Pascal
PEEK	Polyetheretherketone
PEO	polyethyleneoxide
PET	polyethylene terephthalate
$R_g$	radius of gyration
SAXS:	small-angle X-ray scattering
SDS-PAGE	sodium dodecyl sulfate-Polyacrylamide gel electrophoresis
SEM	scanning electron microscopy
SR	synchrotron radiation
WAXS	wide-angle X-ray scattering





# INTRODUCTION

## In.1. Overview

This thesis work aims at improving our understanding of silk formation. Silk is a biopolymer made by some arthropods, mainly arachnids and insects like lepidopteras, for different uses: protection of eggs and prey capture for instance [1-3]. The *Bombyx mori* silk has been used by human beings for more than 4000 years to make fabrics.

During the last century, spider dragline silk has been extensively studied because of its exceptional mechanical properties combining toughness and elasticity [4]. Moreover this fibre is spun by the spider under ecological conditions: at room temperature and pressure and with water as solvent. Being made of proteins, it is totally biodegradable and biocompatible. Thanks to these properties, spider silk could have applications in diverse areas such as textile or medicine for instance [5-7]. Therefore, it is of great interest to discover the mechanisms of silk formation to mimic or improve this fibre.

The fibre microstructure of silk spun by spiders and Lepidoptera is quite similar [8]. *Bombyx mori* silk can therefore be used as a model for silk polymers, although its mechanical properties are less attractive than those of spider silk [4]. The interest in using *B. mori* silk as a model is that its protein can be obtained in far larger quantities than the protein of spider silk.

Microfluidics has been used in this thesis work as a tool to mimic the *in vivo* silk spinning conditions. While the research into the characterization of flowing in channels of micrometric size is still in progress, such devices are already starting to be used to mimic the complexity of biological systems [9]. The combination of microfluidics and X-ray scattering studies provides the possibility of probing biological systems at the microscopic scale [10].

The comprehension of silk formation process is not only interesting in the field of high performance polymer science, it can also serve as a model for understanding the folding of fibrous protein into an insoluble structure. Such phenomena are of crucial interest in medical research into the Prion protein (PrP) and the amyloid  $\beta$ -peptide involved respectively in the Creutzfeldt-Jakob and Alzheimer's diseases [11, 12].

## In.2. Structure of this thesis report

This report presents, in Chapter I, an overview of the general literature about the silk biopolymer, mainly its role, synthesis and properties in nature. In Chapter II the principles of the techniques used in this thesis work are introduced. The three following chapters are dedicated to the description of experiments done to elucidate the silk formation process, and the discussion of their results. The two last chapters present experiments which reinforce our knowledge about the physical properties of natural silk, namely its resistance to high pressures and temperatures.

## In.3. Thématique générale

Ce travail de thèse a pour but d'améliorer notre compréhension du processus de formation de la soie. La soie est un bio-polymère fabriqué par quelques arthropodes, principalement des araignées et des insectes, pour assurer des fonctions variées : la protection des œufs ou la capture de proies par exemple [1-3]. La soie de *Bombyx mori* est utilisée par les humains depuis plus de 4000 ans pour fabriquer du tissu.

Durant le siècle dernier, la soie du filin de sureté de l'araignée a été largement étudiée en raison de ses exceptionnelles propriétés mécaniques qui combinent élasticité et solidité. De plus, cette fibre est synthétisée par l'araignée dans des conditions écologiques : à température et pression ambiante et en utilisant l'eau comme solvant. Etant constituée de protéines, elle est entièrement biodégradable et biocompatible. Grâce à ces propriétés, cette soie pourrait trouver de nombreuses applications dans le textile ou la médecine par exemple [5-7]. Il serait donc très intéressant de découvrir les mécanismes de sa formation afin de mimer, ou même d'améliorer cette fibre.

La microstructure de la soie filée par le vers à soie *B. mori* est très similaire à celle de la soie produite par les araignées [8]. Elle peut donc être utilisée comme modèle d'étude de la soie en général, bien que ses propriétés mécaniques ne soient pas aussi attractives que celles de la soie d'araignée [4]. L'intérêt de ce modèle réside dans la facilité d'obtention des protéines composant la soie de *B. mori* comparée à celles composant la soie d'araignée.

La microfluidique a été utilisée dans ce travail de thèse comme un outil permettant de mimer les conditions de filage de la soie *in vivo*. La caractérisation des écoulements dans des canaux de taille micrométrique étant encore en plein développement scientifique, de tels appareils sont déjà largement utilisés dans le but de mimer la complexité des systèmes biologiques [9]. La combinaison de la microfluidique et des techniques de diffusion des rayons X apporte de nouvelles possibilités d'études des systèmes biologiques à l'échelle microscopique [10].

La compréhension du processus de formation de la soie ne concerne pas seulement la science des polymères. Elle peut être considérée plus généralement comme un modèle d'étude du repliement de protéines fibreuses en une structure insoluble. De tels processus sont d'un intérêt crucial dans le domaine de la recherche médicale sur des protéines amyloïdes telles que le Prion ou les peptides  $\beta$ -amyloïdes impliqués respectivement dans les maladies de Creutzfeldt-Jakob et d'Alzheimer [11, 12].

## In.4. Structure de ce manuscrit

Ce manuscrit présente en chapitre I un résumé des données de la littérature concernant la soie en tant que bio-polymère, principalement son rôle, sa synthèse et ses propriétés naturelles. Le chapitre II expose brièvement le principe des techniques employées au cours de ce travail de thèse. Les trois chapitres suivants sont consacrés à la description d'expériences dédiées à la compréhension du processus de formation de la soie et à la discussion de leurs résultats. Les deux derniers chapitres présentent des expériences renforçant nos connaissances des propriétés physiques de la soie, en particulier sa résistance aux hautes températures et pressions.



---

## Bibliography

1. Vollrath, F., *Spider Webs and Silks*. Scientific American, 1992. **266**(3): p. 70-76.
2. Kaplan, D., et al., *Silk - Biology, Structure, Properties, and Genetics*. Silk Polymers, 1994. **544**: p. 2-16.
3. Craig, C.L., *Evolution of Arthropod Silks*. Annual Review of Entomology, 1997. **42**: p. 231-267.
4. Gosline, J.M., M.E. Demont, and M.W. Denny, *The Structure and Properties of Spider Silk*. Endeavour, 1986. **10**(1): p. 37-43.
5. Scheibel, T. and D. Huemmerich, *Proteins of natural origin and materials made therefrom*. United States Patent 20070196429, 2007.
6. Islam, S., et al., *Methods and apparatus for spinning spider silk protein*. United States Patent 7057023, 2006.
7. Vollrath, F. and D.P. Knight, *Liquid crystalline spinning of spider silk*. Nature, 2001. **410**(6828): p. 541-548.
8. Fraser, R.D.B. and T.P. MacRae, *Conformation in fibrous proteins*. New York: Academic Press, 1973.
9. Arnaud, C.H., *Mimicking biological systems*. Chemical & Engineering News, 2007. **85**(37): p. 14-19.
10. Pfohl, T., et al., *Trends in microfluidics with complex fluids*. Chemphyschem, 2003. **4**(12): p. 1291-1298.
11. Brown, D.R., *Introduction: Copper and amyloid fibril formation*. FEBS journal, 2007. **274**(15): p. 3755-3755.
12. Vestergaard, B., et al., *A helical structural nucleus is the primary elongating unit of insulin amyloid fibrils*. Plos Biology, 2007. **5**(5): p. 1089-1097.

## **Chapter I- GENERAL BACKGROUND**



**Résumé de ce chapitre :**

Dans ce chapitre, la soie est présentée en tant que bio-polymère optimisé pour des fonctions naturelles spécifiques. Le ver à soie *Bombyx mori* produit cette soie pour construire le cocon qui protège la larve pendant sa métamorphose. La soie de *B. mori* est constituée de deux brins enveloppés d'une glue. Les deux brins sont constitués d'une protéine et assurent la solidité du cocon. La glue est constituée d'une autre protéine (Séricine) et assure principalement la cohésion des brins et ainsi l'intégrité du cocon. Les araignées tissent jusqu'à sept soies différentes ayant un rôle spécifique, et donc une constitution et des propriétés adaptées.

Les propriétés mécaniques de la soie, leur nature protéique et leur synthèse *in vivo* en conditions peu coûteuses économiquement et écologiquement en font des polymères ayant de possibles applications dans divers domaines tels que le textile et la médecine, par exemple.

La protéine constituant les brins de soie de *B. mori* est la Fibroïne. Sa structure primaire est modulaire. Elle est constituée de 11 régions hautement répétitives riches en Alanine et Glycine, alternées de régions « espaceurs » plus hydrophiles.

La synthèse *in vivo* de la soie se passe dans l'appareil de filage du vers à soie. Les protéines sont synthétisées puis transportées tout au long d'une glande allongée. Au cours de ce transport la solution de Fibroïne est convertie en une fibre solide et insoluble à l'eau. Cette conversion implique de nombreux facteurs chimiques et mécaniques, tel que la variation de pH et de concentration de certains ions métalliques, une déshydratation et des forces de cisaillement accompagnant l'écoulement.

La fibre de soie est à la fois très étirable et résistante. Ces propriétés mécaniques sont probablement dues à sa structure semi-cristalline, mais également à sa morphologie à plus grande échelle. Des modèles mathématiques sont construits afin de décrire ces propriétés et de prévoir l'effet de divers paramètres tels que la cristallinité.

Parallèlement, plusieurs méthodes sont utilisées pour synthétiser *in vitro* des fibres de Fibroïne ayant des propriétés mécaniques comparables à celles de la soie naturelle.

The aim of this chapter is to show what is already known about natural silk and what remains to be clarified. In particular, the process of silk formation and the relationship between its structure and mechanical properties are not yet fully understood. Although this chapter is mainly focused on silkworm silk, some comparisons with spider silk are developed.

## I.1. Silk: a biopolymer optimized for specific functions

The silkworm is the larvae of the moth *Bombyx mori*. This Lepidoptera originates from a small egg and undergoes five larvae stages. At the end of its fifth larvae stage, the worm weaves a silk cocoon to protect the pupa during its metamorphosis to the imago.

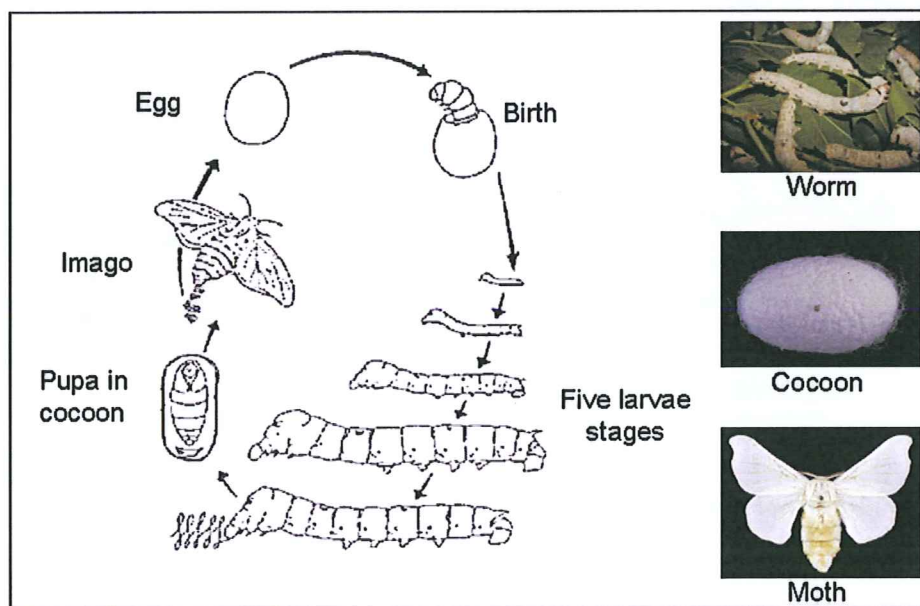
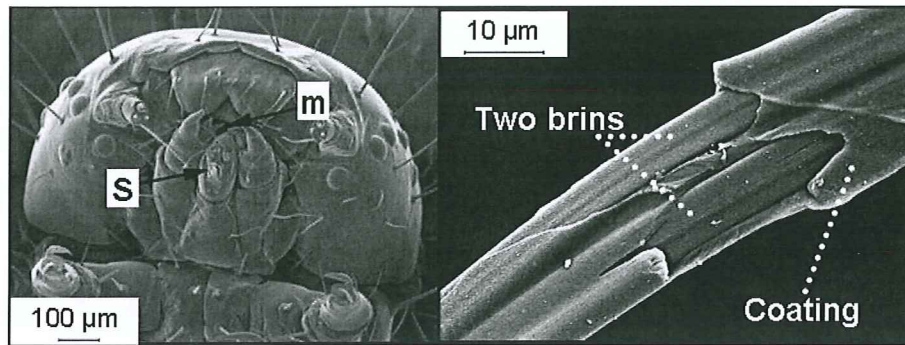


Fig. 1: *Bombyx mori* life cycle [1].

To build the cocoon around itself, the worm pulls the silk thread from its spinneret, which is situated close to its mouth, by moving its head in an “8” shape. The silk thread (also called: bave) is made of two parts: two brins and a coating (Figure 2). The brins ensure the cocoon’s toughness. The coating ensures the cohesion of the cocoon by gluing the brins and the different layers together.



*Fig. 2: SEM pictures of Lepidoptera head (left, s: spigot; m: mouth) [15] and silk thread (right).*

The coating is made of several serine-rich proteins named Sericins, which are synthesized by alternative splicing from three different genes [19]. The brins are made of Fibroin, a glycine/alanine-rich fibrous protein. As shown in figure 3, the two components have specific roles to protect the pupa. However, the present thesis project is focused on the fibrous component, the Fibroin brins.

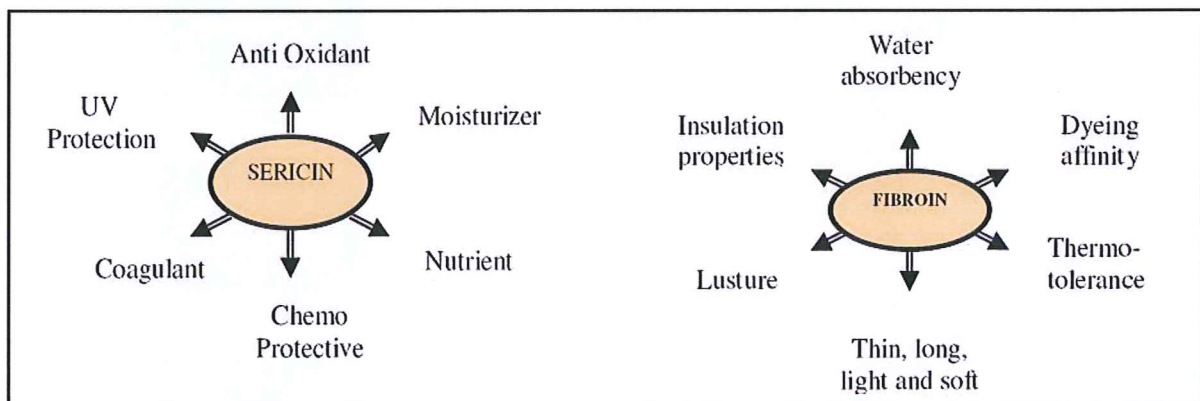


*Fig. 3: The two protein components of silk and their attributes [2].*

The main function of silkworm silk is to make a protecting cocoon. Spiders have a much larger variability of silk production which have different functions. The production of cocoon silk is only one of them [4] (figure 4). Each silk is made of different protein components.



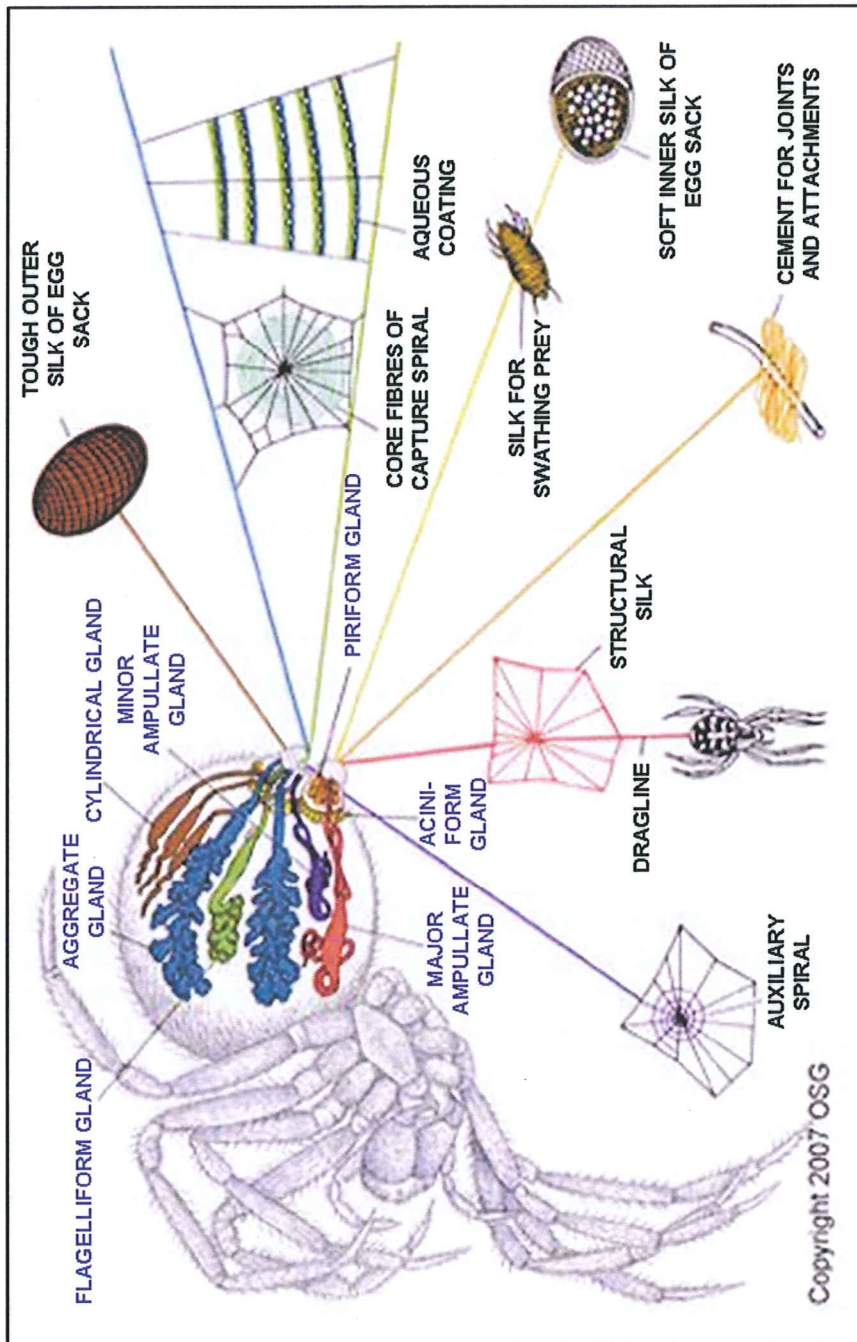


Fig. 4: Example of the variety of silk made by spiders [4].

## I.2. Fibrous protein component

Proteins are biological polymers made of twenty different molecular units called amino acids. A protein is defined on different organization scales by its amino acid sequence (or primary structure), the local folding of the amino acid chain (secondary structure), its whole three dimensional shape (tertiary structure) and its arrangement with other proteins (quaternary structure). The most common secondary structures of protein are shown in appendix I [23, 24]. The protein sequence is encoded in the genome.

Protein synthesis occurs in all living cells. Proteins ensure a wide range of functionalities inside and outside the cell, like cell mobility, intra-cellular transport, cell recognition and chemical reaction catalysis. Silk Fibroin is an example of protein ensuring an extracellular structural role.

The Fibroin protein of *B. mori* silk is made of two chains: a heavy chain (FibH) and a light chain (FibL). The two chains are linked by a disulfide bond between the cysteines 5244 of FibH and 190 of FibL. FibL has a molecular weight (MW) of 25781.5 Da and has a non-repetitive sequence (figure 5).

```
SVTINQYSDNEIPRDIDDGKASSVISRAWDYVDDTDKSIALNVQEILKDMASQ
GDYASQASAVAQTAGIIAHL SAGIPGDACAAANVINSYTDGVRSGNFAGFRQ
SLGPF FGHV GQNLNLINQLVINPGLRYSVGPALGCAGGGRIYDFEAAWDAI
LASSDSSFLNEEY CIVKRLYNSRNSQSNNIAAYITAHLLPPVAQVFHQ SAGSIT
DLLRGVGN GNDATGLVANAQRYIAQAASQVHV
```

Fig. 5: FibL sequence [6].

FibH is a large protein (MW=389203.4 Da). It has a modular primary structure made of an Amino-terminal and a Carboxy-terminal non-repetitive region (blue), and between them, 11 glycine/alanine-rich repetitive regions (red) alternating with 11 spacer regions (green) (figure 6). The spacer regions have a sequence richer in hydrophilic and large amino acids. This modular sequence is essential for the structure of the silk thread.





These alanine-rich domains can be considered as equivalent to the GA-rich domains of *B. mori* FibH, during folding and in the final structure. The silk spinning apparatus of spiders and insects are homologous, which means that they derive from the same organ of their common ancestor [28].



### I.3. Silk Fibre Formation

The spinning process converts a Fibroin solution into an insoluble fibre. The main physico-chemical factors which are thought to be involved in this process are the Fibroin concentration, pH [29], the ionic composition of the dope through the silk gland, as well as shearing forces along the spinning duct [30]. Reviews of the different factors involved are available for *B. mori* [31] and spiders [30].

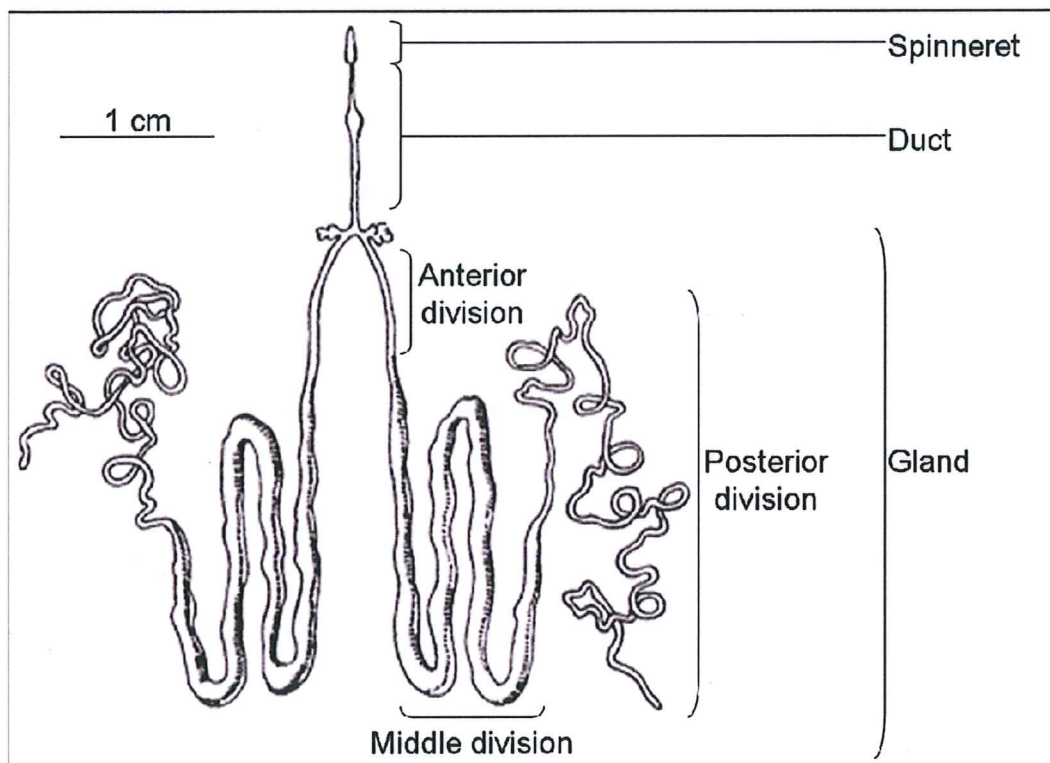
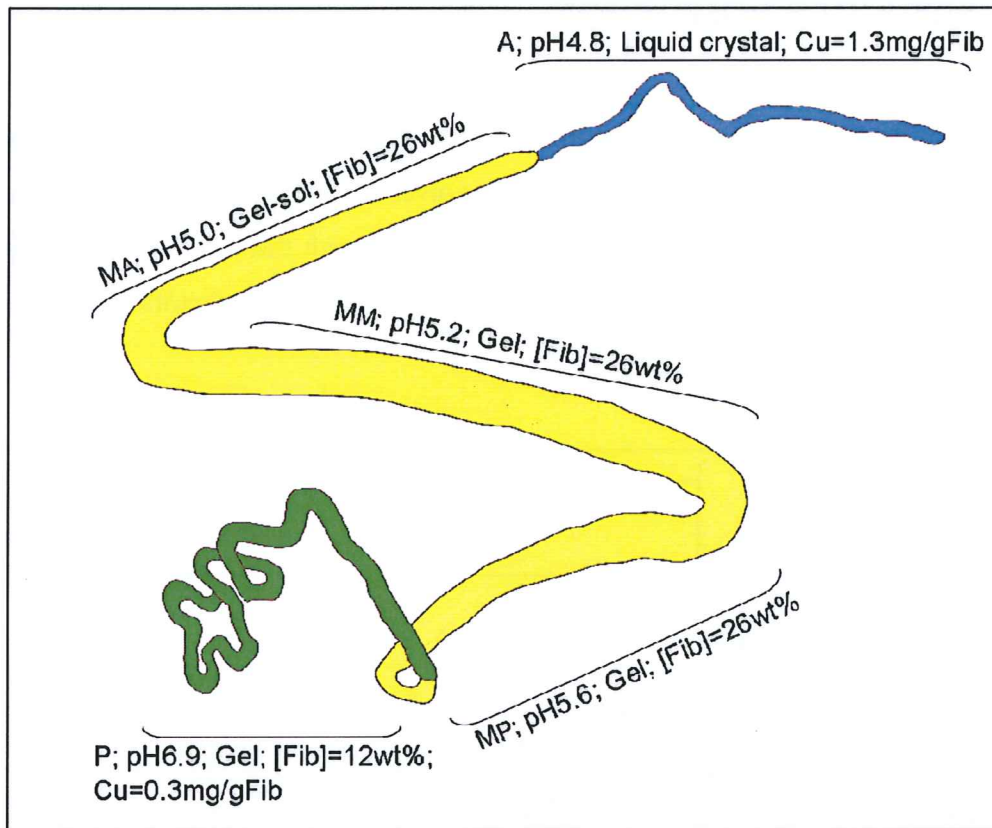


Fig. 7: *Bombyx mori* spinning apparatus [5].

The *Bombyx mori* spinning apparatus (figure 7) is made of two parallel silk glands derived from salivary glands [32], joining in one spinning duct ended by a spinneret. Three divisions can be identified in the gland: the posterior division (P), where the Fibroin is secreted, the middle division (M), where the Fibroin is stored and Sericin sequentially added, and the anterior division (A). The Fibroin secretion unit consists of six heterodimers FibH-FibL linked together by the P25 glycoprotein through non-covalent interactions [33]. This structure is thought to ensure the solubility of the highly concentrated protein solution until its spinning.



*Fig. 8: Physical and chemical conditions of silk dope along the silk gland of Bombyx mori larvae [20-22].*

The middle division can itself be divided in three parts: the posterior (MP), middle (MM) and anterior (MA) parts. Along the silk gland, the conditions change: the pH decreases while the concentration of the Fibroin increases. A concomitant change in the dope state from gel to solution has to be noted.

The concentrations of some metallic ions also change relatively to the Fibroin concentration. The concentrations of sodium, potassium, magnesium, copper and zinc increase while the calcium concentration decreases [17].

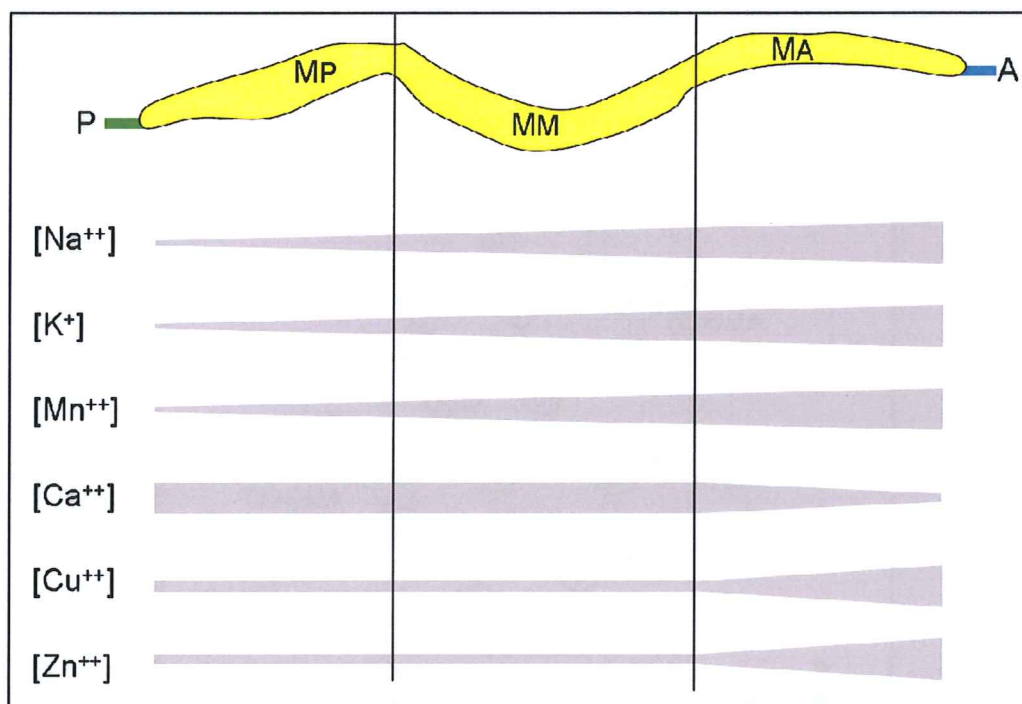


Fig. 9: Relative evolution of the concentration of six metallic ions along the middle division of the Bombyx mori silk gland, relatively to the Fibroin concentration [17].

Copper is known to induce fibrillar protein conformational transitions from random coil to  $\beta$ -sheet folding (Prion protein,  $\beta$ -amyloid...) [34]. Its concentration increases in the last part of the middle division of the silk gland [17]. Zhou *et al.* [21] suggest that calcium could play a role in the destruction of the random-coil-protein network leading to an intermediate structure, allowing the copper to induce the conformational transition to a  $\beta$ -sheet structure. However, Kobayashi *et al.* [24], suggest that the calcium would maintain the protein network present in the gel state. Both hypotheses are coherent with the calcium concentration profile presented in figure 9. However, this profile of concentration is not unanimously accepted [22]. Ruan *et al.*, showed that the potassium also induces the transition from a random-coil (or  $\alpha$ -helix) structure to a  $\beta$ -sheet structure [35]. The precise role of each ion is still unclear.

Several models try to describe the Fibroin spinning process on a molecular scale. Here, two of them are shown as examples. Both are based on the study of model peptides representatives for the GA-rich repeats. After experiment of nuclear magnetic resonance (NMR) and molecular dynamics simulations, Asakura suggests that the Fibroin could be first in a random coil and/or helical conformation. Then, it would undergo conformational changes



including a mainly  $\beta$ -turn intermediate conformation (figure 10) named silk I structure. Finally Fibroin would reach a mainly  $\beta$ -sheet conformation [18].

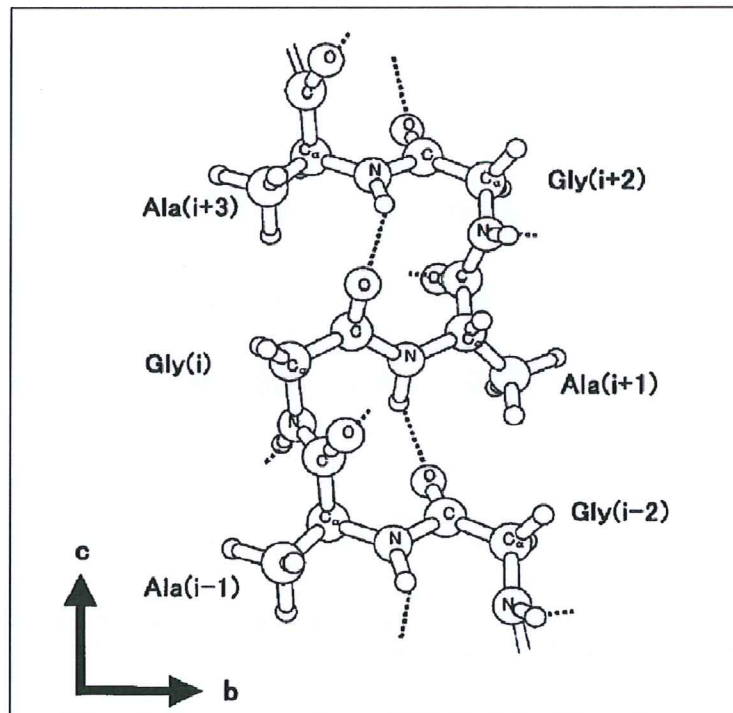


Fig. 10: The conformation of a repeated  $\beta$ -turn type II-like molecule as a model for silk I proposed by Asakura *et al.* [18]; there are intra-molecular hydrogen bonds between the carbonyl oxygen atom of the  $i^{\text{th}}$  G residue and the amide hydrogen atom of the  $(i + 3)^{\text{th}}$  A residue.

Using Fourier transform infrared spectroscopy (FTIR), circular dichroism, and electron diffraction, Wilson *et al.* [10] call silk I the initial random-coil or extended helix structure and suggest a three-fold helix named silk III as a possible intermediate before the  $\beta$ -sheet folding (figures 11 and 12) [13].

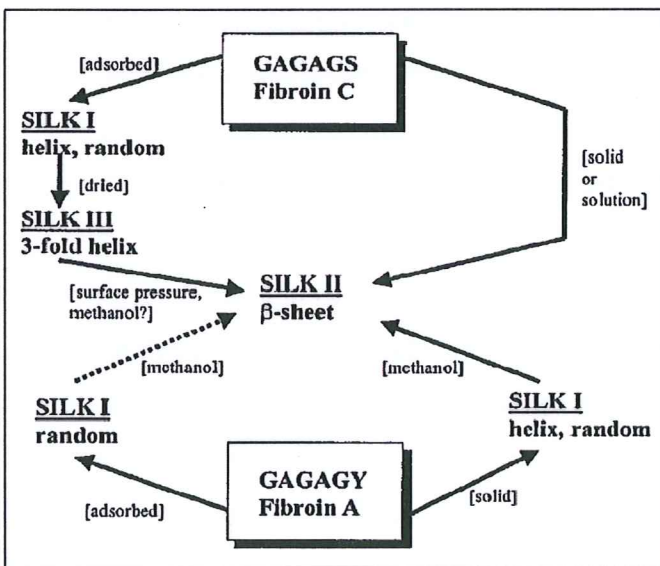


Fig. 11: FibH fragments folding pathway proposed by [10].

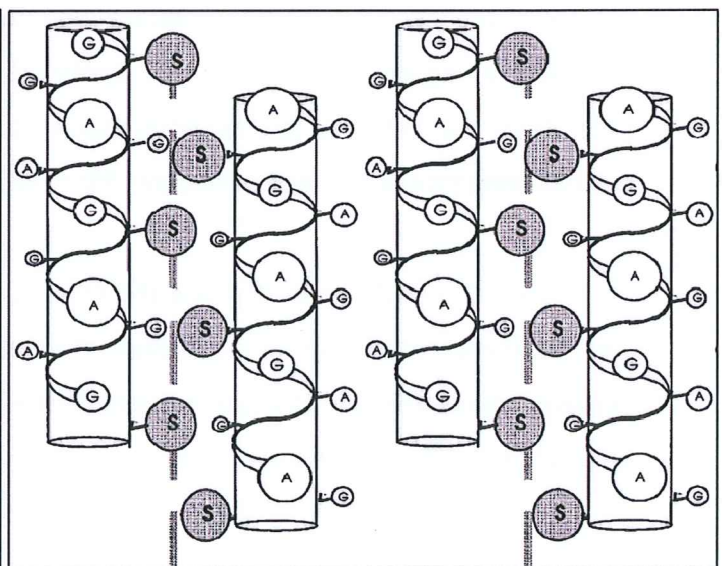


Fig. 12: Silk III: three-fold helix suggested as a folding intermediate by [13].

Fossey *et al.* [36] and He *et al.* [37] define silk I as a  $\beta$ -sheet structure different from the structure observed in silk fibre.

Finally, the  $\beta$ -sheets are assumed to stack in microcrystalline domains [38], giving the ultimate semi-crystalline structure of the fibre called silk II:  $\beta$ -sheet nanometer-sized crystalline domains embedded in an amorphous matrix formed by the non-repetitive part of the Fibroin [39, 40]. Some of the  $\beta$ -sheets may remain isolated and constitute a short-range order fraction [41]. This folding is linked to the modular primary structure of FibH: the GA-rich regions fold in  $\beta$ -sheets, the non-repetitive regions and spacers remaining amorphous (random coil,  $\beta$ -turn or  $\alpha$ -helix belong to the models). The role of the spacers sequence is rarely questioned given its regularity. Evidence for the formation of a nanofibrillar superstructure has also been obtained [41, 42].

Some models, based on circular dichroism measurements, propose that the  $\beta$ -sheet crystallites formation occurs through a nucleation dependent process [43]. Other models assume intermediate aggregation steps involving the formation of micelles driven by the hydrophobic profile of FibH [8] (Figure 13). This model is based on the observation of such structure by scanning electronic microscopy (SEM) on Fibroin dope. These micelles constitute a liquid-crystalline phase [22].

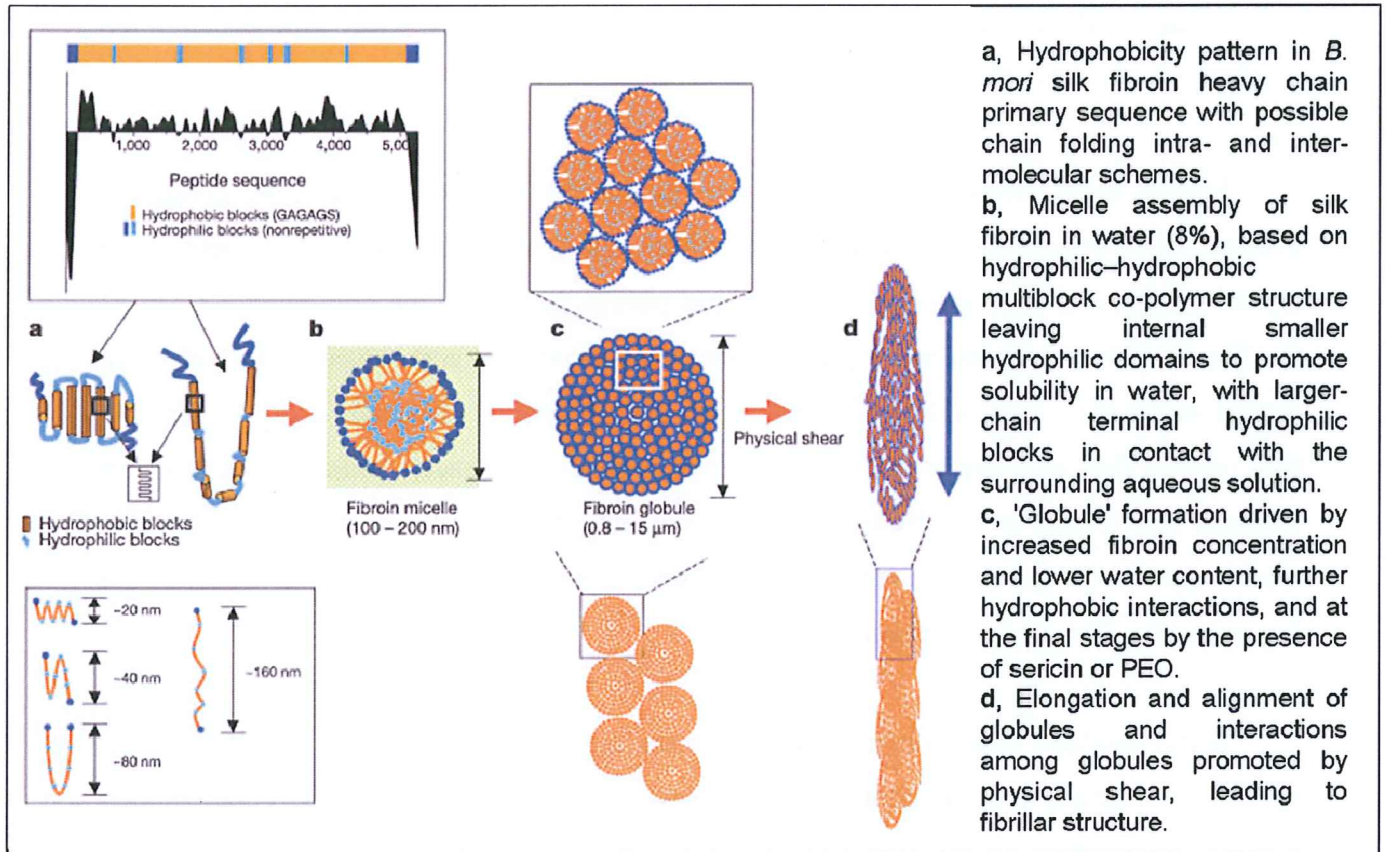


Fig. 13: Model of Fibroin folding via a micelle step [8].

In short, the conversion of the Fibroin solution to an insoluble fibre is thought to be an aggregation dependent process leading to a mainly  $\beta$ -sheet conformation. The conformation of the intermediate steps is still not definitively determined but a mainly  $\beta$ -turn intermediate could take place in this process. The causal relationship between  $\beta$ -sheet folding and aggregation remains unclear.

As already mentioned, similar schemes are discussed for spider silk formation.



## 1.4. Silk Fibre Properties and structure

Besides its aesthetic quality, silk -and particularly spider silk- has interesting tensile properties which combine high strength and high elasticity [27, 44]. The tensile properties of a fibre can be determined by a stress/strain curve [45]. The fibre is elongated until it breaks while recording the length increase ( $\Delta l$ ) and the force necessary to pull. The strain ( $\epsilon$ ) of the fibre is its elongation ( $\Delta l$ ) divided by its initial length ( $l_0$ ) (Equation 1). It can be expressed as a percentage of the initial length. The applied force ( $F$ ) is typically normalized by the area of the fibre cross section ( $A$ ), giving a nominal stress value ( $\sigma$ ) expressed in Pa (Equations 2). The stress reached when failure takes place is the “strength” of the material. The stress-strain curve shows the tensile properties of the fibre.

$$\epsilon = \frac{\Delta l}{l_0} \quad \text{Equation 1}$$

$$\sigma = \frac{F}{A} \quad \text{Equation 2}$$

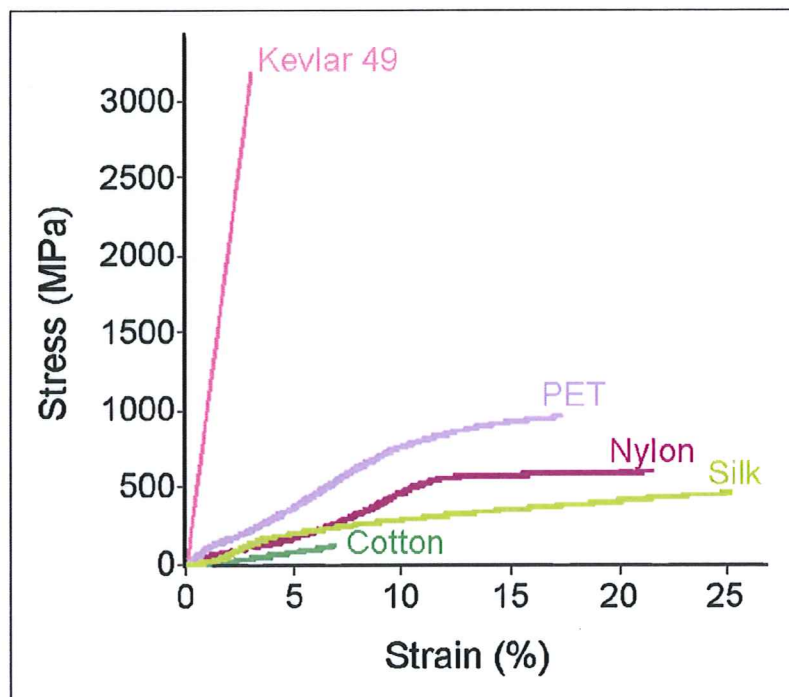


*Fig. 14: Tensile properties of selected man-made and natural fibres (Stress/strain curves obtained as part of this thesis work).*

The mechanical properties of silk are often explained by an elastomeric behavior [46]. The stress-strain curves of typical elastomeric fibers like nylon or PET (see Figure 14) show two parts. The first part represents the deformation under an elastic regime which is reversible. The slope of this phase is called the elastic modulus (in Pa). The second part represents the deformation under a plastic regime which is irreversible.

Natural degummed silkworm silk has an approximate maximum stress of 1.1 GPa and a maximum elongation of approximately 24%. The spider dragline silk has a maximum stress of about 1.75 GPa and a maximum elongation of approximately 15% [47]. As illustrated in table 1 [9], these values vary a lot according to different authors.

Initial Modulus (GPa)	Strength (MPa)	Elongation (%)	Remarks
	500	15	Natural spinning
	700	22.5	Obtained by forced silking
5		27	Tested in water
23		6.6	Tested in Ethanol
19		17	Tested in air
16	650	15	
8.9 - 17.4	320 - 600		
16	650		A single brin
12.4 – 17.9	360 - 530	18 - 21	Obtained by forced silking
12 - 17	450 - 700	12	Forcibly reeled and degummed silk
	400	22	
	570	23.5	Fine silk fibre
	240	22.4	Coarse silk fibre
9	320	16	Treated with methacrylamide
		10.56	Fine silk fibre
		17.25	Coarse silk fibre
5	600	15 - 35	

*Table 1: Variability of silk mechanical properties found in the literature (reviewed by Zhao et al. [9]).*

Figure 15 shows the stress-strain curve of natural non-degummed silkworm silk. The low stress at breaking point can be explained by the fact that the sericin layer is taking into account in the cross section area but has no significant effect on the tensile properties with regard to the variability between fibres [48].



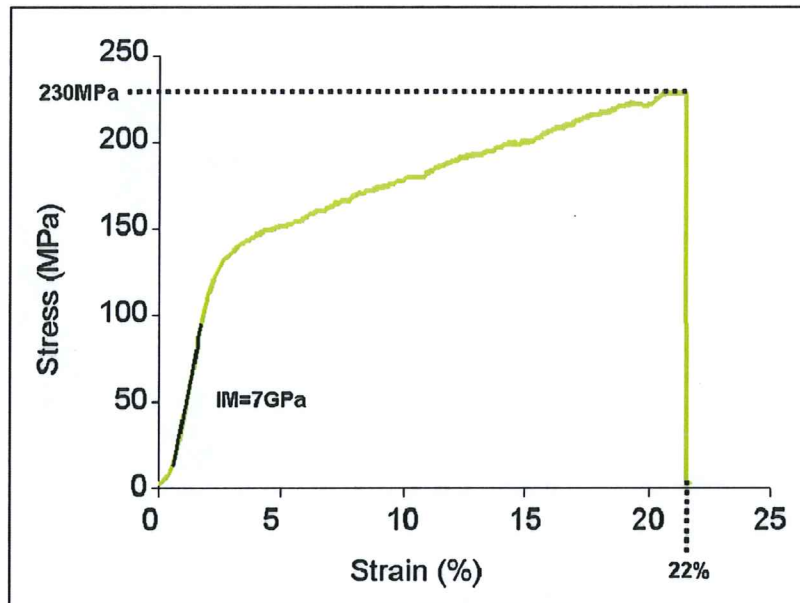
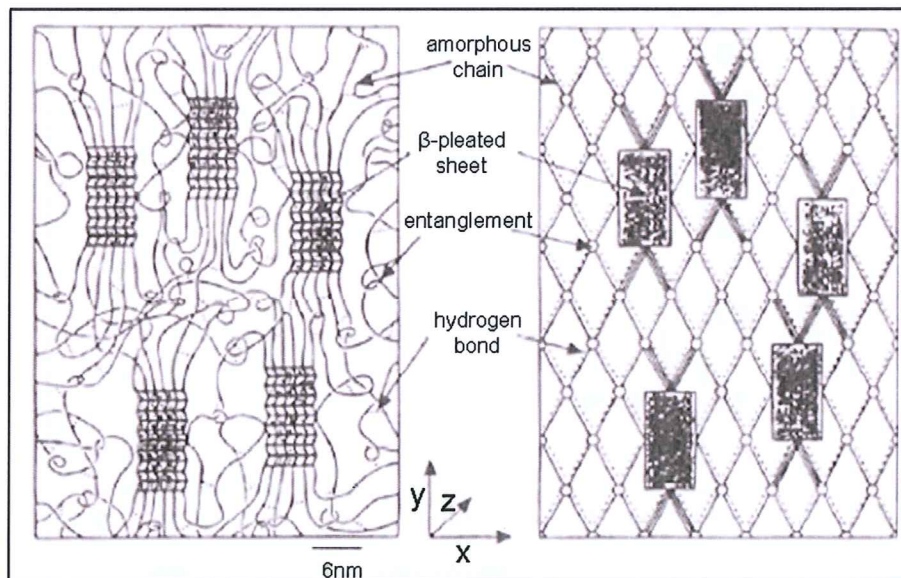


Fig. 15: Stress- strain curve of natural (non-degummed) *B. mori* silk.

These mechanical properties can be related qualitatively to the semi-crystalline fibre structure as follows: during the elastic regime, the polypeptide chains in the amorphous phase straighten (breaking of hydrogen bonds [7]) and the crystallites are elastically deformed [49]. An increase of the orientation of the crystallites along the fibre axis has also been observed in the case of spider silk [50]. The plastic regime deformation can be related to the irreversible breaking of molecular bonding.

Some microscopic models of silk have been developed to help understand the relationship between the structure and the mechanical properties. The best known is the Termonia model [7] (Figure 16): a set of oriented crystallites linked by an amorphous network of hydrogen bonds and entanglements allows the tensile properties of dry and wet spider silk to be simulated, and to predict their change with modification of crystallites size and aspect ratio.



**Fig. 16: Termonia's model to predict the mechanical properties of dragline spider silk [7].**

The hierarchical organization in microfibrils [41, 42] or in skin-core structure [51, 52] might also influence the tensile properties as for Nylon [53].

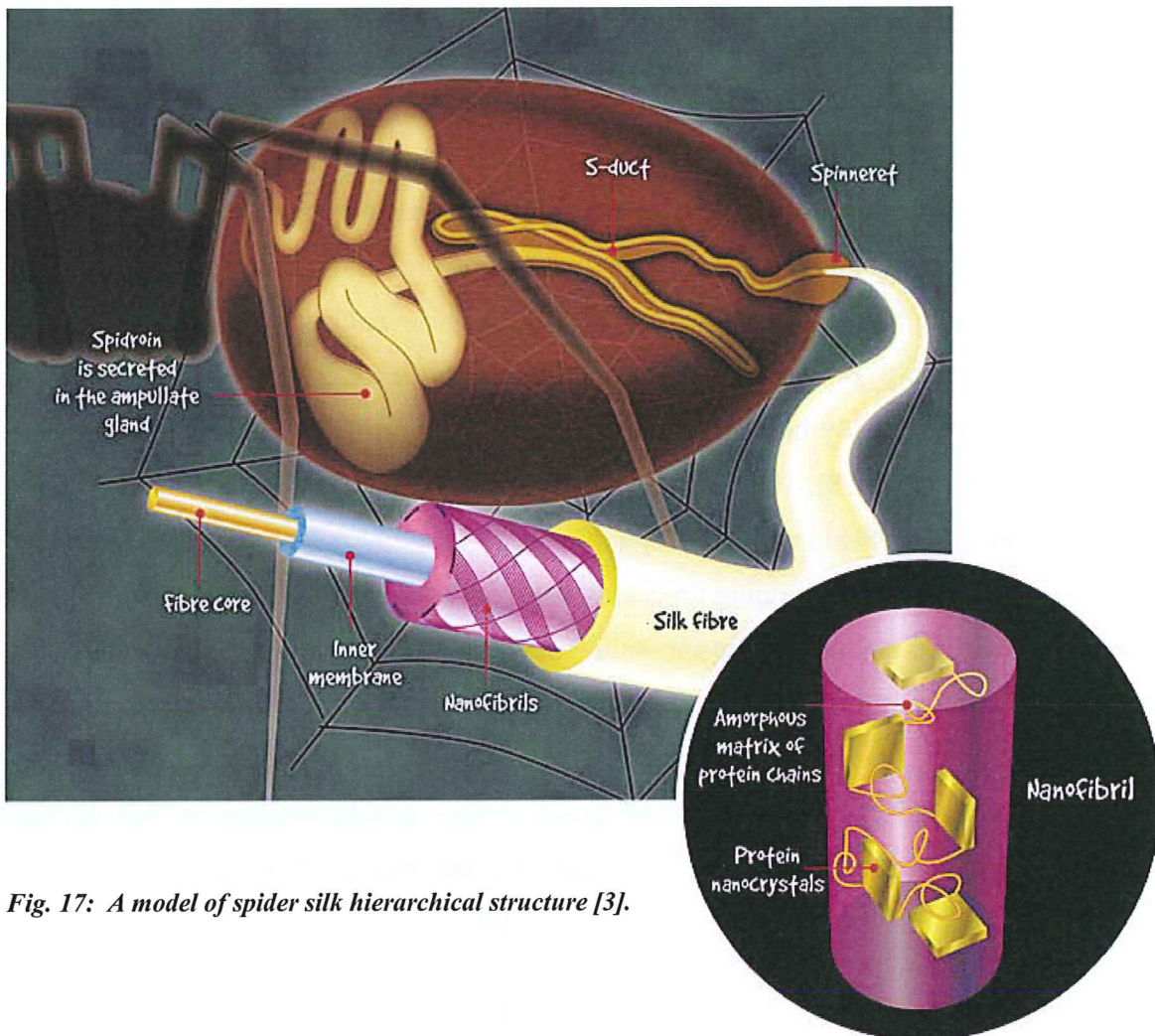


*Fig. 17: A model of spider silk hierarchical structure [3].*

The semi-crystallinity of silk is well identified through the observation of crystalline and amorphous fractions by X-ray and neutron diffraction techniques [41, 50, 54, 55]. However, the details of its hierarchical structure and its relationship with the mechanical properties of the fibre are still unclear. Some models which use a phenomenological approach involving zones which differ in their hydrogen bond density are built to attempt to answer this question [56].



## I.5. Attempts to mimic natural silk spinning

Scientists try to mimic silk spinning to produce fibers from silk protein dope. Their aim is to make fibers with mechanical properties close to those of natural spider silk, or even better. Ideally, this should be done using recombinant protein, which would provide an additional possibility to control the silk properties by gene engineering. Such “designed” fibers would have many applications for the textile industry or for medical uses, for example. Several patents have already been deposited concerning the artificial spinning of spider silk and its applications [57, 58]. Here, three spinning processes are presented: shear spinning [14], wet spinning [11, 59-61] and electrospinning [12, 62].

Figure 18 shows two spinning processes using only shearing forces. On the left (a), the surface of a highly concentrated Fibroin solution is only touched with a glass rod and, by gently pulling, a fiber is produced. On the right (b), the Fibroin solution is injected through a thin capillary [14]. The first method gives a fiber in which the proteins are in a silk I conformation although the second method gives a fiber structure closer to silk II. This experiment underlines the importance of the shearing in the spinning process.

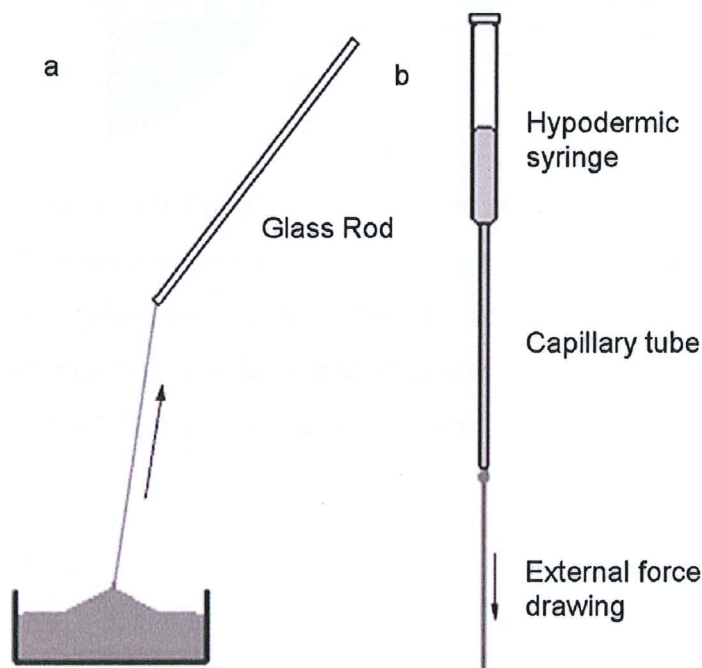


*Fig. 18: Fibroin shearing by spinning only [14].*

Figure 19 describes the electrospinning technique. Here, an electric field is applied between a reservoir which contains the Fibroin dope and a metallic collection plate. The

viscous dope forms a drop at the end of the needle. The voltage is increased until the charge overcomes the surface tension. A jet is formed; its size is tunable by adjusting the voltage. Very thin fibers with diameters in the 10 nm range have been spun using this method. These fibers have interesting mechanical properties approaching those of natural silk, although their structure seems to be that of silk I [63].

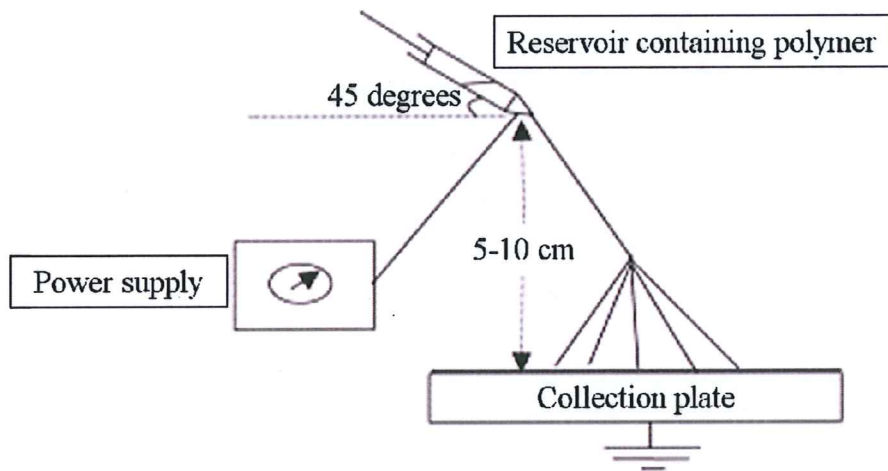


*Fig. 19: Electrospinning principle [12].*

The most frequently used spinning process to mimic natural silk formation is the wet spinning method. This method consists of injecting a Fibroin solution jet in one or more successive baths. The chemical composition of the bath, and any drawing steps that take place within the baths, influence the mechanical properties and structure of the fibres [11, 61, 64]. Figure 20 shows an example of a wet spinning set up. The microfluidic spinning process presented in this study is a wet spinning process where the coagulation bath volume is minimized. Recently, a microfluidic device mimicking both the chemical evolution of the dope and the shearing conditions has been used to spin recombinant spider silk protein [65].



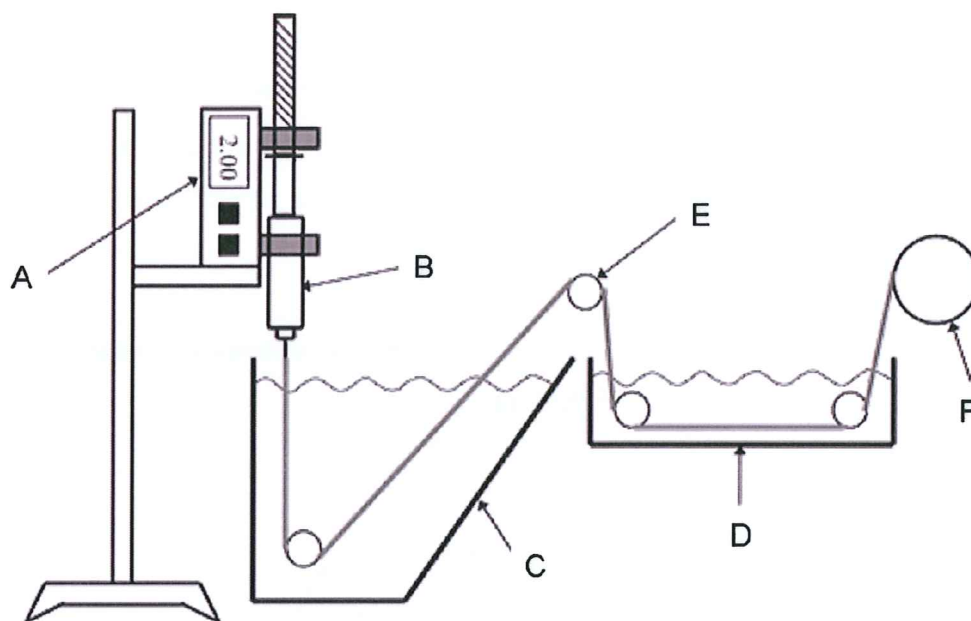


*Fig. 20: Example of wet spinning set up [11] (A: mechanical pump; B: polymer solution in the syringe; C: coagulation bath; D: wash bath; E: draw rolls; F: take up roll).*

## Bibliography

1. Veda, K., I. Nagai, and M. Horikomi, *Silkworm Rearing*. Science publishers, 1997.
2. Mondal, M., K. Trivedy, and S. Nirmal Kumar, *The silk proteins, sericin and Fibroin in silkworm, Bombyx mori Linn., - A review*. Caspian Journal of Environmental Sciences, 2007. **5**(2): p. 63-76.
3. Fox, D., *The spinners*. New Scientist, 1999. **162**(2183): p. 38-41.
4. Vollrath, F., *Spider Webs and Silks*. Scientific American, 1992. **266**(3): p. 70-76.
5. Willcox, P.J., et al., *Evidence of a cholesteric liquid crystalline phase in natural silk spinning processes*. Macromolecules, 1996. **29**(15): p. 5106-5110.
6. Yamaguchi, K., et al., *Primary Structure of the Silk Fibroin Light Chain Determined by Cdna Sequencing and Peptide Analysis*. Journal of Molecular Biology, 1989. **210**(1): p. 127-139.
7. Termonia, Y., *Molecular Modeling of Spider Silk Elasticity*. Macromolecules, 1994. **27**(25): p. 7378-7381.
8. Jin, H.J. and D.L. Kaplan, *Mechanism of silk processing in insects and spiders*. Nature, 2003. **424**(6952): p. 1057-1061.
9. Zhao, H.P., X.Q. Feng, and H.J. Shi, *Variability in mechanical properties of Bombyx mori silk*. Materials Science & Engineering C-Biomimetic and Supramolecular Systems, 2007. **27**(4): p. 675-683.
10. Wilson, D., R. Valluzzi, and D. Kaplan, *Conformational transitions in model silk peptides*. Biophysical Journal, 2000. **78**(5): p. 2690-2701.
11. Ha, S.W., A.E. Tonelli, and S.M. Hudson, *Structural studies of Bombyx mori silk Fibroin during regeneration from solutions and wet fiber spinning*. Biomacromolecules, 2005. **6**(3): p. 1722-1731.
12. Sukigara, S., et al., *Regeneration of Bombyx mori silk by electrospinning - part 1: processing parameters and geometric properties*. Polymer, 2003. **44**(19): p. 5721-5727.
13. Valluzzi, R. and S.P. Gido, *The crystal structure of Bombyx mori silk Fibroin at the air-water interface*. Biopolymers, 1997. **42**(6): p. 705-717.
14. Xie, F., et al., *Effect of shearing on formation of silk fibers from regenerated Bombyx mori silk Fibroin aqueous solution*. International Journal of Biological Macromolecules, 2006. **38**(3-5): p. 284-288.
15. Sorensen, G.S., et al., *Structure and ultrastructure of the silk glands and spinneret of Helicoverpa armigera (Hubner) (Lepidoptera : Noctuidae)*. Arthropod Structure & Development, 2006. **35**(1): p. 3-13.
16. Zhou, C.Z., et al., *Fine organization of Bombyx mori Fibroin heavy chain gene*. Nucleic Acids Research, 2000. **28**(12): p. 2413-2419.
17. Zhou, L., et al., *Metal element contents in silk gland and silk fiber of Bombyx mori silkworm*. Acta Chimica Sinica, 2005. **63**(15): p. 1379-1382.
18. Asakura, T., et al., *A repeated beta-turn structure in poly(Ala-Gly) as a model for silk I of Bombyx mori silk Fibroin studied with two-dimensional spin-diffusion NMR under off magic angle spinning and rotational echo double resonance*. Journal of Molecular Biology, 2001. **306**(2): p. 291-305.
19. Takasu, Y., et al., *Identification and characterization of a novel sericin gene expressed in the anterior middle silk gland of the silkworm Bombyx mori*. Insect Biochemistry and Molecular Biology, 2007. **37**(11): p. 1234-1240.

20. Ochi, A., et al., *Rheology and dynamic light scattering of silk Fibroin solution extracted from the middle division of Bombyx mori silkworm*. *Biomacromolecules*, 2002. **3**(6): p. 1187-1196.
21. Zhou, L., et al., *Copper in the silk formation process of Bombyx mori silkworm*. *Febs Letters*, 2003. **554**(3): p. 337-341.
22. Foo, C.W.P., et al., *Role of pH and charge on silk protein assembly in insects and spiders*. *Applied Physics a-Materials Science & Processing*, 2006. **82**(2): p. 223-233.
23. Huang, C.Y., G. Balakrishnan, and T.G. Spiro, *Protein secondary structure from deep-UV resonance Raman spectroscopy*. *Journal of Raman Spectroscopy*, 2006. **37**(1-3): p. 277-282.
24. Kobayashi, M., et al., *Study of gel-sol transition of silk Fibroin*. *Abstracts of Papers of the American Chemical Society*, 2001. **221**: p. U409-U410.
25. Lewis, R.V., *Spider Silk - the Unraveling of a Mystery*. *Accounts of Chemical Research*, 1992. **25**(9): p. 392-398.
26. Lewis, R.V., *Spider Silk, an Ancient Biomaterial for the Future*. *Abstracts of Papers of the American Chemical Society*, 1994. **207**: p. 169-Iec.
27. Gosline, J.M., et al., *The mechanical design of spider silks: From Fibroin sequence to mechanical function*. *Journal of Experimental Biology*, 1999. **202**(23): p. 3295-3303.
28. Craig, C.L., *Evolution of Arthropod Silks*. *Annual Review of Entomology*, 1997. **42**: p. 231-267.
29. Terry, A.E., et al., *pH induced changes in the rheology of silk Fibroin solution from the middle division of Bombyx mori silkworm*. *Biomacromolecules*, 2004. **5**(3): p. 768-772.
30. Vollrath, F. and D.P. Knight, *Liquid crystalline spinning of spider silk*. *Nature*, 2001. **410**(6828): p. 541-548.
31. Magoshi, J., Y. Magoshi, and S. Nakamura, *Mechanism of Fiber Formation of Silkworm*. *Silk Polymers*, 1994. **544**: p. 292-310.
32. Perez-Rigueiro, J., et al., *Mechanical properties of single-brin silkworm silk*. *Journal of Applied Polymer Science*, 2000. **75**(10): p. 1270-1277.
33. Inoue, S., et al., *Silk Fibroin of Bombyx mori is secreted, assembling a high molecular mass elementary unit consisting of H-chain, L-chain, and P25, with a 6 : 6 : 1 molar ratio*. *Journal of Biological Chemistry*, 2000. **275**(51): p. 40517-40528.
34. Brown, D.R., *Introduction: Copper and amyloid fibril formation*. *FEBS journal*, 2007. **274**(15): p. 3755-3755.
35. Ruan, Q.X., et al., *An investigation into the effect of potassium ions on the folding of silk Fibroin studied by generalized two-dimensional NMR-NMR correlation and Raman spectroscopy*. *Febs Journal*, 2008. **275**(2): p. 219-232.
36. Fossey, S.A., et al., *Conformational Energy Studies of Beta-Sheets of Model Silk Fibroin Peptides .1. Sheets of Poly(Ala-Gly) Chains*. *Biopolymers*, 1991. **31**(13): p. 1529-1541.
37. He, S.J., R. Valluzzi, and S.P. Gido, *Silk I structure in Bombyx mori silk foams*. *International Journal of Biological Macromolecules*, 1999. **24**(2-3): p. 187-195.
38. Jelinski, L.W., *Establishing the relationship between structure and mechanical function in silks*. *Current Opinion in Solid State & Materials Science*, 1998. **3**(3): p. 237-245.
39. Marsh, R.E., R.B. Corey, and L. Pauling, *An Investigation of the Structure of Silk Fibroin*. *Biochimica Et Biophysica Acta*, 1955. **16**(1): p. 1-34.
40. Rich, A., *Molecular Configuration of Synthetic and Biological Polymers*. *Reviews of Modern Physics*, 1959. **31**(1): p. 50-60.



41. Sapede, D., et al., *Nanofibrillar structure and molecular mobility in spider dragline silk*. *Macromolecules*, 2005. **38**(20): p. 8447-8453.
42. Putthanarat, S., et al., *Investigation of the nanofibrils of silk fibers*. *Polymer*, 2000. **41**(21): p. 7735-7747.
43. Li, G.Y., et al., *The natural silk spinning process - A nucleation-dependent aggregation mechanism?* *European Journal of Biochemistry*, 2001. **268**(24): p. 6600-6606.
44. Gosline, J.M., M.E. Demont, and M.W. Denny, *The Structure and Properties of Spider Silk*. *Endeavour*, 1986. **10**(1): p. 37-43.
45. Glisovic, A. and T. Salditt, *Temperature dependent structure of spider silk by X-ray diffraction*. *Applied Physics a-Materials Science & Processing*, 2007. **87**(1): p. 63-69.
46. Vollrath, F. and D. Porter, *Spider silk as archetypal protein elastomer*. *Soft Matter*, 2006. **2**(5): p. 377-385.
47. Moore, A.M.F. and K. Tran, *Material properties of cobweb silk from the black widow spider *Latrodectus hesperus**. *International Journal of Biological Macromolecules*, 1999. **24**(2-3): p. 277-282.
48. Perez-Rigueiro, J., et al., *Effect of degumming on the tensile properties of silkworm (*Bombyx mori*) silk fiber*. *Journal of Applied Polymer Science*, 2002. **84**(7): p. 1431-1437.
49. Seydel, T., et al., *Silkworm silk under tensile strain investigated by synchrotron X-ray diffraction and neutron spectroscopy*. *Macromolecules*, 2007. **40**(4): p. 1035-1042.
50. Grubb, D.T. and L.W. Jelinski, *Fiber morphology of spider silk: The effects of tensile deformation*. *Macromolecules*, 1997. **30**(10): p. 2860-2867.
51. Augsten, K., P. Muhlig, and C. Herrmann, *Glycoproteins and skin-core structure in *Nephila clavipes* spider silk observed by light and electron microscopy*. *Scanning*, 2000. **22**(1): p. 12-15.
52. Sponner, A., et al., *Differential polymerization of the two main protein components of dragline silk during fibre spinning*. *Nature Materials*, 2005. **4**(10): p. 772-775.
53. Murthy, N.S., V.A. Kagan, and R.G. Bray, *Effect of melt temperature and skin-core morphology on the mechanical performance of nylon 6*. *Polymer Engineering and Science*, 2002. **42**(5): p. 940-950.
54. Yang, Z., D.T. Grubb, and L.W. Jelinski, *Small-angle X-ray scattering of spider dragline silk*. *Macromolecules*, 1997. **30**(26): p. 8254-8261.
55. Riekkel, C., et al., *Aspects of X-ray diffraction on single spider fibers*. *International Journal of Biological Macromolecules*, 1999. **24**(2-3): p. 179-186.
56. Porter, D., F. Vollrath, and Z. Shao, *Predicting the mechanical properties of spider silk as a model nanostructured polymer*. *European Physical Journal E*, 2005. **16**(2): p. 199-206.
57. Islam, S., et al., *Methods and apparatus for spinning spider silk protein*. United States Patent 7057023, 2006.
58. Scheibel, T. and D. Huemmerich, *Proteins of natural origin and materials made therefrom*. United States Patent 20070196429, 2007.
59. Liivak, O., et al., *A microfabricated wet-spinning apparatus to spin fibers of silk proteins. Structure-property correlations*. *Macromolecules*, 1998. **31**(9): p. 2947-2951.
60. Marsano, E., et al., *Wet spinning of *Bombyx mori* silk Fibroin dissolved in N-methyl morpholine N-oxide and properties of regenerated fibres*. *International Journal of Biological Macromolecules*, 2005. **37**(4): p. 179-188.



- 
61. Corsini, P., et al., *Influence of the draw ratio on the tensile and fracture behavior of NMMO regenerated silk fibers*. Journal of Polymer Science Part B-Polymer Physics, 2007. **45**(18): p. 2568-2579.
  62. Zhu, J.X., H.L. Shao, and X.C. Hu, *Morphology and structure of electrospun mats from regenerated silk Fibroin aqueous solutions with adjusting pH*. International Journal of Biological Macromolecules, 2007. **41**(4): p. 469-474.
  63. Ayutsede, J., et al., *Regeneration of Bombyx mori silk by electrospinning. Part 3: characterization of electrospun nonwoven mat*. Polymer, 2005. **46**(5): p. 1625-1634.
  64. Phillips, D.M., et al., *Regenerated silk fiber wet spinning from an ionic liquid solution*. Journal of Materials Chemistry, 2005. **15**(39): p. 4206-4208.
  65. Rammensee, S., et al., *Assembly mechanism of recombinant spider silk protein*. PNAS, 2008. **105**(18): p. 6590-6595.

## Chapter II- TECHNIQUES

**Résumé de ce chapitre :**

Ce chapitre décrit brièvement le principe des techniques utilisées lors de ce travail de thèse.

Il présente le protocole de préparation des protéines (Fibroïne). Ce protocole enlève la plupart de la séricine sans pour autant dégrader la Fibroïne.

Quelques notions de microfluidique sont introduites et deux cellules de géométries différentes sont comparées. La cellule ayant la géométrie la plus adaptée à la problématique de l'agrégation des protéines a été utilisée dans les expériences qui seront présentées dans les chapitres suivants. Il s'agit d'une géométrie « Tube-dans-Tube », c'est-à-dire d'une cellule constituée d'un tube de section ronde inséré dans un tube de section carrée. Cette géométrie concentrique est plus proche de celle de l'appareil de filage de *B. mori* qu'une cellule de géométrie plane. Elle présente également des avantages techniques.

Les deux principales techniques d'analyses utilisées sont brièvement décrites: la diffusion de rayons X et la spectroscopie Raman.

La diffusion des rayons X permet d'investiguer la structure de la matière. La diffusion aux grands angles (WAXS) inclue la diffraction. Elle renseigne sur les structures amorphes et cristallines à l'échelle de la liaison atomique (Å). La diffusion aux petits angles (SAXS) donne des informations sur la taille et la forme des structures étudiées à l'échelle de la molécule et de l'arrangement moléculaire.

La spectroscopie Raman est une méthode optique également basée sur la diffusion de la lumière. Elle renseigne sur l'état vibrationnel des molécules étudiées. Dans le cas de protéines, elle apporte des informations sur les structures secondaires présentes.

## II.1. Protein preparation

In the case of *B. mori* silk, large quantities of protein are readily available from the cocoons. This is not the case for spider silk, as traditional forced silking methods provide only small quantities of protein [7]. In the future, gene engineering and recombinant protein production methods are expected to provide large quantities of peptides close to spider silk protein, although full length protein has not yet been produced [8-11].

The *B. mori* cocoon silk has to be degummed, that is to say “washed” to remove the sericin coating, and dissolved. This process is named “regeneration”. The classical way to degum silk cocoons is the one used in the silk industry before weaving. It consists of boiling the cocoons in soap and water for several hours. Unfortunately, the Fibroin is degraded by this procedure and the Sericin is only partially removed. Yamada *et al.* [12] improved this protocol by reducing the time and temperature of treatment and increasing the bath volume, which results in preparation of a pure and non-degraded Fibroin solution. This process has been used in this thesis work and is depicted in figure 21.

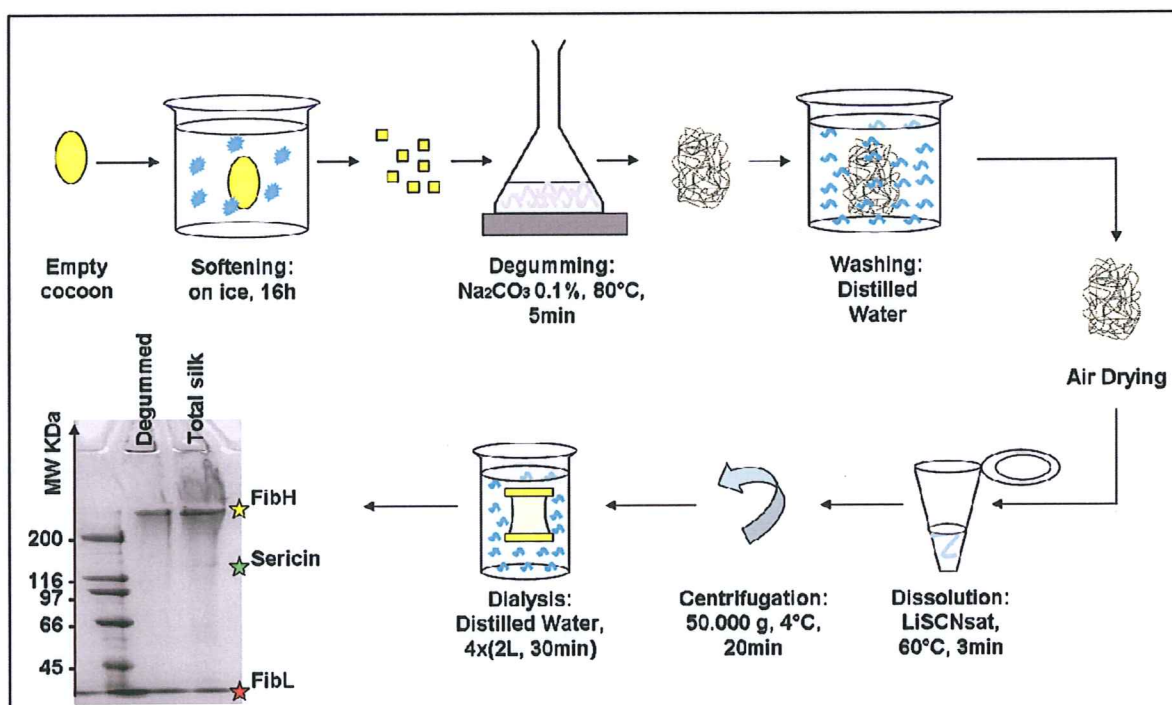


Fig. 21: Protocol for regeneration of the silk dope used in this work. MW: molecular weight.



---

The cocoon is first kept in ice overnight to soften the Sericin. It is then dilacerated and degummed by a 5 minute incubation in a bath of  $\text{Na}_2\text{CO}_3$  0.1%, at 80 °C under agitation. The  $\text{Na}_2\text{CO}_3$  and remaining Sericin are washed away in distilled water, and the Fibroin brins are left to dry overnight and conserved at 4 °C. Less than one week before being used, the Fibroin is dissolved in a saturated solution of LiSCN at 60 °C during 3 minutes under agitation at 20 to 50 mg/mL. As the dissolution is incomplete, the solution must be centrifuged for 20 minutes at 50,000 g and 4 °C to remove the non dissolved residues. Then the solution is dialyzed against 4 baths of 2 L of distilled water during at least 30 minutes per bath without agitation. The Fibroin integrity and the absence of Sericin are checked by denaturizing polyacrylamide gel electrophoresis (SDS-PAGE with  $\beta$ -mercaptoethanol). The Fibroin solution's concentration is measured spectroscopically. At this stage, the solution is very viscous and sensitive to shearing.

## II.2. Microfluidics

Microfluidics is now widely used in biology for two main reasons. First, it allows to minimize the amount of sample used [4]. Secondly, it mimics the flowing conditions which occur in biological environments such as in blood capillaries [13] or silk spinning ducts [14] for instance, by the use of similar flow geometries. The aim of this section is to provide a basic understanding of microfluidic principles [3, 15]. Then, the two microfluidic geometries used in this work: the T-mixer and the Tube-in-Tube chip, will be presented.

The flow of a fluid in a tube is classically described by its Reynolds number ( $Re$ ), calculated as follows:

$$Re = \frac{\rho \cdot \bar{U} \cdot d_h}{\mu} \quad \text{Equation 1}$$

where  $\bar{U}$  is the average flow velocity (m/s),  $\mu$  is the fluid viscosity (Pa.s) and  $\rho$  its density ( $\text{kg/m}^3$ ).  $d_h$  is the hydraulic diameter of the tube, calculated as the ratio of the tube section ( $S$ ) and its wet circumference  $\Pi$ :  $d_h = (4 \cdot S) / \Pi$ . In the case of a round tube,  $d_h$  is the internal diameter, and in the case of a square tube,  $d_h$  is the length of the internal side of the tube. In microfluidics, the tubes are very small: they have at least one dimension smaller than 1 mm. Under these conditions,  $Re \ll 1$  and the viscosity  $\mu$  dominates the flow characteristics. The flow is laminar (also called Stokes flow), which means that the flow velocity is parallel to the wall but is not constant across the channel. The velocity profile is parabolic, equal to 0 at the walls and maximum in the center of the channel (Figure 22). The maximum velocity  $U_{max}$ , at the center of the tube, is proportional to the pressure gradient along the tube.

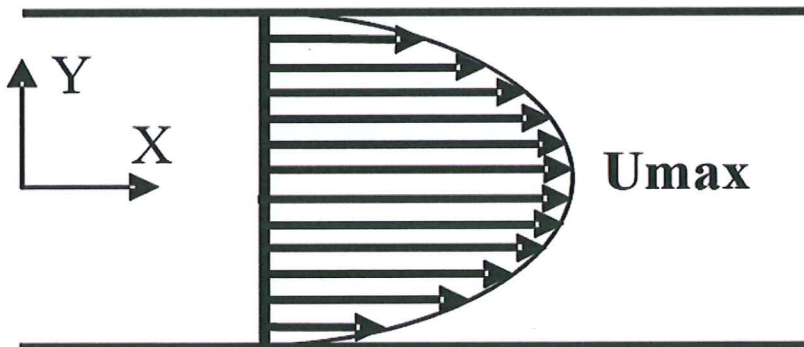


Fig. 22: Scheme of the parabolic velocity profile of a fluid flowing in a microchannel [3].

This scheme allows to introduce the shear forces. The fluid can be imagined as a stacking of very thin layers of liquid, each having a different velocity [16]. The shear forces are caused by the friction between these layers.

In the geometries considered below, the flow being laminar, the mixing of the different co-flowing solutions occurs via a diffusion process.

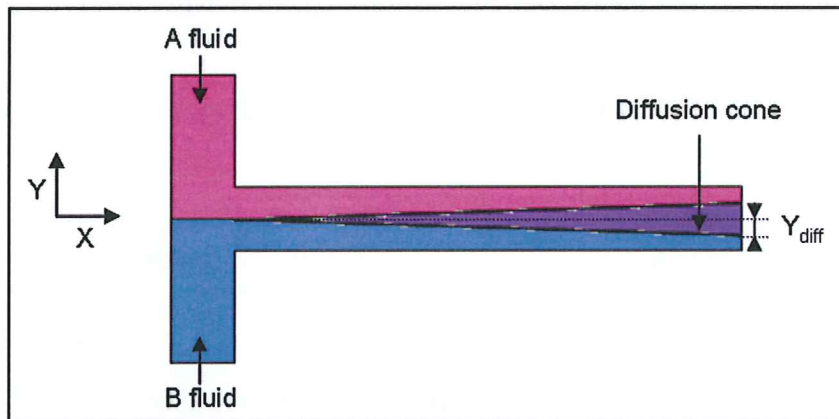


Fig. 23: Scheme of inter-diffusion of co-flowing fluids.

The half width  $Y_{diff}$  (Figure 23) of the diffusion cone at the distance  $X$  from the starting point of the co-flow can be calculated by:

$$Y_{diff}(X) = \sqrt{\frac{2 \cdot D \cdot X}{\bar{U}}} \quad \text{Equation 2}$$

where  $\bar{U}$  is the average flow velocity (m/s) imposed by the injection system, and  $D$  is the diffusion coefficient ( $m^2/sec$ ).

One aim of this thesis work was to develop a microfluidic device which is able to mimic a silk spinning duct. The technical choices were driven by several constraints, the size and required material properties being balanced by the technical availability and/or the cost of development.

Synchrotron radiation scattering experiments demand a window material which is sufficiently transparent to X-rays and does not produce a diffraction pattern with too many discrete reflections. The widely used PDMS is ruled out as a window material because its diffraction pattern is too rich. Borosilicate glass was initially proposed by the Micronit<sup>®</sup> company and adopted for this thesis project because of its compatibility with protein analysis and its broad diffuse scattering signal which can be easily subtracted. Two microfluidic geometries have been tested: a T-shape mixer and a tube-in-tube chip. The T-shape mixer is a commercial device made from borosilicate glass (figure 24) by Micronit<sup>®</sup>. The channels are of about 100 $\mu\text{m}$  diameter and the glass walls around the mixing part are about 50  $\mu\text{m}$  thick.

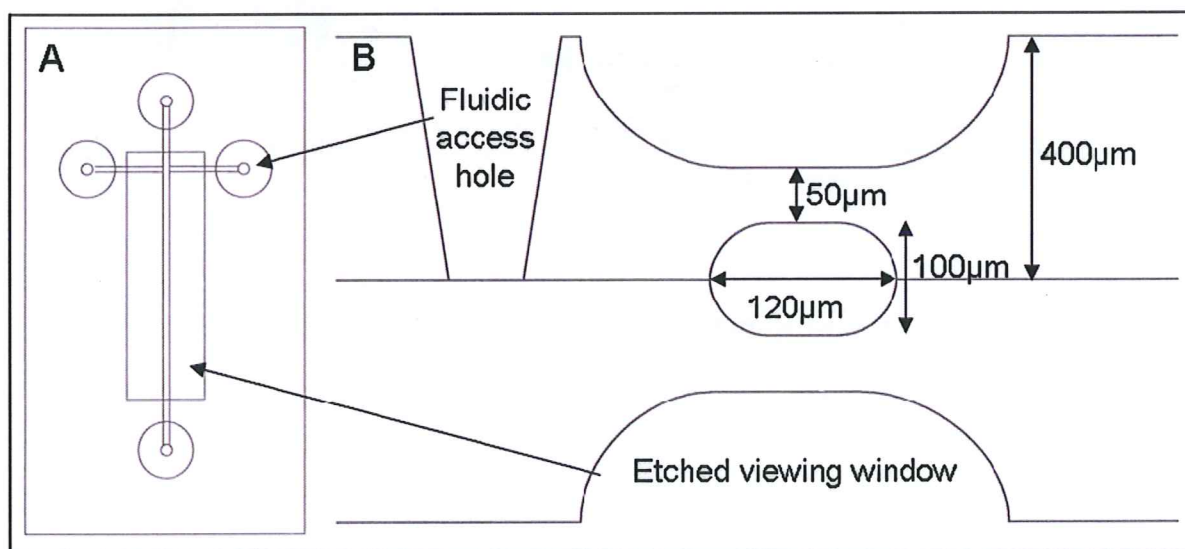


**Fig. 24:** Scheme of the Micronit<sup>®</sup> T-shape mixer. *A:* Front view showing the general geometry. *B:* Cross section showing one of the channels and connection holes.



Two different solutions can be injected: one through the central channel and the other through the lateral channels. At the crossing point, both liquids are co-flowing in a laminar way and mix by diffusion. The width of the central flow is correlated with the ratio of both flow velocities [4, 17] (figure 25).

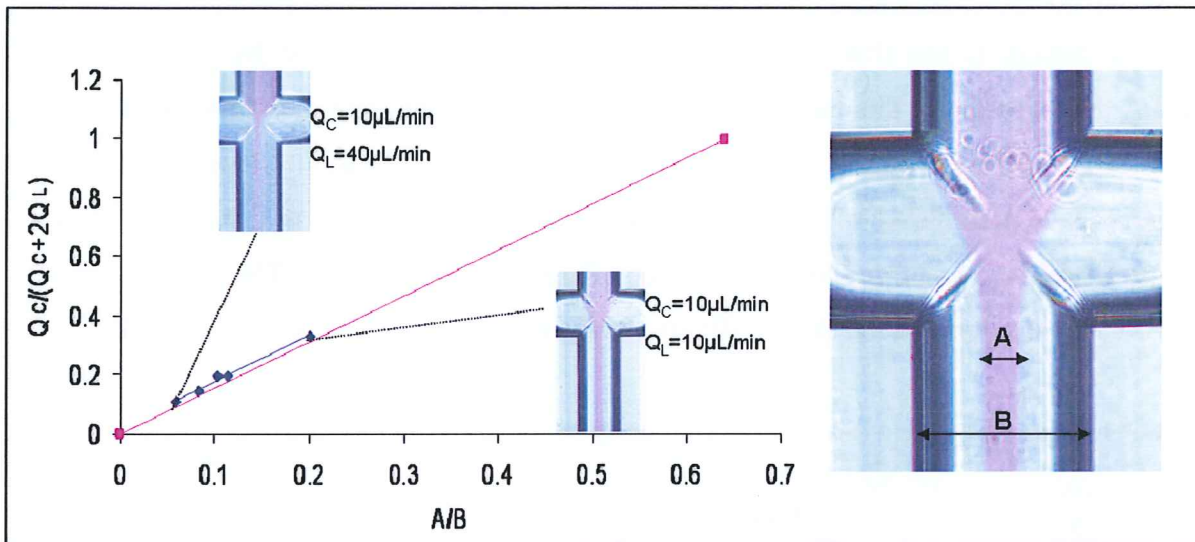


Fig. 25: Proportionality between the flow rates ratio and the width of the central flow. Pink : results from Pfohl et al. [4]; Blue: characterisation of the T-mixer.

Some aggregation experiments have been carried out with this chip, by injecting Fibroin in the central channel and the aggregation buffer in the lateral channels. However, this geometry is not adapted for studying aggregation processes because it was found to be prone to blocking by aggregated material (figure 26).

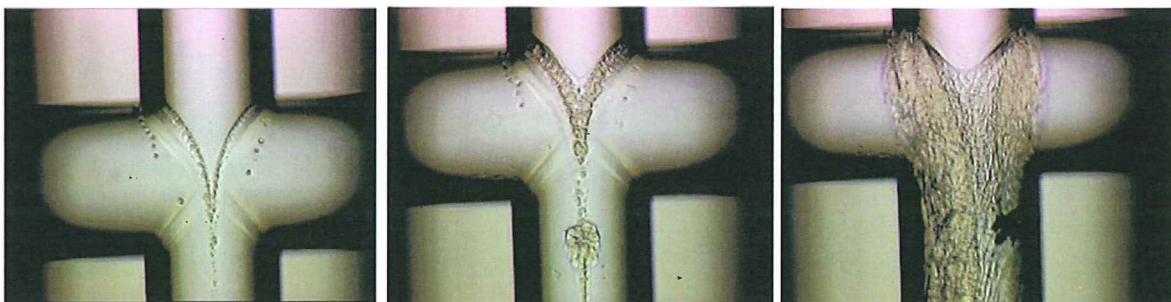
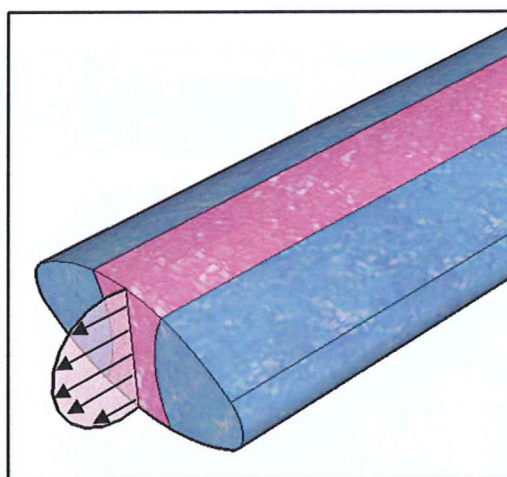


Fig. 26: T-mixer blocking by the Fibroin in contact with Aggregation agent.

This blocking is probably due to the fact that the flow has a parabolic velocity profile (Figure 27). Thus, at the walls, the protein has a very low flow speed and sticks to the glass, generating static aggregates and blocking.



*Fig. 27: The vertical velocity profile of the flow is also parabolic, which induces the presence of protein flowing very slowly close to the walls of the channel.*

A further problem is related to the ovoid cross section of the channels, which is imposed by the etching technology used by Micronit<sup>®</sup>. Consequently, the X-ray path length through the flow varies across the channel which complicates the SAXS/WAXS data analysis. This cell line was abandoned by Micronit<sup>®</sup> because of excessive production costs. The attempt to produce a cell line with silicon body and silicon-nitride window was unsuccessful as the windows were not leak tight. As a result of these difficulties, it has been decided to develop, in collaboration with the Laboratory of future (Rhodia-CNRS-Bordeaux University, Pessac) a less expensive and more tunable device.

A solution to prevent protein aggregation at the walls of the chip is to avoid contact between the protein flow and the walls by surrounding it with the buffer flow. This condition is met in the tube-in-tube geometry [18], where the central tube, carrying the protein, is inside a larger tube carrying the aggregation buffer. The chip developed for this work (figure 28) has a square outside tube, which has two advantages. Firstly, it allows to keep the inner tube exactly centered by selecting an outer diameter close to the inner side dimension of the square outer pipe. Secondly, the thickness of glass plus fluid is constant all across the chip, which

facilitates the background subtraction during X-ray scattering data analysis. Technical details on a set up involving this type of cell are provided in a recent publication (A. Martel *et al.*, *Biomicrofluidics*, in Press, provided in appendix IV).

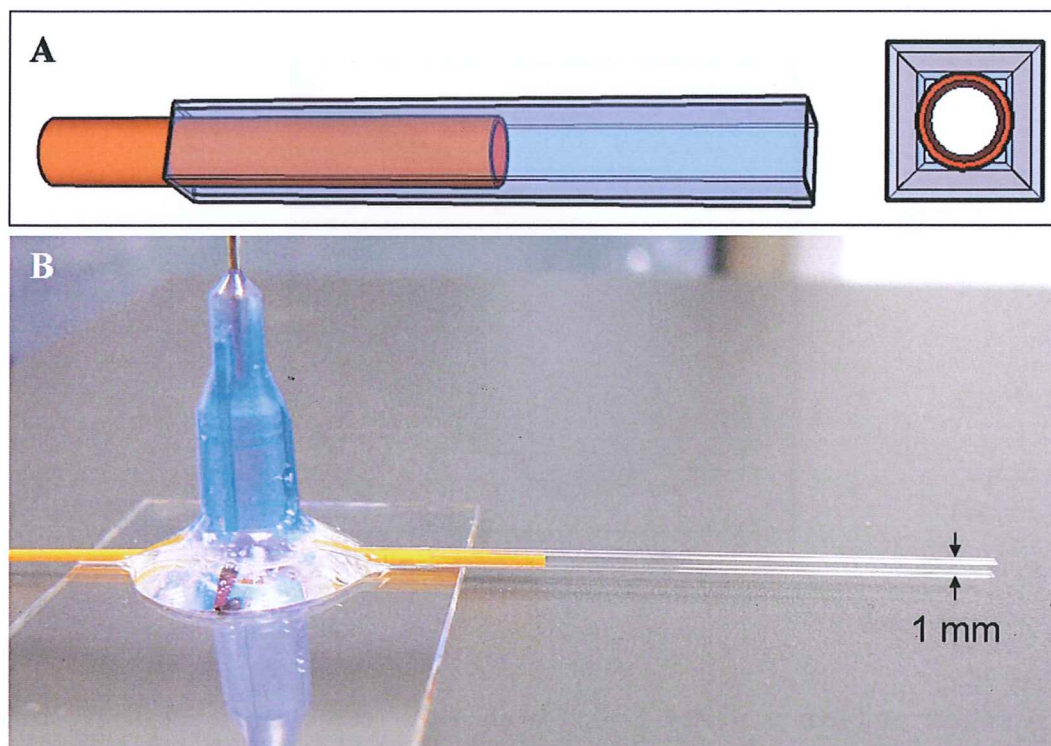


**Fig. 28: Microfluidic Tube-in-tube geometry. A: schemes of the side and bottom views. B: photo of a chip with the connection.**

The outer square tube is made of borosilicate. Its diameter of about 1 mm is determined by the commercial availability of glass square capillaries. To minimize X-ray absorption, its walls were thinned in a 40 % NaOH solution at 80 °C. The thinning speed is around 1 to 2  $\mu\text{m/hr}$ . The minimum wall thickness which could be reached by this technique was 40  $\mu\text{m}$ . At smaller thicknesses, the angles of the tube become very fragile, preventing further manipulation required to assemble the chip. The inner tube is made either of PEEK or borosilicate glass.

After a few minutes of Fibroin artificial spinning with this chip, an aggregation of protein at the end of the inner tube appears and finally blocks the chip. By using a glass inner tube, two surface treatments of this part have been tested: silanisation and polymer coating [19], but they did not have any visible effect on this phenomenon.



### II.3. X-ray scattering

X-ray scattering methods are well adapted to the study of silk fibres as the crystalline fraction provides a characteristic WAXS pattern [20] and the hierarchical silk structure is revealed by SAXS [21, 22]. Although no SAXS/WAXS data have yet been reported on the silk spinning process using microfluidic techniques, such techniques have already been applied to the study of protein conformational changes in biopolymers and proteins [4, 23].

X-rays interact with the matter in three different ways: absorption, scattering and refraction, as does visible light. The absorption effect has to be minimized in the design of sample environments such as microfluidic devices. The refraction effect deviates the incoming monochromatic beam while it passes through the sample. This deviation is very weak for X-rays and can usually be ignored. The scattering effect is used to investigate the structure of the matter and will be further developed. The basic principles of X-ray scattering and diffraction will now be considered using a few geometrical schemes. Small Angle X-ray Scattering (SAXS) and Wide Angle X-ray Scattering (WAXS) methods are extensively used to study hierarchically organized materials. WAXS allows to determine periodic structures down to that atomic scale. SAXS is used to investigate structures at a larger scale, up to about 200 nm.

X-rays can be considered either as photons (light particles) having an energy between 5 and 100 keV, or as an electromagnetic wave having a wavelength of 0.1 to 100 Å. An electromagnetic wave is composed of an electric field and a magnetic field. Only the electric field plays a role in the scattering effect. Thus, in the following descriptions, the X-ray waves will be depicted as electric fields oscillating perpendicularly to the direction of propagation.

To understand the scattering effect, let's first consider the case of a single scattering particle illuminated by a monochromatic beam (Figure 29). Part of the incident beam is scattered in a spherical wave which has the particle for origin, the same wavelength as the incident beam (elastic scattering) and is out of phase by  $\pi$ .



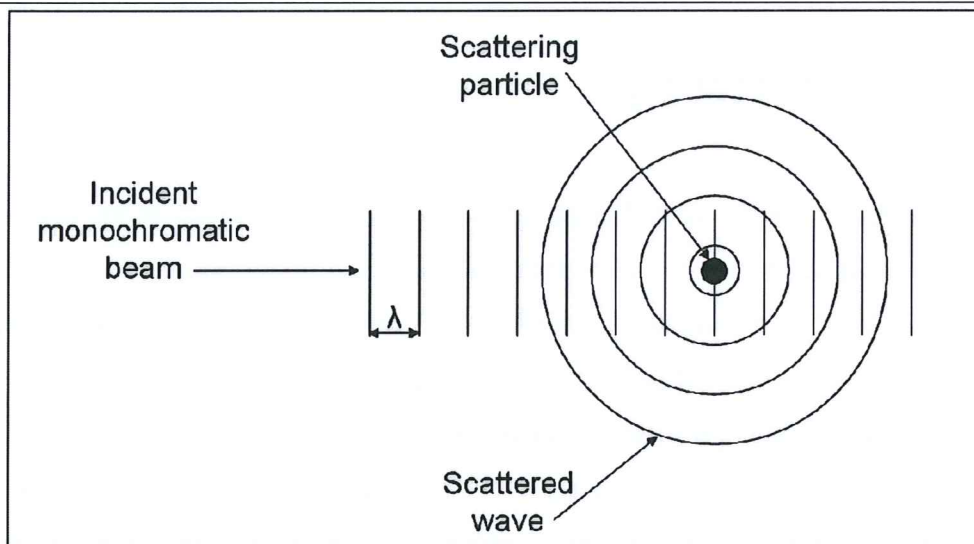


*Fig. 29: Scattering by a single particle [1].*

In the case of X-ray scattering experiments, the scattering particles are electrons of the sample. The observation point is very far from the sample compared to the distance between the scattering particles. Thus the scattering directions which are parallel in the vicinity of the scattering particles appear like a point at the observation plane. The angle between the incident beam and the direction of observation is  $2\theta$ . The spherical scattered wave emerging from a first interaction between the incident beam and a particle can be secondly scattered by another particle of the sample, but this secondary scattering is negligible compared to the primary scattering. If we consider the sample as a group of single scattering particles (figure 30), the scattered waves from each particle have the same wavelength. Therefore, they interfere, and a composed scattered wave rises: the diffracted X-rays. The phase difference between the scattered waves depends on the length difference of the X-ray pathways in each individual scattering situation :  $x_1+y_1$  or  $x_2+y_2$  on figure 30. It conditions the amplitude of the composed scattered wave.

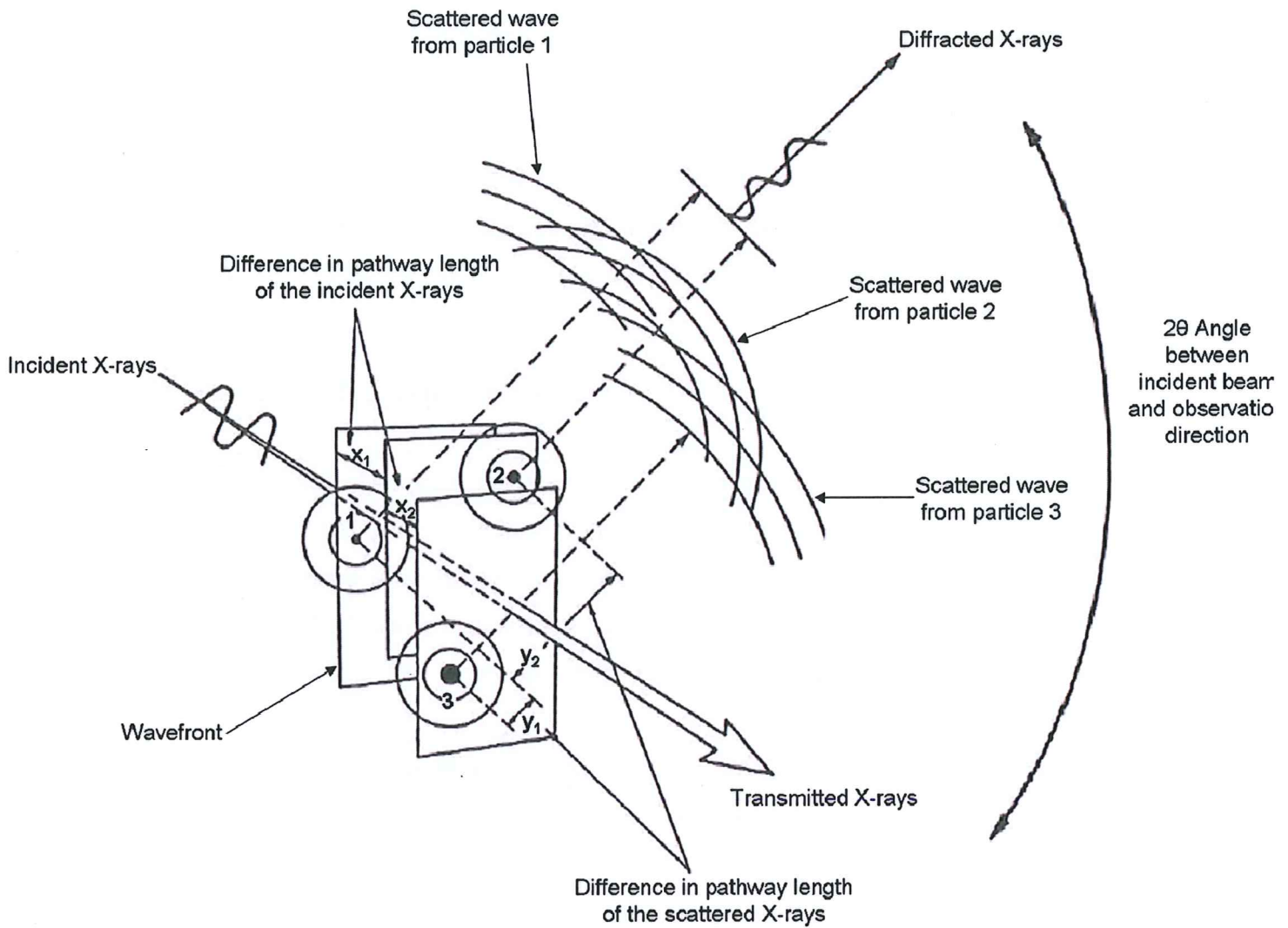


Fig. 30: Scattering by several particles, interference and diffraction [1].

If the difference in the X-rays pathway length is equal to an integer number ( $n$ ) of wavelengths (Bragg condition), the interferences between scattered waves are constructive.

In a crystal, the particles are strictly ordered in a repetitive way along the three axis of the crystal. Therefore, the difference in the pathway length is repeated along each of these axis and the addition of these constructive interferences gives rise to intense peaks at the observation point called Bragg reflections. Thus, in practice, when a Bragg reflection is observed, knowing the wavelength and the scattering angle  $2\theta$ , it is possible to calculate a characteristic repetitive distance  $d$  inside the crystal by the Bragg equation:

$$n \lambda = d.2.\sin(\theta) \quad \Leftrightarrow \quad \sin(\theta) = n\lambda/2.d \quad \text{Equation 3}$$

If the matter is more disordered, differences in the X-ray pathway lengths are more variable, and consequently the scattering intensity is more diffuse. The smaller  $2\theta$  is, the larger the  $d$  distance observed is. As a consequence, SAXS experiments (small  $2\theta$ ) give information on the general shape and size of large structures, whereas the WAXS experiments (large  $2\theta$ ) give information on smaller structures down to inter-atomic distances inside crystals.

In the case of a crystal, the unit cell is the smallest entity which is sufficient to describe the whole structure. It is delimited by three unit vectors,  $a$ ,  $b$  and  $c$ , which lengths and directions depend on the structure. The macroscopic crystal is assembled from this unit cell through a 3D translational symmetry. The characteristic distances ( $d$ ) inside the crystal are combinations of these three unit vectors. Each Bragg peak corresponds to a characteristic distance. In the example illustrated in figure 31, the 210 reflection corresponds to the (210) plane, which cuts the  $a$ -axis vector at  $1/2$ , the  $b$ -axis vector at  $1$ , and is parallel to the  $c$ -axis vector. The  $[210]$  vector is normal to the (210) plane. Its length  $2\pi/d$  ( $d$  being the distance between the plans parallel to the (210) plane).

Figure 31 shows an indexed WAXS pattern [5, 24] of a silk fibre on which the contribution of the crystalline domains (Bragg peak) and the amorphous phase (diffuse scattering) can be clearly distinguished. Materials which WAXS pattern shows a mixture of Bragg peaks and diffuse scattering are called “semicrystalline”. This is the case for many polymers and biopolymers.



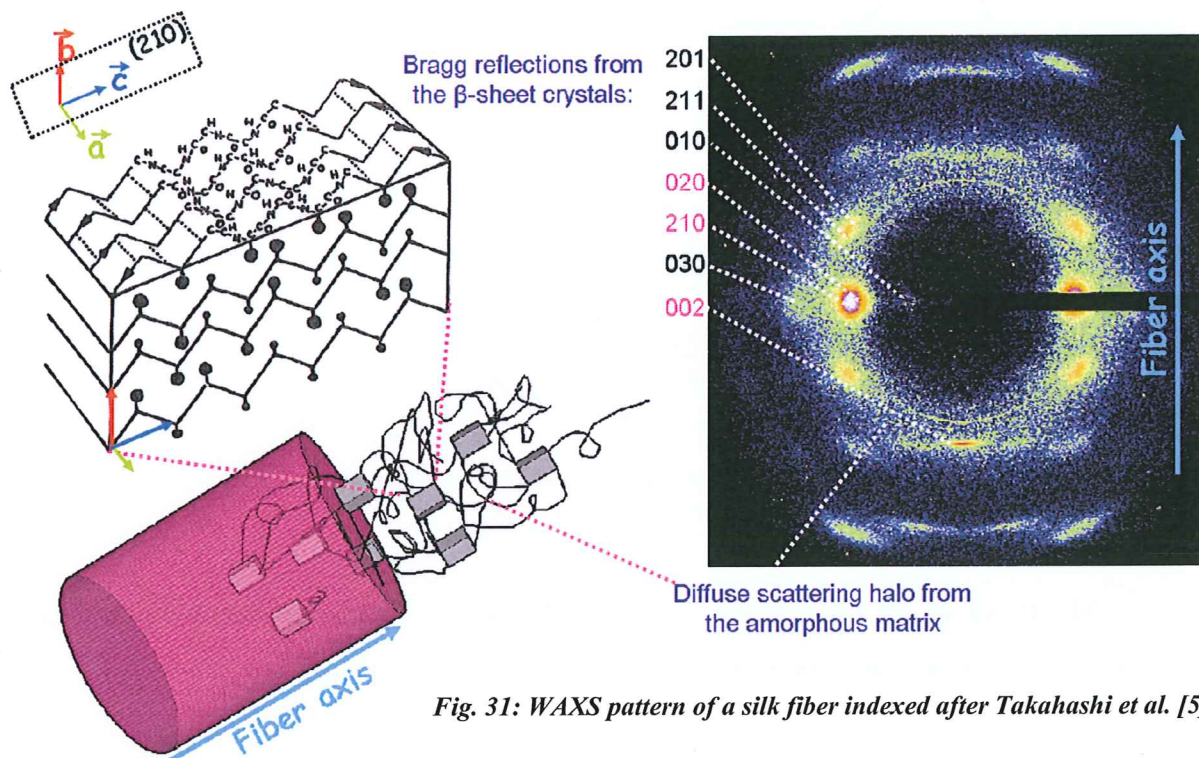
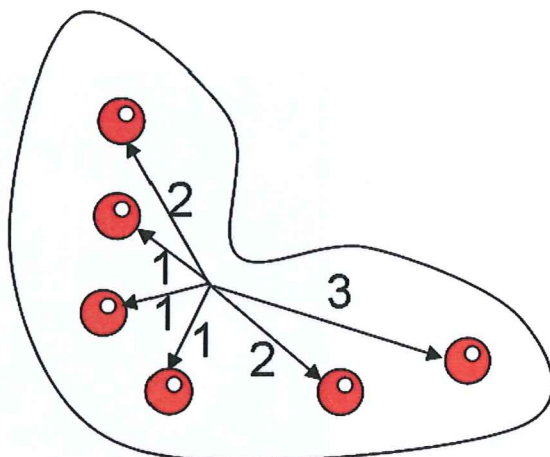


Fig. 31: WAXS pattern of a silk fiber indexed after Takahashi et al. [5].

The waves scattered close to the incident beam constitute the SAXS pattern. The analysis of SAXS pattern provides information on the large-scale organization of materials, as well as the size and shape of molecules [25]. For instance, the nano-fibrillar structure of the spider dragline silk can be deduced from the presence of peaks on its anisotropic SAXS pattern, along the fibre axis direction [26].

In the case of solution scattering reported below, the SAXS patterns are isotropic so they can be azimuthally averaged over  $360^\circ$  to a 1-dimensional SAXS profile. The analysis of the solution scattering patterns of a protein allows to get information on its size via the determination of the Radius of gyration ( $R_g$ ) [27].  $R_g$  corresponds to the square root of the average squared distance of each atom from the centre of the molecule [2]. For the example shows figure 32, the  $R_g = [(1^2 + 1^2 + 1^2 + 2^2 + 2^2 + 3^2) / 6]^{1/2} = 1.82$





**Fig. 32:** The radius of gyration  $R_g$  is the square root of the average squared distance of each atom from the centre of the molecule [2].

The  $R_g$  value can be deduced from a SAXS pattern of a monodisperse dilute solution of this molecule using the Guinier law :

$$I = I_0 \exp\left(-\frac{1}{3}q^2 R_g^2\right) \quad \text{Equation 4}$$

where  $q = 2\pi/d$  and  $I$  is the SAXS intensity. This law holds for  $q < 1/R_g$  and requires dilute solutions without interference between molecules. As shown on figure 33, the plot of  $\ln(I)$  as a function of  $q^2$  (called Guinier plot) has a linear part. The slope  $S$  of this part is proportional to the square of  $R_g$ :

$$S = -1/3 \cdot R_g^2 \quad \text{Equation 5}$$

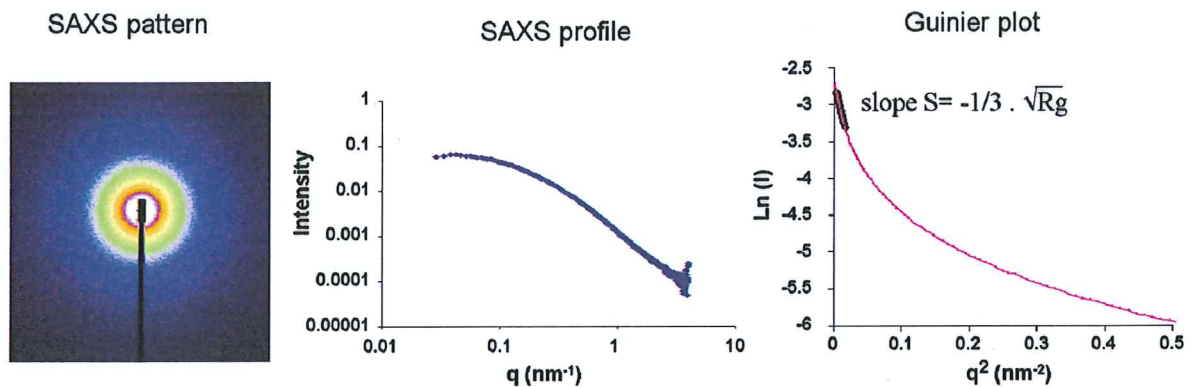


*Fig. 33: Fibroin solution SAXS pattern, SAXS profile and Guinier plot. The slope of the linear region where  $q < 1/R_g$  gives the  $R_g$  value.*

The SAXS profile also gives information about the shape of the molecule [28]. The pair distance distribution function, which gives for each distance the probability to find it inside the molecule, can be calculated.

In recent years, the determination of the shape of molecules in solution has become of particular interest for biological applications. The shape of Fibroin in solution has been recently determined [28]. This method will be discussed in more details below.

## II.4. Raman spectroscopy

Raman spectroscopy is a technique used to investigate the molecular structure of many different materials [29]. In biology, it can reveal the secondary structure of protein [30]. In this thesis work, Raman spectroscopy has been used as a complementary tool to determine the molecular structure of silk fibre [6, 31, 32]. The basic principle of this technique is presented below [33].

When a sample is illuminated with a monochromatic laser, some light is scattered in all directions. A large part of this scattered light has the same wavelength as the incident beam (Rayleigh scattering) and the rest has different wavelengths (Raman scattering). The light scattered at different wavelengths than the incident beam constitutes the Raman spectrum and the different wavelengths represented in this spectrum are called Raman bands. They correspond to an energy transfer between the incident beam and the molecules in the material. The Raman spectrum is specific of the molecular structure of the material. As depicted figure 34, the molecules can either take some energy from the light as vibration energy or loose their vibration energy, transmitting it to the light. The corresponding Raman bands appear at larger wavelength (Stokes) or lower wavelength (anti-Stokes).

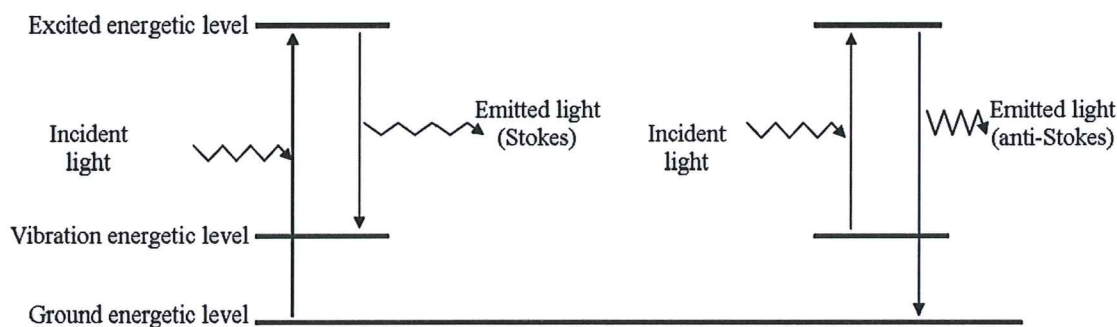


*Figure 34: Principle of Raman spectroscopy.*

The Raman scattered light is weak compared to the Rayleigh scattered light [29]. To gather the Raman signal of a sample, a special microscope, able to filter out the light having the same wavelength as the incident beam, is necessary. Figure 35 shows a simplified scheme of such a microscope. The incident laser beam is focalized on the sample through a lens, a dichroic mirror and an objective. The dichroic mirror (or beam splitter) is wavelength-

selective: it reflects light having certain wavelengths (the laser in our case) and is transparent for others. The sample exposed scatters light in all directions. In the so-called backscattering geometry, part of this light which passes through the objective, is filtered with regard to the band or wavelength range asked by the user and focalized on a detector system.

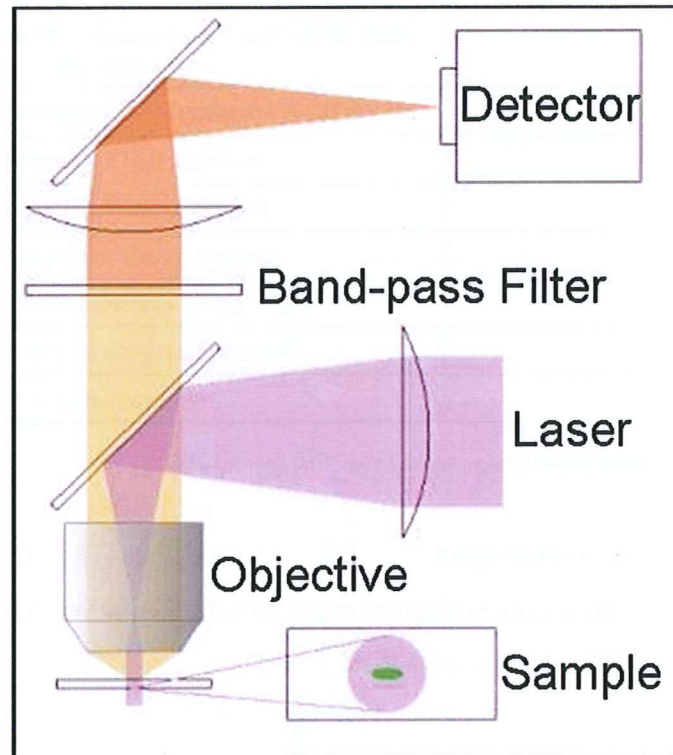


*Figure 35: Simplified scheme of a Raman microscope.*

Silk has a lot of different molecular bonds, therefore its Raman spectra is complex. Nevertheless, some of its bands are assigned to particular bonds, often by comparison to the spectra of simpler materials (table 2) [6].



<i>B. mori</i> Raman bands (wavenumber (cm <sup>-1</sup> ))	Assignment
1693 shoulder	amide I, mainly C=O stretching in antiparallel $\beta$ -sheets
① 1665	amide I, C=O stretching in $\beta$ sheets
1614	aromatic ring stretching in F and Y
1447	CH <sub>2</sub> bending in poly(AG)
1401	COO <sup>-</sup> symmetrical stretching in D and E, CH <sub>2</sub> w in poly(AG)
1263	amide III: N-H in-plane bending, C=O in-plane bending, C $\alpha$ -C stretching
1229	amide III, A symmetry: N-H in-plane bending, CH <sub>2</sub> twisting
1207	aromatic C-H in-plane bending
② 1083	C $\alpha$ -C $\beta$ stretching, CH <sub>3</sub> rocking
1001	aromatic ring breathing in F and Y
881	stretching of C $\alpha$ -C stretching, C-N, C=O and C $\alpha$ -C $\beta$
③ 828 and 853	Fermi resonance of the Y doublet
642	aromatic ring in Y

Table 2: Summary of Raman band assignment from Silk spectra [6].

Figure 36 shows the Raman spectrum of *B. mori* silk fiber. The three regions written in blue are of particular interest concerning the study of Silk formation. The analysis of this spectrum will be developed further in section IV.2.

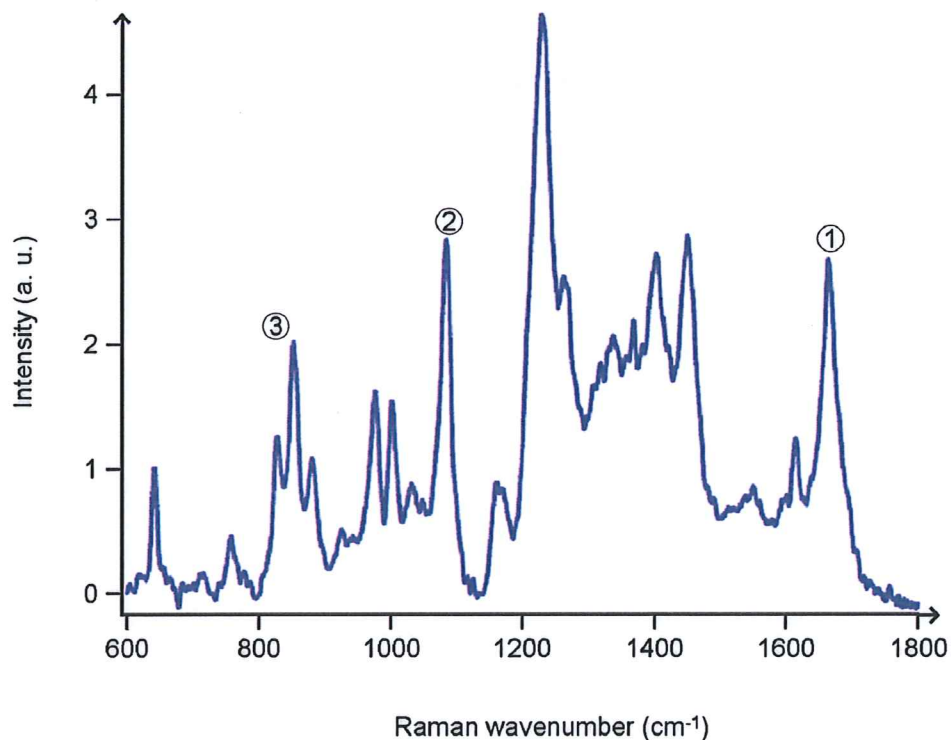


Figure 36: Raman spectrum of a *B. mori* silk fiber. The three marked positions correspond to the band in blue in table 2 which are analyzed in section IV.2.

## Bibliography

1. Kakudo, K. and K. Kasai, *X-ray Diffraction by Polymers*. Kodansha scientific books, 1972.
2. Squires, A., *SR summer school talk*. [www.src.ac.uk/summer-school06/summerschool06\\_talks/Squires%20Chester%2006.ppt](http://www.src.ac.uk/summer-school06/summerschool06_talks/Squires%20Chester%2006.ppt), 2006.
3. Sarrazin, F., *Microréacteurs diphasiques pour le développement rapide des procédés*. Thesis, 2006.
4. Pfohl, T., et al., *Trends in microfluidics with complex fluids*. Chemphyschem, 2003. **4**(12): p. 1291-1298.
5. Takahashi, Y., M. Gehoh, and K. Yuzuriha, *Structure refinement and diffuse streak scattering of silk (Bombyx mori)*. International Journal of Biological Macromolecules, 1999. **24**(2-3): p. 127-138.
6. Rousseau, M.E., et al., *Study of protein conformation and orientation in silkworm and spider silk fibers using Raman microspectroscopy*. Biomacromolecules, 2004. **5**(6): p. 2247-2257.
7. Work, R.W. and P.D. Emerson, *An Apparatus and Technique for the Forcible Silking of Spiders*. Journal of Arachnology, 1982. **10**(1): p. 1-10.
8. Heslot, H., *Artificial fibrous proteins: A review*. Biochimie, 1998. **80**(1): p. 19-31.
9. Hinman, M.B., J.A. Jones, and R.V. Lewis, *Synthetic spider silk: a modular fiber*. Trends in Biotechnology, 2000. **18**(9): p. 374-379.
10. Scheibel, T., *Spider silks: recombinant synthesis, assembly, spinning, and engineering of synthetic proteins*. Microb Cell Fact, 2004. **3**(1): p. 14.
11. Scheibel, T. and D. Huemmerich, *Proteins of natural origin and materials made therefrom*. United States Patent 20070196429, 2007.
12. Yamada, H., et al., *Preparation of undegraded native molecular fibroin solution from silkworm cocoons*. Materials Science & Engineering C-Biomimetic and Supramolecular Systems, 2001. **14**(1-2): p. 41-46.
13. Arnaud, C.H., *Mimicking biological systems*. Chemical & Engineering News, 2007. **85**(37): p. 14-19.
14. Knight, D.P. and F. Vollrath, *Liquid crystals and flow elongation in a spider's silk production line*. Proceedings of the Royal Society of London Series B-Biological Sciences, 1999. **266**(1418): p. 519-523.
15. Bruus, H., *Theoretical microfluidics*. Oxford University Press, 2007.
16. Couarraze, G. and J.L. Grossiord, *Initiation à la Rhéologie*. Technique et Documentation (Lavoisier), 1983.
17. Knight, J.B., et al., *Hydrodynamic focusing on a silicon chip: Mixing nanoliters in microseconds*. Physical Review Letters, 1998. **80**(17): p. 3863-3866.
18. Utada, A.S., et al., *Monodisperse double emulsions generated from a microcapillary device*. Science, 2005. **308**(5721): p. 537-541.
19. McPherson, T.B., H.S. Shim, and K. Park, *Grafting of PEO to glass, nitinol, and pyrolytic carbon surfaces by gamma irradiation*. Journal of Biomedical Materials Research, 1997. **38**(4): p. 289-302.
20. Fraser, R.D.B. and T.P. MacRae, *Conformation in fibrous proteins*. New York: Academic Press, 1973.

21. Riekkel, C. and F. Vollrath, *Spider silk fibre extrusion: combined wide- and small-angle X-ray microdiffraction experiments*. International Journal of Biological Macromolecules, 2001. **29**(3): p. 203-210.
22. Yang, Z., D.T. Grubb, and L.W. Jelinski, *Small-angle X-ray scattering of spider dragline silk*. Macromolecules, 1997. **30**(26): p. 8254-8261.
23. Pollack, L., et al., *Compactness of the denatured state of a fast-folding protein measured by submillisecond small-angle x-ray scattering*. Proceedings of the National Academy of Sciences of the United States of America, 1999. **96**(18): p. 10115-10117.
24. Marsh, R.E., R.B. Corey, and L. Pauling, *An Investigation of the Structure of Silk Fibroin*. Biochimica Et Biophysica Acta, 1955. **16**(1): p. 1-34.
25. Baruchel, J., et al., *Neutron and Synchrotron Radiation for Soft Condensed Matter studies*. Les éditions de Physique, 1993.
26. Sapede, D., et al., *Nanofibrillar structure and molecular mobility in spider dragline silk*. Macromolecules, 2005. **38**(20): p. 8447-8453.
27. Putthanarat, S., et al., *Investigation of the nanofibrils of silk fibers*. Polymer, 2000. **41**(21): p. 7735-7747.
28. Roessle, M., et al., *Structural evolution of regenerated silk fibroin under shear: Combined wide- and small-angle x-ray scattering experiments using synchrotron radiation*. Biopolymers, 2004. **74**(4): p. 316-327.
29. Wen, Z.Q., *Raman spectroscopy of protein pharmaceuticals*. Journal of Pharmaceutical Sciences, 2007. **96**(11): p. 2861-2878.
30. Berjot, M., J. Marx, and A.J.P. Alix, *Determination of the Secondary Structure of Proteins from the Raman Amide-I Band - the Reference Intensity Profiles Method*. Journal of Raman Spectroscopy, 1987. **18**(4): p. 289-300.
31. Monti, P., et al., *Raman spectroscopic studies of silk fibroin from Bombyx mori*. Journal of Raman Spectroscopy, 1998. **29**(4): p. 297-304.
32. Lefevre, T., M.E. Rousseau, and M. Pezolet, *Protein secondary structure and orientation in silk as revealed by Raman spectromicroscopy*. Biophysical Journal, 2007. **92**(8): p. 2885-2895.
33. Long, D.A., *The Raman effect. A unified treatment of the theory of raman scattering by molecules*. Wiley and sons, 2002.



## **CHAPTER III- ARTIFICIAL SPINNING OF SILK: Fibroin Aggregation**



**Résumé de ce chapitre :**

Dans ce chapitre, deux expériences de SAXS sont présentées :

Tout d'abord la caractérisation de la Fibroïne en solution aqueuse est réalisée. Cette expérience a lieu en conditions standards. Elle permet, grâce aux programmes de traitement de données GNOM et DAMMIN, de reconstituer la forme approximative de la molécule en solution. La forme de la Fibroïne serait plutôt allongée, et ressemble à la forme proposée par Roessle *et al.* [1] pour cette protéine après cisaillement.

Dans un deuxième temps, l'agrégation de la Fibroïne est suivie lors de la formation d'une fibre dans une cellule microfluidique. Cette expérience est réalisée grâce à la cellule Tube-dans-Tube présentée chapitre II avec des vitesses de flux faibles. Dans ces conditions, le mélange est presque total 7,5 mm après le point de mélange. L'état d'agrégation est observé en 15 points distribués tous les 0,5 mm. Le premier point est 0,5 mm après la fin du tube interne (ou point de mélange). Les résultats montrent que 0.5 mm après le point de mélange, soit après 1,7 sec de diffusion, une partie de la Fibroïne est déjà en partie agrégée. L'ordre de grandeur de la taille des agrégats se situe autour de 100 nm. La Fibroïne sous forme agrégée est plus compacte qu'en solution diluée. Les agrégats semblent également se compacter dans un second temps.

Ces résultats soulèvent l'hypothèse d'une agrégation en deux temps: d'abord la formation des agrégats dans lesquels la Fibroïne adopte une conformation plus compacte qu'en solution, puis une compaction de ces agrégats.

## III.1. Experiments

### III.1.1. Fibroin characterization by SAXS

Fibroin in solution (see protocol presented in Chapter I- Techniques) has been characterized by SAXS on ID02 [2]. Experiments were carried out using a flow-through cell as shown in figure 37. The cell consists of a glass tube connected to a motorized syringe through Teflon tubing. First water (which is the solvent of Fibroin) and then a Fibroin solution were pushed through the cell. This allows the best possible background subtraction. In order to reduce the volume of protein solution, a drop of the solution is deposited at the tube entrance and pushed using the syringe, which is filled with air. The motorization makes it possible to move the drop a little bit between each exposure to always have fresh solution in the beam. Then the tube is extensively washed with water and the following solution can be analyzed. The temperature is maintained at 25 °C using a Peltier element.

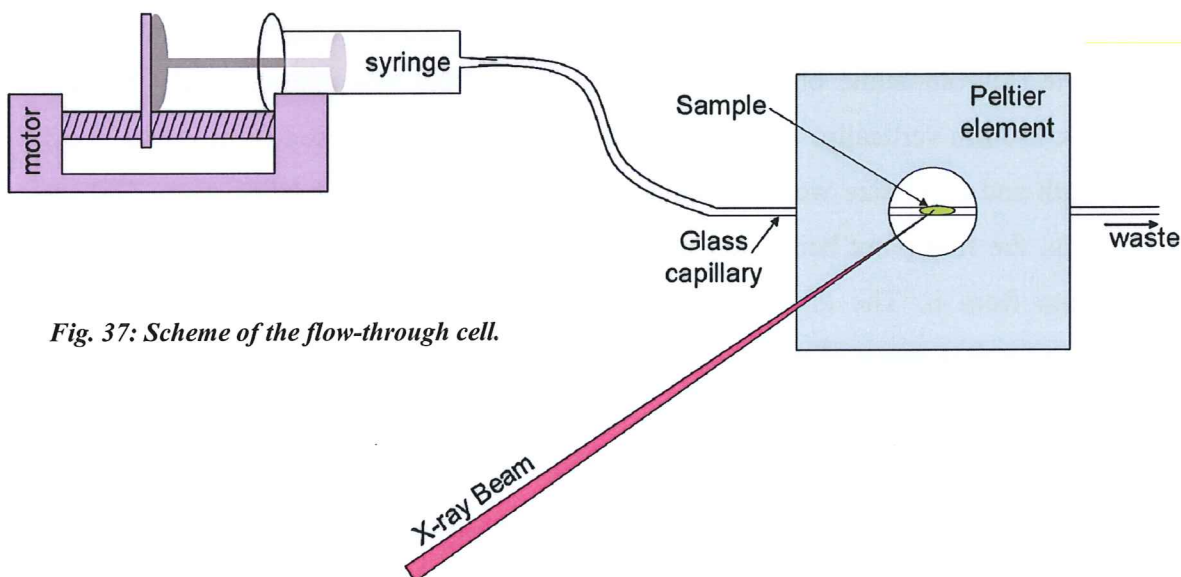


Fig. 37: Scheme of the flow-through cell.

Three concentrations of Fibroin and three sample-detector distances were used: the scattering of Fibroin solutions at 1 mg/mL, 5 mg/mL and 9.3 mg/mL were measured at 1,5 and 3 meters from the detector and the 1 mg/mL solution was also measured at 5m. The wavelength was 0.995 Å, the exposure time was 0.1 sec and the beam size was approximately 300 x 300  $\mu\text{m}^2$ . The detector used was a Frelon camera [3] with pixels of 50 x 50  $\mu\text{m}^2$ . The pixels were binned 4 x 4. For each sample, three patterns were recorded and averaged.

### III.1.2. Fibroin Aggregation observed by SAXS

In a separate experiment, SAXS measurement were done *in situ* during Fibroin aggregation with the Tube-in-Tube chip presented in Chapter II [4] and appendix IV. The set up used is schematically shown in figure 38.

#### III.1.2.1. Solutions

The Fibroin concentration was 8.96 mg/mL. The aggregation buffer was a pH2 solution with 20 mM of  $H_3PO_4$  and 100 mM of NaCl. The flow rates were 500  $\mu$ L/hr for Fibroin and water and 660  $\mu$ L/hr for pH2 buffer. At these flow rates, the velocity of the fluids before the mixing point is the same: 1300 mm/hr. The velocity after the mixing point is lower: 1052 mm/hr (see calculation in appendix III). The mixing by diffusion starts at the end of the internal tube, also called the mixing point.

#### III.1.2.2. Small-angle X-ray scattering:

The exposure times were 1 sec for the background ( $H_2O$ -Buffer mixing) and 0.5 sec for the sample (Fibroin-acidic buffer mixing). The beam size was approximately 100  $\mu$ m horizontally x 150  $\mu$ m vertically. The sample detector distance was close to 5 m (4.99123 m), the wavelength and pixel size were the same as above. A pattern was taken every 500  $\mu$ m along the chip, the first point being 500  $\mu$ m under the end of the internal tube and the last point, 7.5 mm from it. The distance range from the mixing point (0.5 mm to 7 mm) corresponded to a time range of mixing of 1.7 s to 25.7 s. After 7.5 mm of travel inside the chip, the protons have diffused by about 390  $\mu$ m inside the protein flow (calculated from equation 2, taken  $D = 3.10^{-9} \text{ m}^2/\text{s}$  [5]). The radius of the Fibroin flow before diffusion is less than 390  $\mu$ m (radius of the inner flow in the hypothesis of a flat velocity profile), which implies that the process of mixing by diffusion is complete 7.5 mm downstream from the mixing point (see calculation in appendix III). The background scattering was first determined by injecting the aggregation buffer and water instead of Fibroin. Two series of patterns were taken from this experiment ( $H_2O$ - Acidic Buffer mixing), then, the  $H_2O$  injection was stopped and the Fibroin injection started. Once the thread formation started, two series of sample patterns were taken. The background series were averaged and subtracted from the two sample series. Finally, the flow was stopped and a pattern of the end of the aggregation was taken a moment later.

### III.1.2.3. Data analysis:

The patterns are azimuthally regrouped into 1-dimensional intensity profiles and analyzed by the “unified fit model” using the Irena package for IGOR software [6].

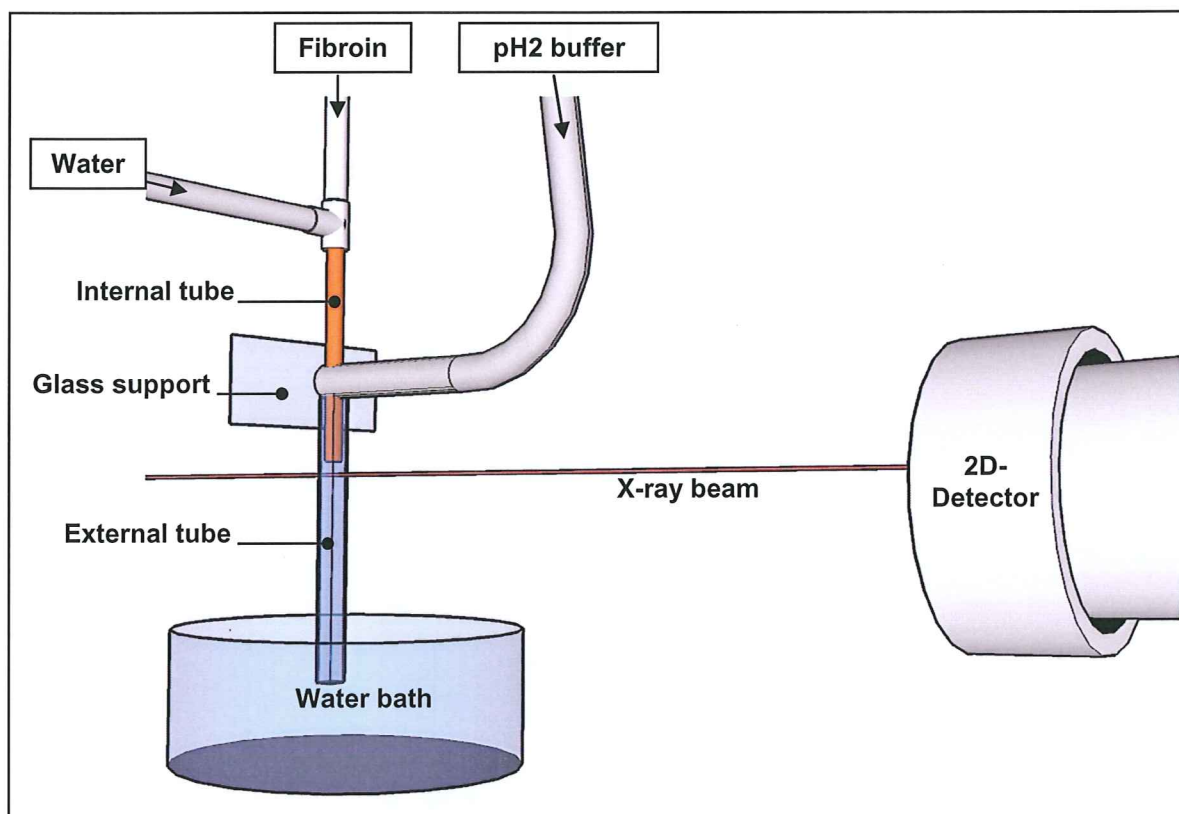


*Fig. 38: Scheme of the setup used for artificial spinning with the Tub-in-Tube chip and in situ SAXS and WAXS experiments. Each solution is injected by an independent syringe pump.*



## III.2. Results and Discussion

### III.2.1. Fibroin characterization by SAXS

Three protein concentrations were used: 1 mg/mL, 5 mg/mL and 9.3 mg/mL. The Fibroin integrity was checked by denaturing poly-acrylamide gel electrophoresis (SDS-PAGE Figure 39).

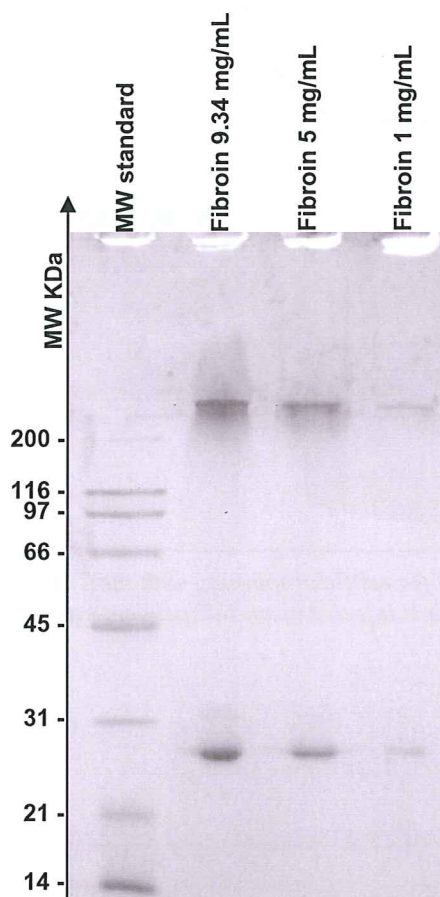


*Fig. 39 : SDS-PAGE of the three fibroin solutions used for SAXS.*

The 2-dimensional SAXS patterns are azimuthally regrouped after masking the beamstop image and the data coming from exposures at different sample-detector distances are merged.

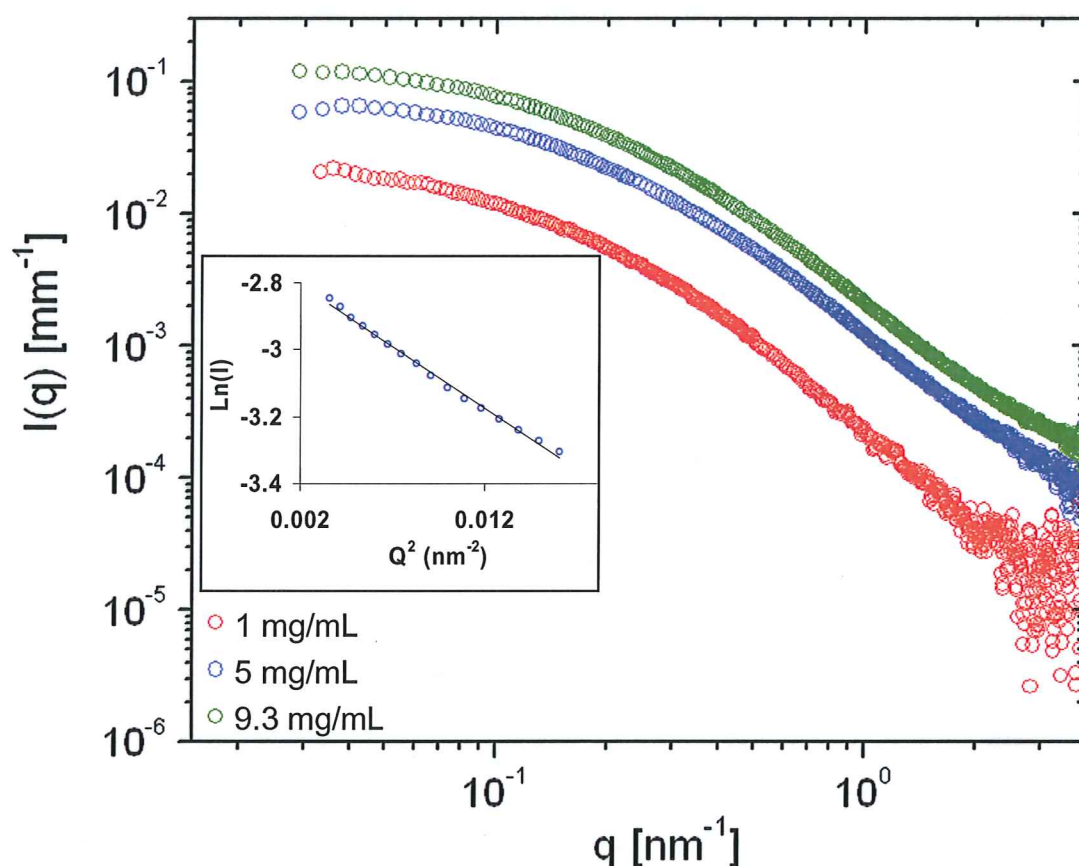


*Fig. 40: SAXS profile of the fibroin solutions of three different concentration. The insert shows the Guinier plot of the 5 mg/mL solution profile.*

A logarithmic plot of the intensity  $I(q)$  as a function of  $q$  ( $\text{nm}^{-1}$ ) is shown in Figure 40. This representation enables us to appreciate the absence of aggregates by the fact that the profiles reach a plateau at low  $q$ . The insert of the figure 40 is the Guinier plot of the data from the 5 mg/mL solution. From these data, the Fibroin radius of gyration is deduced: 10.8 nm. The hydrodynamic radius [7] measured by dynamic light scattering (DLS) is around 16 nm. The radius of gyration is lower than the hydrodynamic radius because it does not include the water shell around the protein. The 5 mg/mL data are further analyzed using specialized programs: IFTc [8], GNOM and DAMMIN programs [9, 10]. First, the IFTc program estimates the maximum length which can be found in the protein ( $d_{\text{max}}$ ) and the pair distance distribution function of the protein, providing that the data are collected from a diluted solution without interference effects. GNOM is also able to calculate the pair distance distribution function (cf chapter II) but the user has to estimate himself the maximum length which can be found in the protein ( $d_{\text{max}}$ ) although IFTc gives an estimation of it. However, the output file of GNOM is readable by DAMMIN, which is not the case of IFTc file. Figure 41

shows that the pair distance distribution function  $[p(r)]$  calculated by IFTc and GNOM (providing the  $d_{\max} = 38$  nm, estimated by IFTc) are similar. The radii of gyration  $R_g$  estimated by the two programs are also very similar: 11.42 nm for IFTc and 11.106 nm for GNOM.

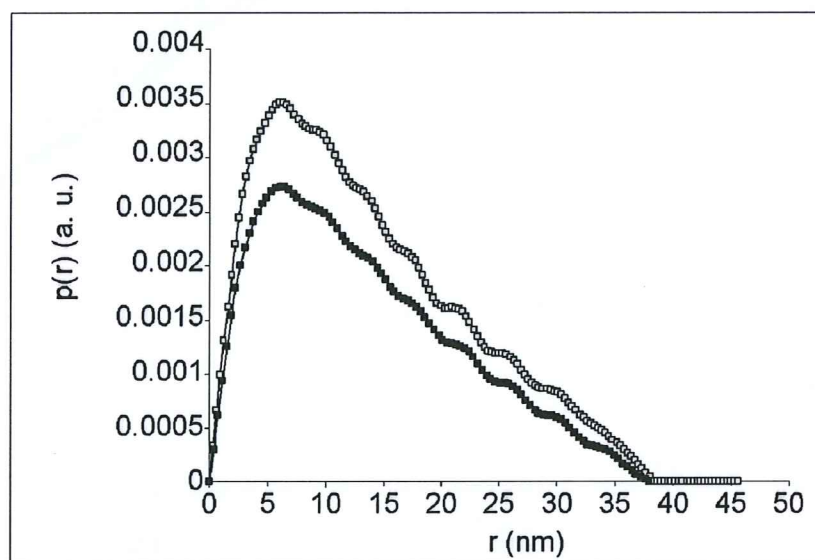


**Fig. 41:** Pair distance distribution function calculated by IFTc (white squares) and GNOM (black squares) from the 5gm/mL solution SAXS data, using  $d_{\max} = 38$  nm.

From the GNOM output file, DAMMIN program simulates the Fibroin shape shown figure 42. DAMMIN builds a sphere having a diameter of  $d_{\max}$  made of densely packed dummy atoms (at the positions marked by green dots in Figure 42). At each step of the simulated annealing, each atom is assigned either to the molecule of interest (pink spheres) or to the solvent and the theoretical SAXS profile is calculated, until a configuration which fit the experimental data while minimizing the interfacial area is found [11]. This method presents the advantage of being *ab initio*, which means that no model shape is required, minimizing the risk of error introduced by a wrong model.

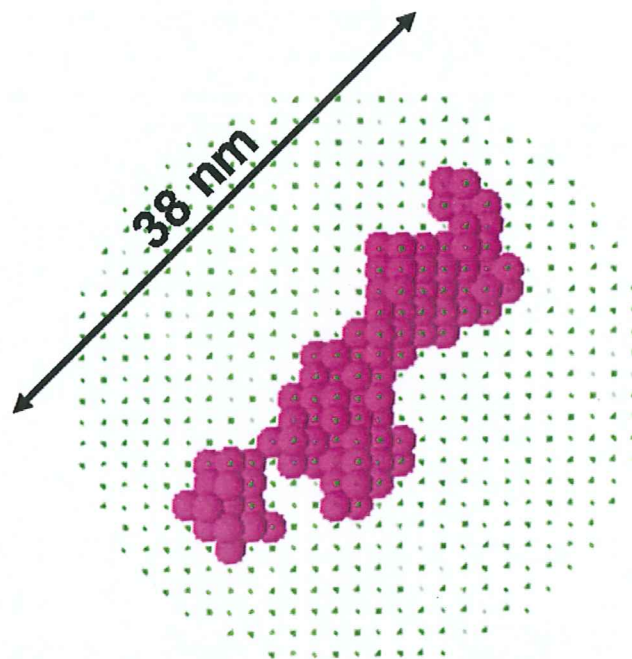


*Fig. 42: Fibroin shape modelised by DAMMIN.*

The  $R_g$  and  $d_{max}$  calculated here are larger than the values found by Roessle *et al.* [1]. In that previous study, protein integrity was not checked and the protocol used for protein preparation included long steps at high temperature. The difference in protein integrity between these two studies might be the main reason for this disagreement.

It has to be noted that the shape of Fibroin simulated by DAMMIN from the same pair distance distribution function can vary slightly. Figure 43 illustrates the solution instability by giving four solutions. The “slow” mode was chosen as it is advised for elongated proteins. The present results are based on a fit of the whole curve.



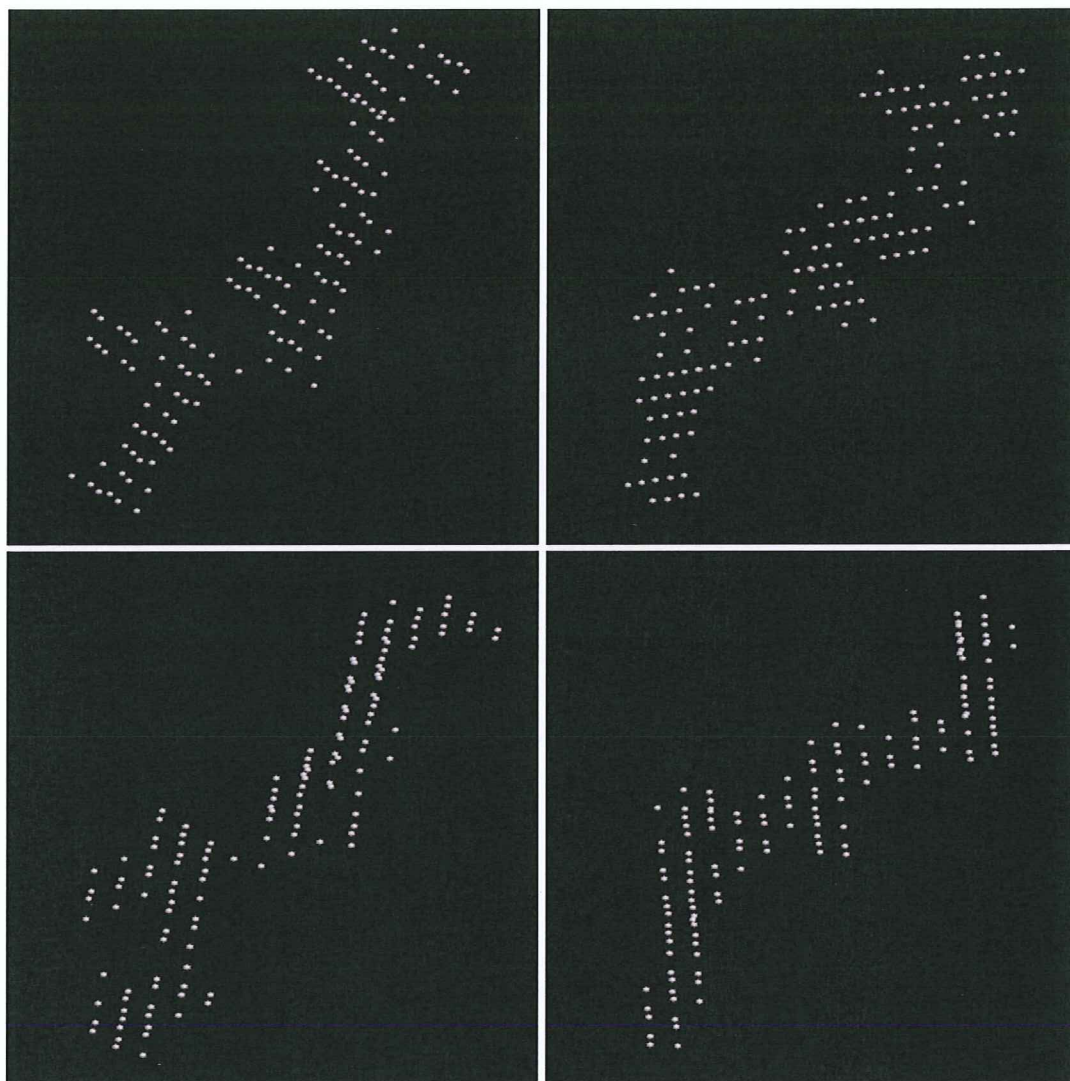


*Fig. 43: Different DAMMIN solutions from the same GNOM out file.*

### III.2.2. Fibroin Aggregation observed by SAXS

We will now analyse the SAXS results obtained during Fibroin aggregation. Figure 44 shows the profile of three of the sample patterns from the first series. In these patterns, one can distinguish two different scales: the individual protein level in the Q range from 0.01 to 0.05  $\text{\AA}^{-1}$ , and the aggregates level in the Q range from 0.002 to 0.006  $\text{\AA}^{-1}$ . This suggests that the aggregation does not occur in a fractal way, on the contrary, the aggregates have a defined size.

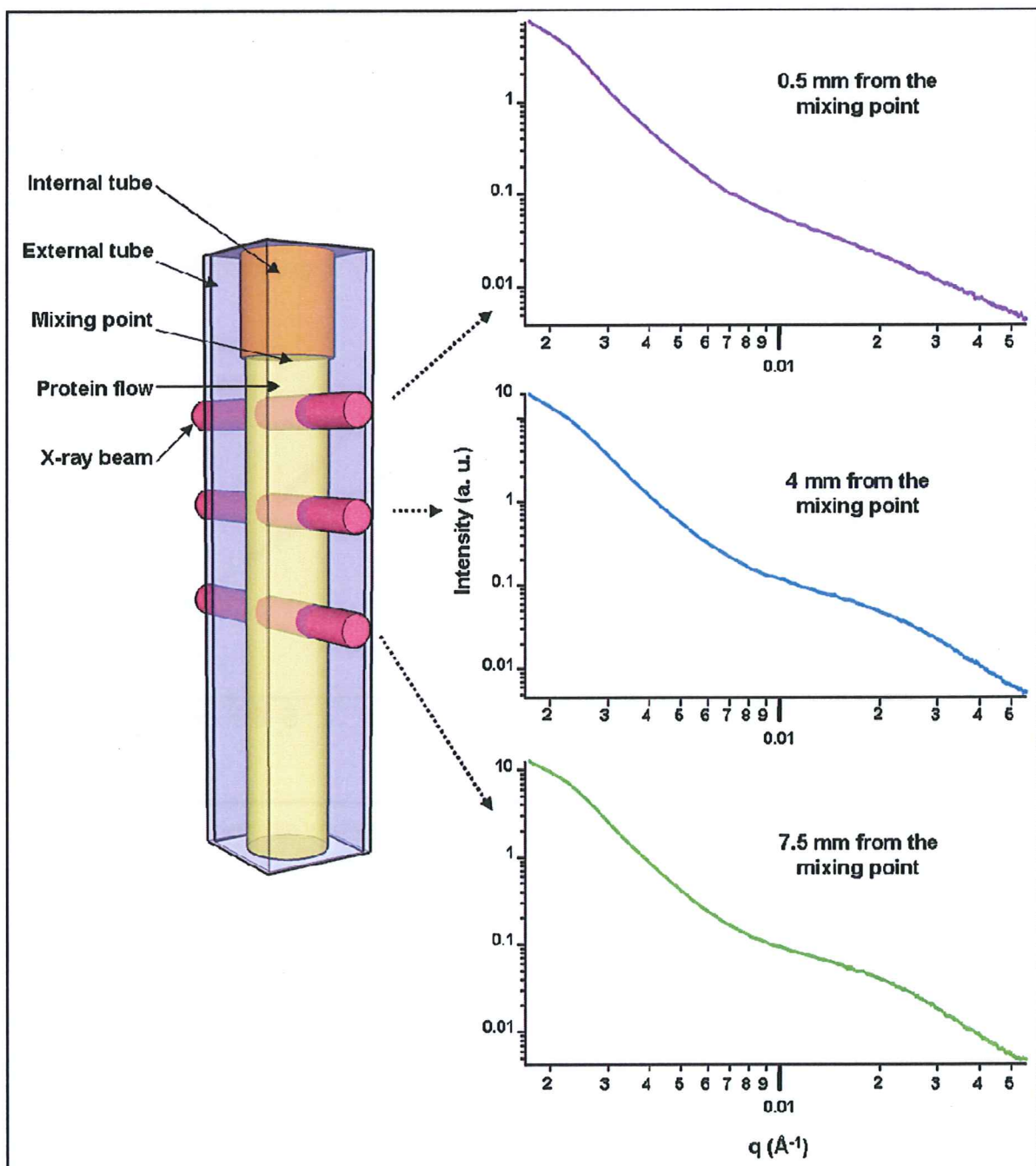
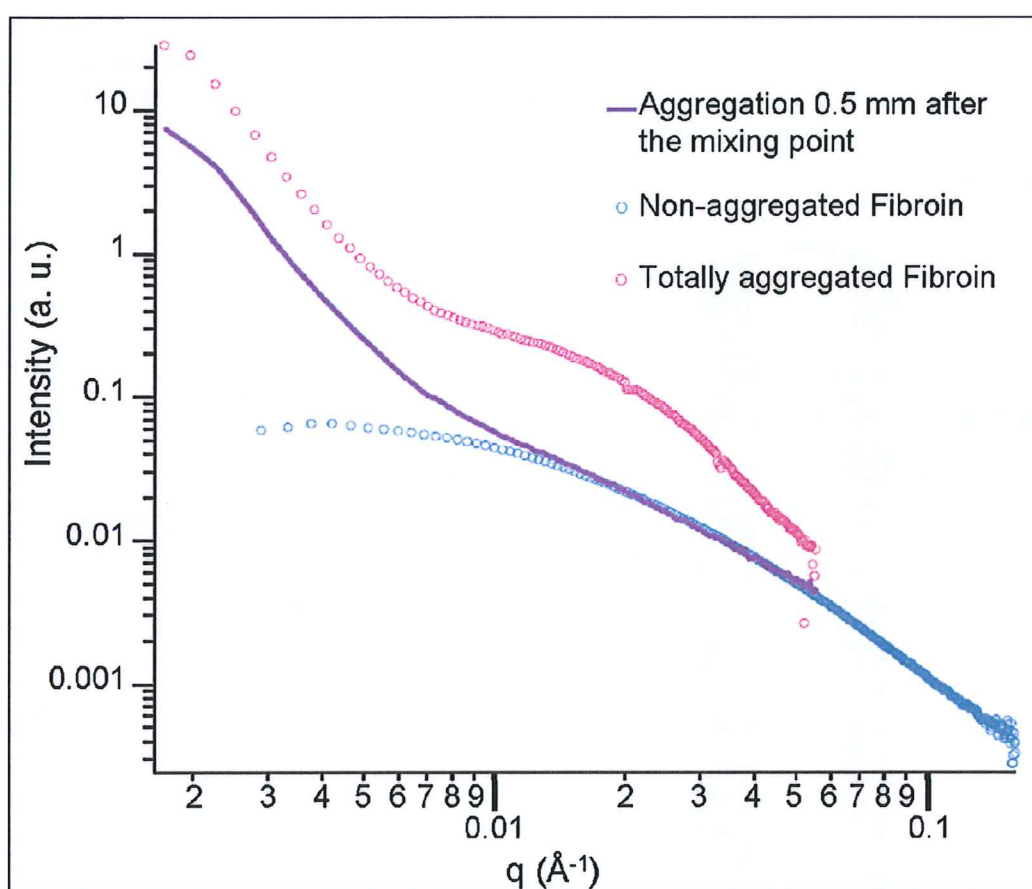


Fig. 44: Fibroin aggregation in the tube-in-tube chip followed by SAXS.

Aggregation is already observed at the first point of measurement, 0.5 mm after the end of the inner tube (mixing point). The individual protein level of the scattering curve at 0.5 mm from the mixing point is very similar to the non-aggregated Fibroin scattering curve (figure 45). This is probably due to the fact that the region mixed by diffusion is very thin compared to the Fibroin flow. Consequently, the signal from the non-mixed protein dominates this  $q$ -range. Along the protein's travel in the mixing channel, the shape of the curve at the individual protein  $q$ -range changes.



*Fig. 45: Comparison of SAXS profiles of Fibroin in different states of aggregation.*

Figure 46 shows that the apparent  $R_g$  of the Fibroin decreases during the first part of the aggregation process. This apparent  $R_g$  is an average of the  $R_g$  of the aggregated Fibroin and of the Fibroin which has not yet been mixed with the acidic buffer. The progressive decrease of the apparent  $R_g$  value of Fibroin probably reflects the advance of mixing and the proportion of the non-aggregated Fibroin and the aggregated Fibroin. At the end of the mixing

process, the apparent  $R_g$  stabilizes. It can be deduced that all the Fibroin proteins are in an aggregated state and their  $R_g$  is around 8 nm.

An indicative  $R_g$  value is also calculated for the aggregates but should not be taken as an absolute value as the part of the curve closest to the lowest  $q$  values is not in the Guinier range ( $q < 1/R_g$ ). The aggregates seem to compact at the end of the mixing process (between 6 and 8 mm from the mixing point).

The data are averages of the value from the two series of sample patterns. The error bars represent their standard deviation.

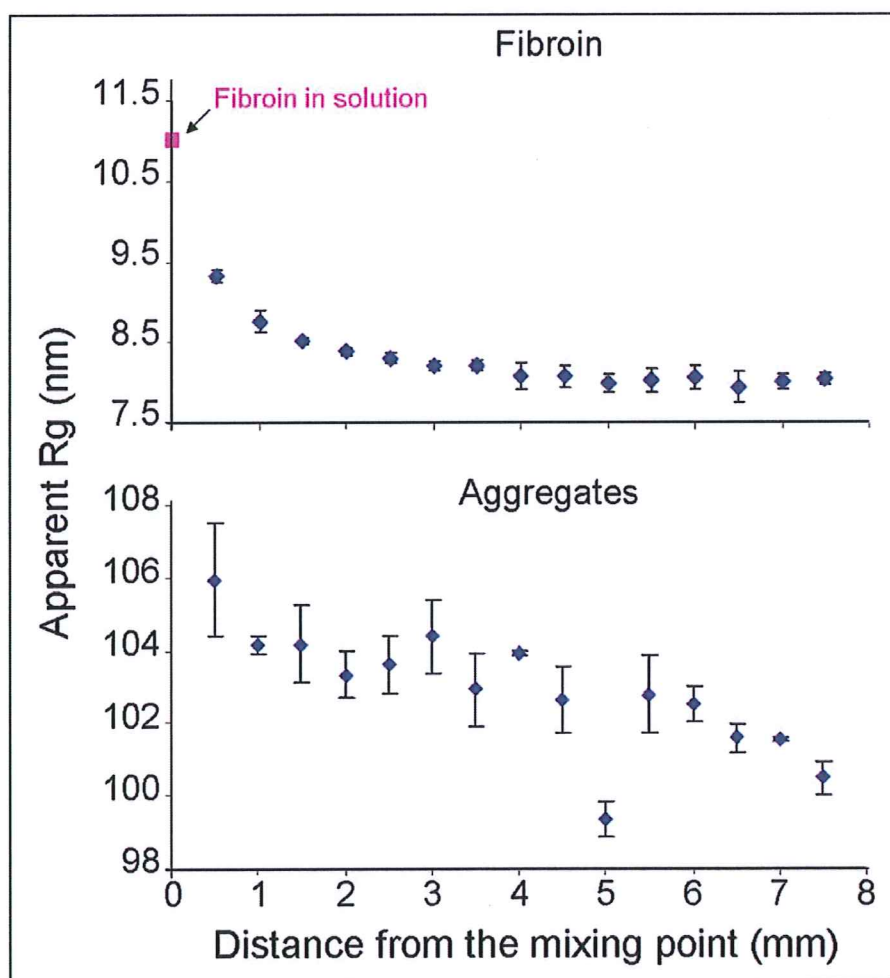


Fig. 46: Evolution of  $R_g$  of fibroin and aggregates along the aggregation process.

These experiments allow the observation of the first steps of Fibroin aggregation until the end of the diffusion mixing process. The aggregation process was observed between 1.7 s to 25.7 s of mixing. The results confirm that the pH decrease induces an aggregation of the Fibroin. The indicative  $R_g$  of these aggregates is around 100 nm. In these aggregates, the



Fibroin is in a compacted form which has an  $R_g$  of 8 nm. In a second step, these aggregates compact slightly as their  $R_g$  decreases from 104 nm to 100 nm. The precise shape of the aggregates remains to be calculated as it has been done in the case of another amyloid peptide [12].

## Bibliography

1. Rossle, M., et al., *Structural evolution of regenerated silk fibroin under shear: Combined wide- and small-angle x-ray scattering experiments using synchrotron radiation*. Biopolymers, 2004. **74**(4): p. 316-327.
2. Narayanan, T., O. Diat, and P. Bosecke, *SAXS and USAXS on the high brilliance beamline at the ESRF*. Nuclear Instruments & Methods in Physics Research Section a-Accelerators Spectrometers Detectors and Associated Equipment, 2001. **467**: p. 1005-1009.
3. Labiche, J.C., et al., *Invited article: The fast readout low noise camera as a versatile x-ray detector for time resolved dispersive extended x-ray absorption fine structure and diffraction studies of dynamic problems in materials science, chemistry, and catalysis*. Review of Scientific Instruments, 2007. **78**(9): p. -.
4. Utada, A.S., et al., *Monodisperse double emulsions generated from a microcapillary device*. Science, 2005. **308**(5721): p. 537-541.
5. Sarrazin, F., *Microréacteurs diphasiques pour le développement rapide des procédés*. Thesis, 2006.
6. Sztucki, M., T. Narayanan, and G. Beaucage, *In situ study of aggregation of soot particles in an acetylene flame by small-angle x-ray scattering*. Journal of Applied Physics, 2007. **101**(11).
7. Malvern Instrument, [www.silver-colloids.com/Papers/hydrodynamic-radius.pdf](http://www.silver-colloids.com/Papers/hydrodynamic-radius.pdf).
8. Hansen, S., *Simultaneous estimation of the form factor and structure factor for globular particles in small-angle scattering*. Journal of Applied Crystallography, 2008. **41**: p. 436-445.
9. Semenyuk, A.V. and D.I. Svergun, *Gnom - a Program Package for Small-Angle Scattering Data-Processing*. Journal of Applied Crystallography, 1991. **24**: p. 537-540.
10. Konarev, P.V., et al., *ATSAS 2.1, a program package for small-angle scattering data analysis*. Journal of Applied Crystallography, 2006. **39**: p. 277-286.
11. Svergun, D.I., *Restoring low resolution structure of biological macromolecules from solution scattering using simulated annealing (vol 76, pg 2879, 1999)*. Biophysical Journal, 1999. **77**(5): p. 2896-2896.
12. Vestergaard, B., et al., *A helical structural nucleus is the primary elongating unit of insulin amyloid fibrils*. Plos Biology, 2007. **5**(5): p. 1089-1097.



## **CHAPTER IV- ARTIFICIAL SPINNING OF SILK: Fibroin Conversion**



**Résumé de ce chapitre :**

Ce chapitre présente des expériences complémentaires de spectroscopie Raman et de diffraction des rayons X à grands angles (WAXS) effectuées sur les mêmes échantillons. Des fibres de Fibroïne ont été produites en utilisant la cellule Tube-dans-Tube présentée chapitre II. Le débit de chaque solution a été choisi de façon à ce que le flux de Fibroïne soit aminci lors du mélange avec le flux de tampon acide pour mimer l'amincissement de l'appareil de filage de *B. mori*. Ces fibres ont été laissées dans le bain de collection, c'est-à-dire dans l'eau, pour une durée variable allant jusqu'à 24h, avant d'être séchées à l'air ambiant. Leur analyse par spectroscopie Raman révèle une transition conformationnelle progressive d'une structure Silk I hydratée à une structure Silk II hydratée durant le bain. Cette transition est caractérisée par :

- l'augmentation de la proportion de feuillets  $\beta$  parmi les structures secondaires représentées,
- le changement d'environnement des tyrosines passant d'un environnement hydrophobe à un environnement plus hydrophile où le groupement hydroxyle de la chaîne latérale est impliqué dans une forte liaison hydrogène,
- la formation de cristallites de feuillets  $\beta$  empilés, observée par WAXS.

Cette transition ne présente pas d'états intermédiaires mais une coexistence des deux formes hydratées. Une grande proportion des tyrosines se trouvant dans les régions riches en alanine et glycine de la séquence de FibH, cette transition pourrait être un repliement de ces régions en cristallites de feuillets  $\beta$  qui serait accompagnée de l'exposition des tyrosines à la surface de ces cristallites, leur permettant de créer des liaisons hydrogène avec la matrice amorphe environnante. Les cristallites présentes dans les fibres de structure Silk II ne montrent pas l'apparition d'une orientation préférentielle en corrélation avec la durée de conversion.

## IV.1. Experiments

### IV.1.1. Production of silk fibres

As described in section III-1-2 silk threads have been produced in a tube-in-tube chip with a 9 mg/mL Fibroin solution and a pH 2 phosphate aggregation buffer. The flow rates were 0.5 mL/hr for the Fibroin and 5 mL/hr for the buffer, so that the compression of the Fibroin flow by the buffer flow mimics the tapering geometry of *B. mori* spinning duct. The inner diameter of the square capillary is 700  $\mu\text{m}$ . In these conditions, the spinning velocity is 3.1 mm/s, the radius of the protein flow before diffusion is around 125  $\mu\text{m}$  and the diffusion mixing is complete about 8.1 mm after the mixing point. The pH of the collection bath was the same before and after the samples production.

### IV.1.2. Raman Spectroscopy experiments

After their formation, the fibres were kept in the water bath for variable periods, up to 24 h, before air drying at room temperature. As it will be shown below, this allowed further conformational changes to occur. The fibres were then analyzed by Raman spectroscopy and WAXS on ID13. The dried fibres were first examined by Raman: two identical Raman spectra on each sample were obtained with a laser wavelength of 785 nm, 100% intensity and three exposures of 10 sec per spectrum. The spectra were background corrected by subtracting a second order polynomial. For curve fitting, functions of the Renishaw WiRE 2.0 program were used. Data are always averaged from the two spectra obtained from each fibre. The intensity parameter corresponds to the height of the fitting Gaussian function.

### IV.1.3. WAXS experiments

In a second step, WAXS patterns were obtained from the fibres by a linear scan with 1  $\mu\text{m}$  increment at ID13. The wavelength was 0.976  $\text{\AA}$ , the beam size around 1  $\mu\text{m}$  and the exposure time per pattern, 10 sec. The detector was a Frelon camera [2]. The distance between the sample and the detector, calibrated by an  $\text{Al}_2\text{O}_3$  standard, was 75.685 mm. For each scan, the patterns from the fibre were averaged using the FIT2D software [3]. The

---

patterns from air, obtained with the sample not in the beam, were averaged and subtracted from the average fibre pattern. Finally, the corrected patterns were azimuthally regrouped over 360 °.

The effect of drying is not addressed in these experiments. However, the drying process is the same for all the samples. Consequently, these experiments allow to follow the conformational changes occurring during the incubation in the water bath. To ensure that there is no evolution of the drying process which could be responsible for the observed results, the samples were not prepared in increasing or decreasing order of duration of incubation in the bath. The experiment was repeated once and very similar results were obtained.

## IV.2. Results and discussion

Figure 47 enables the comparison of the Raman spectra of a degummed *B. mori* silk fibre (red) and a silk fibre spun with the tube-in-tube cell and immediately dried (green).

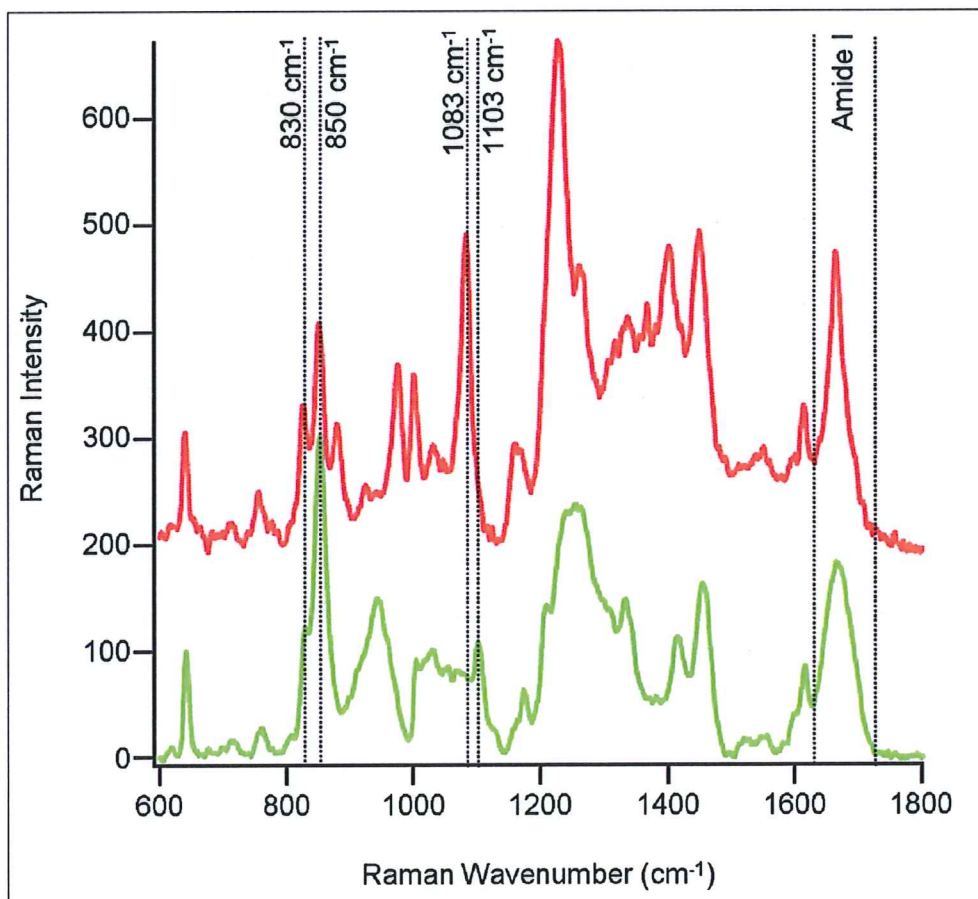


*Fig. 47: Raman spectra of natural degummed silk (red) and an artificially spun Fibroin fiber immediately dried (green).*

The differences between these two spectra suggest that the Fibroin does not have the same conformation in the two fibres. Among these differences the changes occurring in the 840 cm<sup>-1</sup> region, the 1100 cm<sup>-1</sup> region and in the shape of the Amide I band are of particular interest. The changes occurring in the 840 cm<sup>-1</sup> region reflect differences in the tyrosines environment. They should be carefully interpreted as each individual tyrosine might have a specific environment and the Raman spectrum shows an average of all these contributions [4]. However, a global information can be derived from the ratio of the 850 cm<sup>-1</sup> band intensity over the 830 cm<sup>-1</sup> band intensity. A low  $I_{850}/I_{830}$  ratio, around 0.3, reflects that the tyrosines



are mostly buried in the protein and that the hydroxyl group of their side chain (in pink, figure 48) acts as a strong hydrogen-bond donor to an electronegative acceptor [5]. This is the situation observed in the degummed silk Raman spectrum (red) figure 47. A very high  $I_{850}/I_{830}$  ratio, as in the regenerated silk fibre spectrum (in green on figure 47) suggests that the tyrosines are mostly in a very hydrophobic environment [5].

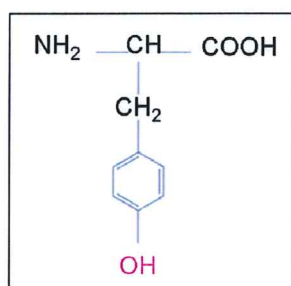


*Fig. 48: Tyrosine residue with the side chain hydroxyl group in pink.*

In the  $1100\text{ cm}^{-1}$  region, a band at  $1103\text{ cm}^{-1}$  is present in the regenerated fibre spectrum and absent in the natural silk fibre spectrum. On the contrary a band at  $1083\text{ cm}^{-1}$  is present in the natural silk fibre spectrum and absent in the regenerated fibre spectrum. This change has been attributed to a Silk I  $\rightarrow$  Silk II conformational transition [6, 7]. Therefore, the artificially spun fiber exhibits a Silk I structure when it is dried immediately after spinning.

The amide I band can be used to determine protein secondary structure [8-10]. Concerning silk more specifically, this band can be deconvoluted as shown figure 49 to quantify each secondary structure component of the fibre [1].

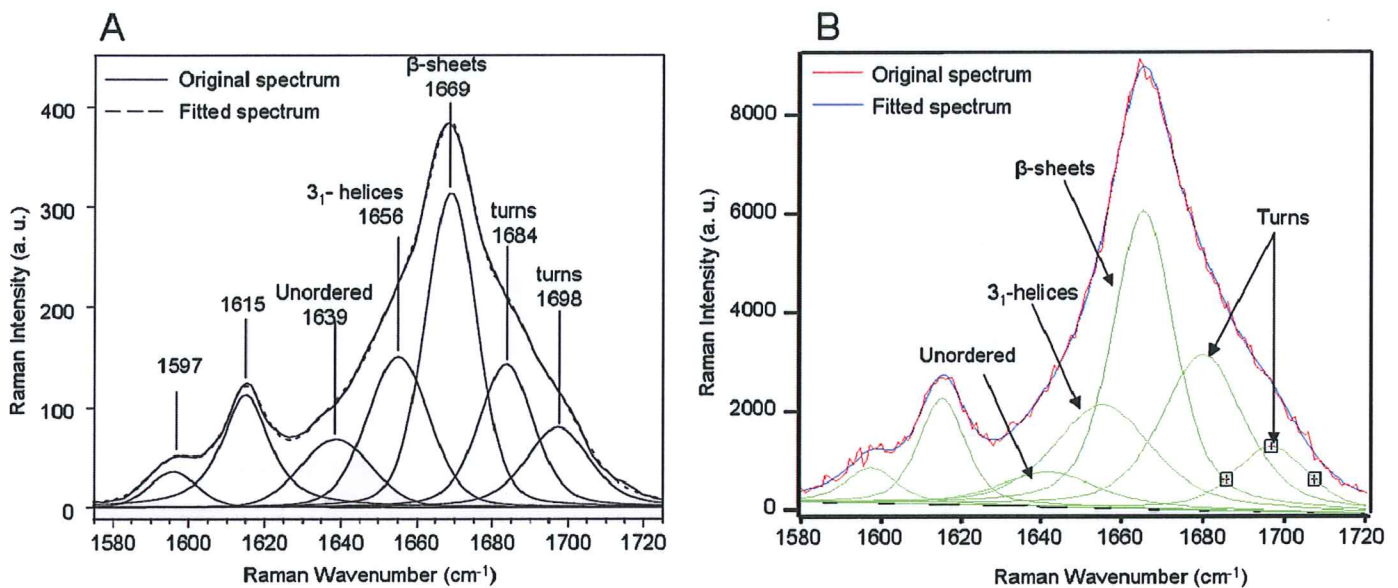


Fig. 49: Secondary structure quantification from the Amide I Raman band [1]. A: Fit done by Lefevre et al., B: Example of fit done in the present study (on a spectrum from a fibre incubated 24 h).

By carrying out the same data treatment as Lefevre *et al.*, the proportion of each type of secondary structure can be calculated from the Raman spectrum shown in figure 47. The results, averaged from two spectra taken from each sample, are summarized in table 3. The errors are the standard deviation between the data from the two spectra. From this quantification, it appears that the proportion of turn structures is about the same in Silk I and Silk II structures. However, the proportion of  $3_1$ -helix (see appendix I) and unordered structures is higher and the  $\beta$ -sheet proportion is lower in the regenerated fibre than in the natural one. This data treatment implicitly assumes that the secondary structures represented in the artificially spun fibre are the same as in the degummed silk.

Secondary structure	unordered	$3_1$ -helix	$\beta$ -sheet	turn
Degummed Silk	7 (+/- 0.3)	19 (+/- 0.5)	46 (+/- 0.2)	28 (+/- 0.1)
Artificially Spun Silk	12 (+/- 4.3)	25 (+/- 1.9)	32 (+/- 1.2)	31 (+/- 1.2)

Table. 3: Secondary structure quantification from the spectra shown figure 47.

Artificially spun fibres have been left in the water bath for different times from 0 to 24 hr. Then, they have been air-dried at room temperature. Their Raman spectra are compared in figure 50.

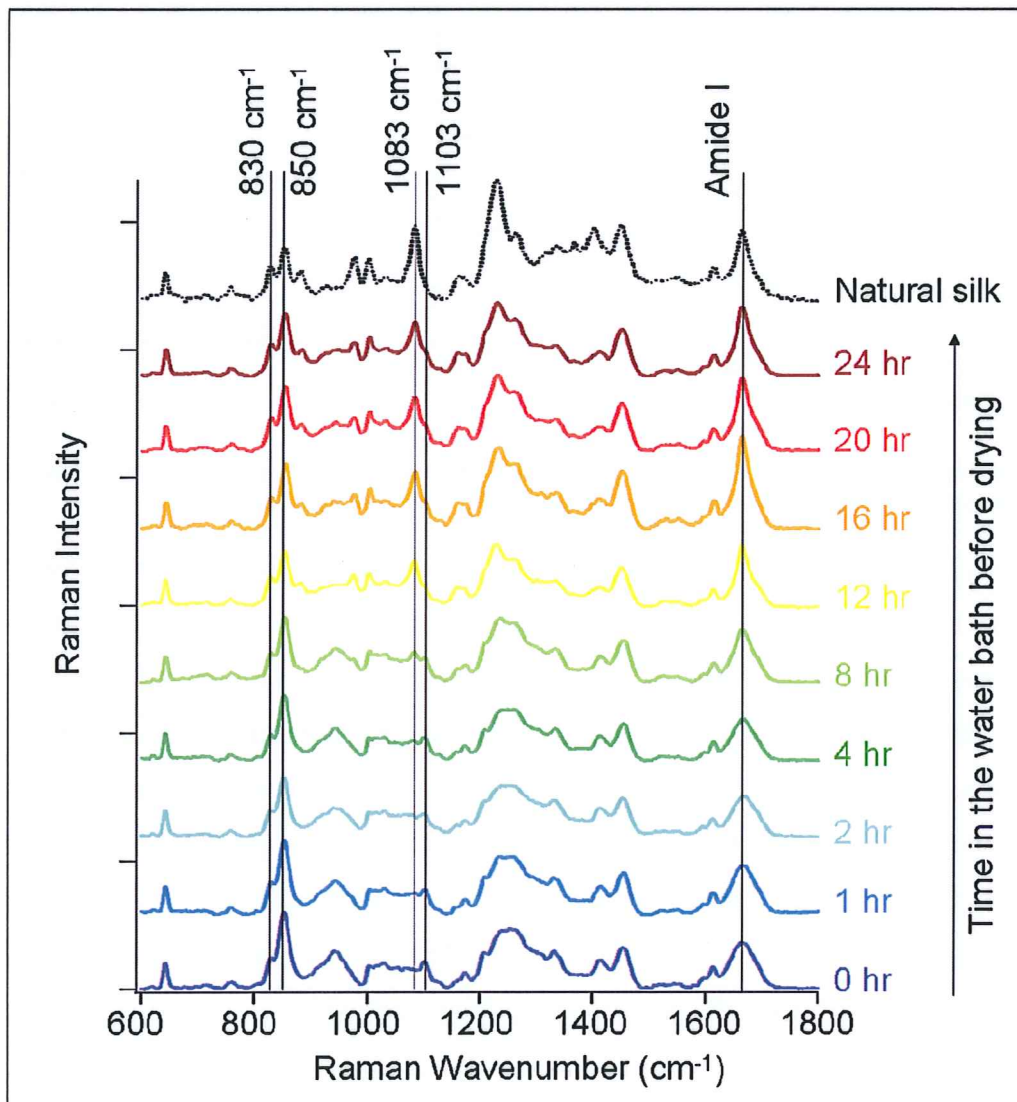


*Fig. 50: Raman spectra of artificially spun Fibroin fiber left in the water bath for various time before drying.*

In the three regions of interest described above, the Raman spectrum of artificially spun fiber evolves to resemble the one of the natural degummed silk (also shown figure 50 for comparison). The ratio  $I_{850}/I_{830}$  decreases, the  $1103\text{ cm}^{-1}$  band appears while the  $1083\text{ cm}^{-1}$  band disappears and the Amide I band thins. These features can be used to evaluate the kinetic of this Silk I  $\rightarrow$  Silk II conversion (figure 51).

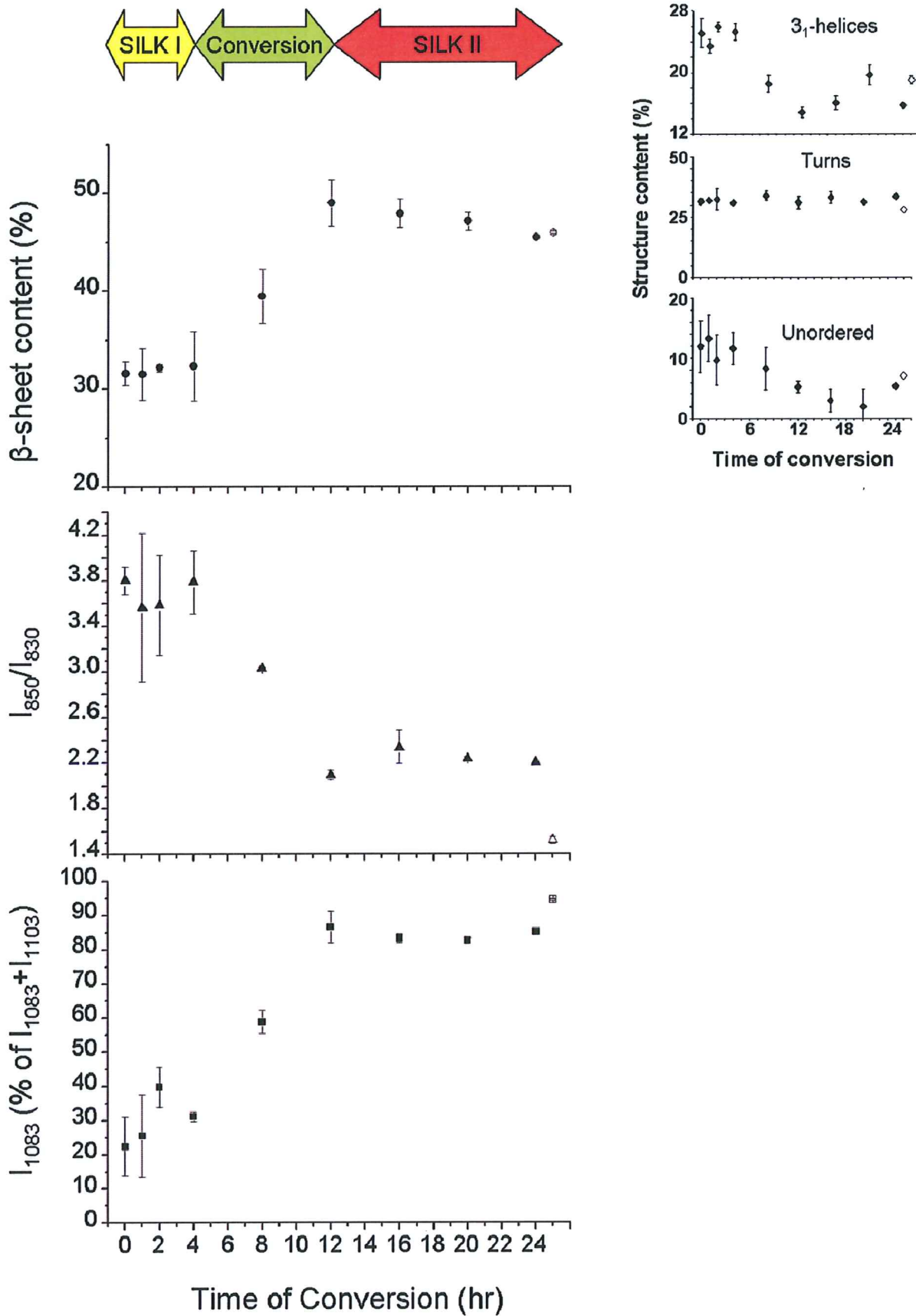


Fig. 51: Kinetics of the Raman spectra evolution. Squares: relative intensity of the  $1083\text{cm}^{-1}$  band; triangles:  $I_{850}/I_{830}$  ratio; circles: proportion of  $\beta$ -sheet structure; black: artificially spun fibres; white: degummed natural silk. The insert also shows the proportion evolution of the other secondary structures represented.



The conversion takes place between 4 hr and 12 hr after the fibre has been spun. During this time range, the intensity of the  $1083\text{cm}^{-1}$  band increases from about 20% to about 90% of the sum of  $1103\text{ cm}^{-1}$  and  $1083\text{ cm}^{-1}$  band intensities (black squares), reflecting the conformational transition from Silk I to Silk II.

Concomitantly, the  $I_{850}/I_{830}$  ratio (black triangles) decreases from 3.8 to 2.2 which reflects that the tyrosines go from a very hydrophobic environment to a more hydrophilic environment where they are involved in strong hydrogen bonds. These results are in agreement with the results of Taddei *et al.* [11]. Asakura *et al.* [12] suggest from the study of model peptide that the tyrosine could facilitate the Silk I  $\rightarrow$  Silk II conversion.

The  $\beta$ -sheet content, calculated by the Lefevre *et al.* method, increases from 30 % to 50 % of the secondary structures. It has to be noted that the proportion of turns seems to remain constant and the increase of  $\beta$ -sheet content is balanced by a decrease of the  $3_1$ -helices and unordered structure proportions. These results suggest that the sequence parts involved in the Silk I  $\beta$ -turn and in the Silk II  $\beta$ -sheet are not the same. This hypotheses would be in disagreement with Asakura's studies [13] and in agreement with Wilson's studies [14], both being based on model peptides analysis. It should be investigated in more detail.

A large part of the Fibroin tyrosines are located inside the GA-rich blocs of FibH (chapter I, figure 6). One can imagine that these changes could reflect a folding of these GA-rich regions in pleated  $\beta$ -sheet, exposing the tyrosines to the less hydrophobic environment of the amorphous matrix with which they could link strong hydrogen bonds.

To strengthen this hypothesis, the crystallites formation during this conversion was studied by WAXS analysis of the same samples (see "Experiments" section of this chapter). Figure 52 presents the isotropic WAXS patterns and the azimuthally regrouped profiles of these artificially spun fibres. For comparison, a pattern from natural silk has also been azimuthally regrouped over  $360^\circ$  although it is anisotropic because of the crystallites orientation along the fibre axis.

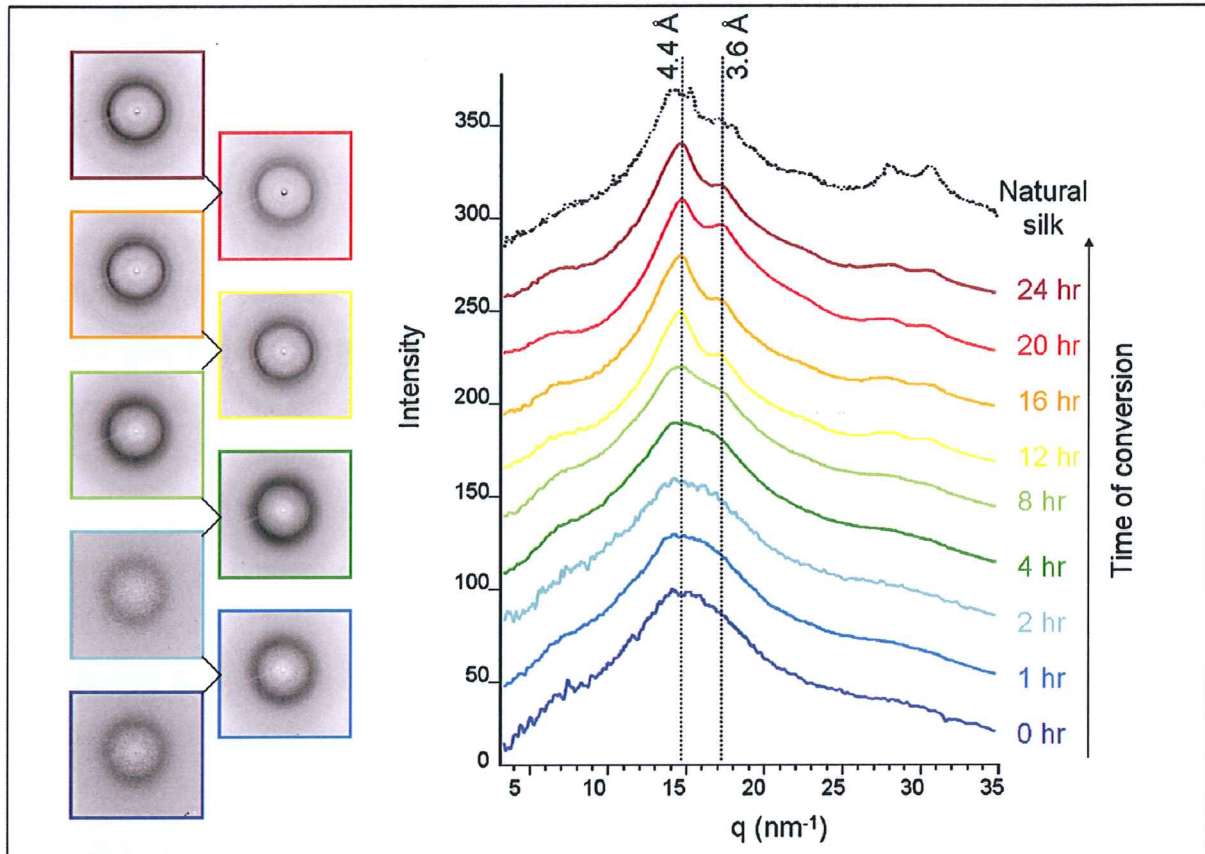


**Fig. 52:** WAXS patterns of Fibroin fibres left to convert for various durations (left) and the corresponding profiles obtained by azimuthal regrouping.

Similarly to the Raman spectra, the WAXS intensity profiles evolve towards the profile of *B. mori* silk. If the fibre is left for less than 4 hours in the water bath before drying, the patterns show a diffuse halo for the sample (Figure 52). For longer conversion times, the halo separates into two thinner rings, revealing small crystalline domains. The peak profiles can be fitted by two Lorentzian functions, representing the crystalline fraction, over a background fitted by a broad Gaussian function, representing the short range order fraction, and a first order polynomial, in agreement with the structural model previously proposed [15]. The crystal characteristic distances corresponding to these peaks are 4.4 Å ( $q = 14.3 \text{ nm}^{-1}$ ; superposition of 210 and 020 reflections) and 3.6 Å ( $q = 17.45 \text{ nm}^{-1}$ ; 030 reflection). This is in agreement with a pleated  $\beta$ -sheet structure proposed for natural silk [15-17].

This Silk I structure should be compared with the available literature data, which is made more complicated by the peak width. The silk I WAXS pattern proposed by He *et al.* [18] shows its maximum scattering peak at  $d = 4.5 \text{ Å}$  and another at  $d = 7.5 \text{ Å}$ . The pattern presented above also shows its maximum intensity at  $d = 4.5 \text{ Å}$  but no peak is detectable at  $d = 7.5 \text{ Å}$ . Therefore, these two structures could be different. The Silk I WAXS pattern

presented by Sohn *et al.* [19] also reveals a very amorphous structure by its broad peak but no d-spacing information is given. This comparison underlines the fact that WAXS is not the best technique to characterize amorphous structures and that the use of other complementary techniques, such as Raman spectroscopy, is essential.

Concerning the orientation of the crystallites, some of the patterns were textured but this was correlated with the time of conversion. Although it has been done very carefully, a weak extension of some samples during their transfer from the bath to the drying support might be the cause of this orientation. The effect of such extension could be rigorously studied as a model for shear forces occurring in the *B. mori* spinning duct.

In summary, these results suggest that the artificial spinning method described above enables the production of a fibre whose structure appears to be a hydrated precursor of Silk I. If the fibre is left in water, this structure converts to a hydrated precursor of Silk II. No structural intermediate has been observed, but rather a co-existence of the two conformations (fiber dried 8 h after spinning). The main feature of this conformational transition could be the folding of the GA-rich blocks of FibH in  $\beta$ -sheet crystallites. The tyrosines would be concomitantly exposed to an environment less hydrophobic, maybe the amorphous matrix, and involved in strong hydrogen-bonds.



## Bibliography

1. Lefevre, T., M.E. Rousseau, and M. Pezolet, *Protein secondary structure and orientation in silk as revealed by Raman spectromicroscopy*. Biophysical Journal, 2007. **92**(8): p. 2885-2895.
2. Labiche, J.C., et al., *Invited article: The fast readout low noise camera as a versatile x-ray detector for time resolved dispersive extended x-ray absorption fine structure and diffraction studies of dynamic problems in materials science, chemistry, and catalysis*. Review of Scientific Instruments, 2007. **78**(9).
3. Hammersley, A., *The FIT2D home page*. [www.esrf.eu/computing/scientific/FIT2D/](http://www.esrf.eu/computing/scientific/FIT2D/), accessed July 10, 2007.
4. Siamwiza, M.N., et al., *Interpretation of Doublet at 850 and 830  $\text{Cm}^{-1}$  in Raman-Spectra of Tyrosyl Residues in Proteins and Certain Model Compounds*. Biochemistry, 1975. **14**(22): p. 4870-4876.
5. Monti, P., et al., *Structure modifications induced in silk fibroin by enzymatic treatments. A Raman study*. Journal of Molecular Structure, 2005. **744**: p. 685-690.
6. Monti, P., et al., *Raman spectroscopic studies of silk fibroin from Bombyx mori*. Journal of Raman Spectroscopy, 1998. **29**(4): p. 297-304.
7. Rousseau, M.E., et al., *Study of protein conformation and orientation in silkworm and spider silk fibers using Raman microspectroscopy*. Biomacromolecules, 2004. **5**(6): p. 2247-2257.
8. Berjot, M., J. Marx, and A.J.P. Alix, *Determination of the Secondary Structure of Proteins from the Raman Amide-I Band - the Reference Intensity Profiles Method*. Journal of Raman Spectroscopy, 1987. **18**(4): p. 289-300.
9. Bussian, B.M. and C. Sander, *How to Determine Protein Secondary Structure in Solution by Raman-Spectroscopy - Practical Guide and Test Case Dnase-I*. Biochemistry, 1989. **28**(10): p. 4271-4277.
10. Huang, C.Y., G. Balakrishnan, and T.G. Spiro, *Protein secondary structure from deep-UV resonance Raman spectroscopy*. Journal of Raman Spectroscopy, 2006. **37**(1-3): p. 277-282.
11. Taddei, P., et al., *Raman study of poly(alanine-glycine)-based peptides containing tyrosine, valine, and serine as model for the semicrystalline domains of Bombyx mori silk fibroin*. Biopolymers, 2004. **75**(4): p. 314-324.
12. Asakura, T., et al., *Structural role of tyrosine in Bombyx mori silk fibroin, studied by solid-state NMR and molecular mechanics on a model peptide prepared as silk I and II*. Magnetic Resonance in Chemistry, 2004. **42**(2): p. 258-266.
13. Asakura, T., et al., *A repeated beta-turn structure in poly(Ala-Gly) as a model for silk I of Bombyx mori silk fibroin studied with two-dimensional spin-diffusion NMR under off magic angle spinning and rotational echo double resonance*. Journal of Molecular Biology, 2001. **306**(2): p. 291-305.
14. Wilson, D., R. Valluzzi, and D. Kaplan, *Conformational transitions in model silk peptides*. Biophysical Journal, 2000. **78**(5): p. 2690-2701.



- 
15. Martel, A., et al., *Thermal Behavior of Bombyx mori silk: Evolution of crystalline parameters, molecular structure, and mechanical properties*. *Biomacromolecules*, 2007. **8**(11): p. 3548-3556.
  16. Marsh, R.E., R.B. Corey, and L. Pauling, *An Investigation of the Structure of Silk Fibroin*. *Biochimica Et Biophysica Acta*, 1955. **16**(1): p. 1-34.
  17. Takahashi, Y., M. Gehoh, and K. Yuzuriha, *Structure refinement and diffuse streak scattering of silk (Bombyx mori)*. *International Journal of Biological Macromolecules*, 1999. **24**(2-3): p. 127-138.
  18. He, S.J., R. Valluzzi, and S.P. Gido, *Silk I structure in Bombyx mori silk foams*. *International Journal of Biological Macromolecules*, 1999. **24**(2-3): p. 187-195.
  19. Sohn, S., H.H. Strey, and S.P. Gido, *Phase behavior and hydration of silk fibroin*. *Biomacromolecules*, 2004. **5**(3): p. 751-757.

## **CHAPTER V- ARTIFICIAL SPINNING OF SILK: Model and Discussion**

**Résumé de ce chapitre :**

Ce chapitre synthétise les données présentées dans les deux précédents. Il présente un modèle de formation de la soie selon lequel les fibroïnes s'agrègent puis les agrégats se compactent. A lieu ensuite la conversion de la forme Silk I à la forme Silk II au cours de laquelle des structures désordonnées subissent une transition conformationnelle vers des structures en feuillets  $\beta$  empilés (cristallites). Cette transition se caractérise également par le changement d'environnement des tyrosines. Celles-ci passent d'un environnement très hydrophobe à un environnement plus hydrophile où elles sont impliquées dans de fortes liaisons hydrogène.

Ce modèle est confronté à ceux présentés dans la littérature. Il est proche de celui proposé par Jin et Kaplan [1] (figure 13). Il précise la séquence temporelle entre l'agrégation et la conversion Silk I  $\rightarrow$  Silk II. Le modèle de transition conformationnelle de structures désordonnées vers des feuillets  $\beta$  se distingue de celui proposé par Asakura *et al.* [2, 3] selon lequel la conversion Silk I  $\rightarrow$  Silk II impliquerait une transition de coudes  $\beta$  en feuillets  $\beta$ . Il est cependant en accord avec le modèle proposé par Wilson *et al.* [4].

Enfin, des perspectives de travail sont proposées afin de préciser ce modèle. L'effet du séchage et des forces de cisaillement devrait être étudié plus avant. La possibilité d'une autre séquence temporelle dans laquelle les forces de cisaillement induiraient un repliement en cristaux liquides [5] de feuillets  $\beta$  préalable à l'agrégation doit également être envisagée et testée. Un équipement microfluidique plus complexe permettant de mieux mimer les conditions *in vivo* pourrait apporter un progrès considérable dans la compréhension du processus naturel de formation de la soie.

## V.I. Proposed model

The experiments presented in the two previous chapters allow the elaboration of a model for silk formation (figure 53). In this model, the Fibroin molecules are assumed to first aggregate in clusters of defined size. In this cluster, the Fibroin would have a smaller size ( $R_g = 8$  nm) than in diluted solution ( $R_g = 10.8$  nm). Subsequently, the aggregates would compact slightly. The Fibroin could then convert from a Silk I conformation to a Silk II conformation. This conversion can occur without further chemical reaction, probably driven by hydrophobic forces as proposed by Jin and Kaplan [1] (figure 13, chapter I). It would imply the folding of GA-rich regions into the hydrated precursor of pleated  $\beta$ -sheet crystallites. During this conversion, the tyrosines would change environment, from a very hydrophobic environment to a less hydrophobic environment where they are involved in strong hydrogen bonds.

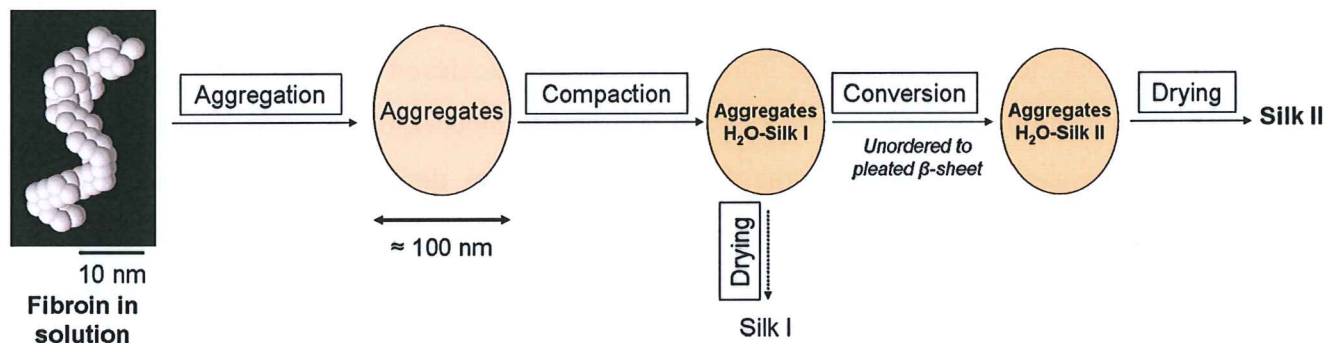


Fig. 53: Currently proposed model of silk formation.

## V.II. Comparison with other models

The model presented above is quite close to the one developed by Jin and Kaplan [1] (Figure 13) in which Fibroin aggregates into micelles which have a predicted size close to the clusters observed here. Our model implies that the aggregation can occur before the  $\beta$ -sheet folding, and that the silk I to silk II conversion does not require additional chemical reaction or shear forces. However the metallic ions, dehydration and shear forces existing in the *B. mori* spinning apparatus could accelerate this process.



The model discussed here and the model by Jin and Kaplan [1] differ from the model proposed by Li *et al.* [6], which assumes that a direct folding of Fibroin into  $\beta$ -sheet takes place within the nucleation-dependent process of aggregation. The Silk I to Silk II conversion has been proposed to consist of a conformational transition from  $\beta$ -turn to  $\beta$ -sheet structure on the basis of model peptides analysis by Asakura *et al.* [2, 3]. The current Raman analysis using a method proposed by Lefevre *et al.* [7] shows that the turn structure proportion remains constant although the  $\beta$ -sheet proportion increases while the  $3_1$ -helices and unordered structure proportions decrease. This could rather suggest that the conversion consists of a transition from an unordered structure to a  $\beta$ -sheet structure, as proposed by Wilson *et al.* [4]. The  $\beta$ -turn structure could be a rapid intermediate in this transition. These scenarios should be compared using molecular dynamics simulations as carried out by Yamane *et al.* [3].

### V.III. Perspectives to refine this model

It has to be noted that no orientation could be achieved in a repeatable way by this artificial spinning method. The orientation is probably induced by the shearing forces which are not properly controlled in the current experimental development. Consequently, the precise time sequence between the structural conversion and orientation remains to be clarified. In the experiments currently described, the shear forces are mimicked in the chip by applying a high flow rate ratio between the aggregation buffer and the protein solution. They take place at the beginning of the aggregation process which might be too early in the process of silk formation. Effectively, the  $\beta$ -sheet crystallites which should orient along the fibre axis are formed later, during the conversion Silk I  $\rightarrow$  Silk II. It would be interesting to test systematically the effect of shearing at different times after aggregation to investigate if the conversion should take place before any orientation process could occur, or if the shearing would accelerate the Silk I  $\rightarrow$  Silk II conversion.

The drying process of silk should be further investigated. Preliminary experiments reveal the existence of an intermediate phase presenting a large scale organization. Interestingly, a large scale organization is also detected in the low  $q$ -range of the X-ray scattering spectra of silk dried 20 hours after formation. A precise characterization of the secondary structures present in the hydrated precursor of Silk I and Silk II could enable a better determination of the molecular folding involved in the conformational transition.

---

The experiments currently presented show one possible pathway to transform a Fibroin liquid dope into a solid silk II fiber. It is important to test if other silk II formation paths are possible. Some preliminary experiments show that the shearing of the Fibroin dope in a tapered capillary induces change in the macroscopic aspect of the dope: the solution becomes less viscous. It could be a sign of a conformational change of the Fibroin. It has been proposed that the conformational conversion from an amorphous folding to a mainly  $\beta$ -sheet phase could take place before or at the same time as the aggregation step [6].

In view of the complexity of the spinning apparatus of *B. mori* and spiders, it is evident that the experimental conditions in the current microfluidic device are largely simplified compared to the natural ones. Only the pH drop is mimicked (and exaggerated), while the change in ionic composition and the shear forces are ignored. However, the concentric geometry is already closer to the spinning duct shape than the planar T-shape mixer tested before. A more complicated set up, allowing successive ions additions to the dope and rolls mimicking shear forces, would be a further step toward the natural conditions.

---

## Bibliography

1. Jin, H.J. and D.L. Kaplan, *Mechanism of silk processing in insects and spiders*. Nature, 2003. **424**(6952): p. 1057-1061.
2. Asakura, T., et al., *A repeated beta-turn structure in poly(Ala-Gly) as a model for silk I of Bombyx mori silk fibroin studied with two-dimensional spin-diffusion NMR under off magic angle spinning and rotational echo double resonance*. Journal of Molecular Biology, 2001. **306**(2): p. 291-305.
3. Yamane, T., et al., *Molecular dynamics simulation of conformational change of poly(Ala-Gly) from silk I to silk II in relation to fiber formation mechanism of Bombyx mori silk fibroin*. Macromolecules, 2003. **36**(18): p. 6766-6772.
4. Wilson, D., R. Valluzzi, and D. Kaplan, *Conformational transitions in model silk peptides*. Biophysical Journal, 2000. **78**(5): p. 2690-2701.
5. Vollrath, F. and D.P. Knight, *Liquid crystalline spinning of spider silk*. Nature, 2001. **410**(6828): p. 541-548.
6. Li, G.Y., et al., *The natural silk spinning process - A nucleation-dependent aggregation mechanism?* European Journal of Biochemistry, 2001. **268**(24): p. 6600-6606.
7. Lefevre, T., M.E. Rousseau, and M. Pezolet, *Protein secondary structure and orientation in silk as revealed by Raman spectromicroscopy*. Biophysical Journal, 2007. **92**(8): p. 2885-2895.

## **Chapter VI- PHYSICAL PROPERTIES OF SILK: The Effects of Temperature**



**Résumé de ce chapitre:**

Les expériences décrites dans ce chapitre ont fait l'objet d'une publication [1]. Il s'agit de l'investigation de l'effet de la température sur la soie naturelle d'un point de vue moléculaire, structural et mécanique. Deux stratégies expérimentales ont été utilisées : l'augmentation *in situ* de la température pendant l'analyse par WAXS et l'analyse à température ambiante, par WAXS, électrophorèse en conditions dénaturantes et tests mécaniques de fibres préalablement chauffées.

L'augmentation *in situ* de la température pendant l'analyse par WAXS révèle une dilatation des cristallites le long des liaisons hydrogène liant les brins  $\beta$  en feuillets et dans la direction d'empilement des feuillets.

La seconde stratégie met en évidence l'étonnante stabilité de la structure cristalline alors même que les chaînes peptidiques sont dégradées et que la fraction amorphe subit une transition vitreuse accompagnée par une altération des propriétés mécaniques de la fibre.

## VI.1. Introduction

This chapter describes experiments which were carried out to investigate the effects of temperature on silk. The behaviour of different aspects of this material has been followed in function of temperature ranging from 100 K to 570 K: the structure, the molecular integrity and the mechanical properties. The results have been published in a more complete article [1]. A few supplementary technical details are provided below.

Two different experimental strategies have been used to determine the effect of temperature on natural *B. mori* silk.

The first one is an *in situ* analysis: the temperature of the silk is changed during its observation by WAXS, thanks to a cryosystem which delivers a flow of dry nitrogen.

The second strategy consists in analyzing, at room temperature, silk fibres which have been previously heat-treated in an oven. It provides information only on the irreversible effects of temperature, whereas the first one investigates both reversible and irreversible effects without distinguishing between them. The second strategy allows the measurement of the temperature effect on the structure of the silk (WAXS), but also on its mechanical properties and on the Fibroin integrity (SDS-PAGE). The temperature ranges accessible by these two methods are different.

A thermal degradation study has recently been performed for dragline silk showing a surprisingly high structural stability of  $\beta$ -sheet domains [2]. However, this previous X-ray study is limited to the analysis of the crystalline fraction of the semicrystalline structure of silk fibres. Termonia's molecular model explaining the mechanical behaviour of dragline silk fibres assumes that the peptide chains in the vicinity of crystallites are constrained by their link to the rigid pleated  $\beta$ -sheet structure [3]. Therefore, this model suggests the existence of a supplementary fraction in addition to the amorphous matrix and the crystalline fraction. This concept has also been introduced in a structural study of dragline silk [4, 5] and called the "short range order" fraction. In addition to the diffraction analysis, the current analysis develops methods to separate the short-range order diffraction scattering from the Bragg reflections.

## VI.2. Experiments

### VI.2.1. Samples

Fresh *Bombyx mori* cocoons were provided by INRA, Unité Séricicole, Lyon, France and were used as received. SR microdiffraction experiments were performed on single baves (composed of two brins with sericin coating). Such experiments on single fibre require a high brilliance synchrotron radiation source [4, 6] while experiments with laboratory X-ray sources are limited to fibre bundles [7, 8]. The baves were separated from the cocoons with microscissors. Care was taken to not introduce mechanical strain. *Greige* silk fibres were provided by Le Musée de la Soie, St Hippolyte du Fort, France. To obtain Greige silk cocoons are boiled in a soap bath in order to soften the sericin layer. Then, baves from up to six cocoons are unwrapped simultaneously and joined in one thread. Figure 54 shows SEM pictures of these samples and their sample-holders used for the *in situ* heating experiment.

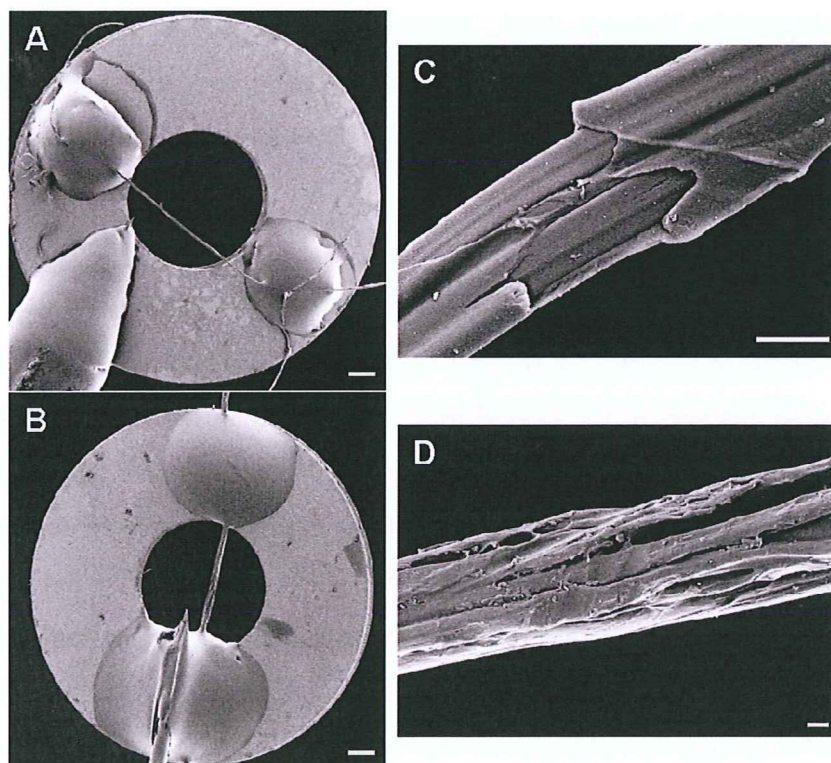


**Fig. 54:** SEM images of samples holders used in the *in situ* heating experiments (A and B, scale bar: 200  $\mu\text{m}$ ) and zoom on the fibres (C and D, scale bar: 10  $\mu\text{m}$ ). A and C: natural bave. B and D: Greige silk thread.



## VI.2.2. Heating conditions

Two kinds of heat treatment were applied, which allow both reversible and irreversible temperature effects to be observed.

For *in situ* synchrotron radiation diffraction experiments under anaerobic conditions, the bave temperature was controlled in the range of 100 K to 500 K by cryostream blowing a 5 litres/min nitrogen flow (technical information: Oxford cryoflow system, [9]). The sample was about 10 mm from the nozzle of the cryosystem. At such a distance, the temperature is less than 1 K different from the set temperature.

Other baves from a cocoon were oven-heated before their characterization at room temperature by denaturing gel electrophoresis (SDS-PAGE), synchrotron radiation diffraction (WAXS) and mechanical tests. Two different ovens were used. The first one makes it possible to heat the sample in non-oxidative conditions by performing the heating in N<sub>2</sub> atmosphere. However, it is limited in temperature to 473 K. To reach higher temperatures, up to 573 K, another oven has to be used which did not allow the control of the sample atmosphere. Therefore, the baves were heated for 6 hours either under a nitrogen atmosphere ( $298 < T \text{ (K)} < 473$ ) or in air ( $473 < T \text{ (K)} < 573$ ) and then cooled to room temperature.

## VI.2.3. Gel electrophoresis

After heating in a nitrogen atmosphere (as described above), 15 mg of cocoons were partially dissolved in 600  $\mu$ L of saturated LiSCN under shaking at 60 °C for 3 minutes and analysed using a classical denaturing gel electrophoresis. This method allows the separation peptide chains according to their length. Sodium dodecyl sulfate (SDS) is a denaturing agent: it maintains the heat-denatured protein in an unfolded conformation. The first part of the gel is very loose and groups the proteins before their separation in the tighter part of the gel. 3  $\mu$ L of dissolved cocoon solution were denatured by boiling 5 min in sample buffer, and loaded on a 12% denaturing acrylamide gel. The migration lasted 90 min at 120 V. After coomassie blue staining, an image of the gel was digitized in order to quantify the relative amount of protein using the FIT2D software [10]. The solutions' composition is given in Appendix V. A background line, close to each signal line and having the same size, was subtracted. The results (Figure 60) are based on 3 similar experiments. The molecular weight



standard is the molecular weight standard, broad range, from Biorad. This method reveals the length of the peptides present in the sample, which means, in this case, an information on the integrity of the peptidic chains of FibH and FibL.

#### VI.2.4. Mechanical tests

Stress/strain curves of single baves were obtained *ex-situ* using a custom-built stretching cell comprising a force sensor and PC-controlled linear translation stage. Each 4 mm long piece of bave was fixed within a cardboard window using cyanoacrylate adhesive. This was then secured to the stretching cell's clamps, between the motorized stage and the force sensor. The baves were deformed in tension at a constant rate of extension (10  $\mu\text{m/s}$ ) with the force and stage position recorded every 0.5 s. The resulting data were then used to calculate fiber stress and strain (see chapter I). For the stress calculation, the cross sectional area including the sericin coating was approximated using a rectangle, an approximation supported by the SEM micrographs shown in the original publication [1]. The rectangle's dimensions were determined microscopically using the AnalySIS5<sup>TM</sup> software package (Soft Imaging System GmbH, Germany), and averaged between three fibers for each temperature. The strain, stress-to-failure and initial modulus from 9 to 15 fibres were averaged for each temperature. The very short gauge length was chosen in view of the fragility of high temperature treated fibres. We note that “end-effects” could be significant [11]. However, we did not find a significant influence of a shorter gauge length on these mechanical parameters.

#### VI.2.5. Synchrotron Radiation Scattering

WAXS experiments on single *B. mori* baves and Greige silk thread were performed at the ESRF-ID13 beamline. For the *in-situ* heating experiments a microgoniometer set-up was used. The monochromatic synchrotron radiation beam (wavelength:  $\lambda = 0.095$  nm) was focused and collimated to 4  $\mu\text{m}$  for the fresh baves and 10  $\mu\text{m}$  for the greige silk by a combination of refractive Be-lenses and apertures. A single *B. mori* bave or a greige silk thread was glued to a thin metal ring (Figure 52), which was attached to a support and aligned in the beam. The temperature of the cryoflow system was ramped in steps of 10 K from 100 K to 500 K. At every temperature plateau, a linear scan across the bave with 5  $\mu\text{m}$  steps was performed. Consecutive linear scans with increasing temperature were performed displaced

by a 13  $\mu\text{m}$  step-increment along the bave in order to avoid possible radiation damage by neighboring scans. The detector was placed about 110 mm away from the sample.

The same data collection method was applied to the preheated baves at room temperature. The sample was composed of 12 baves heated at 12 different temperatures from 298 K to 548 K and glued at both ends on a cardboard frame, which was fixed to the goniometer support. A further bave -heated at 573 K- was too fragile to be fixed in this way and was therefore glued to the end of a tapered capillary. Figure 55 shows photos of the pre-heated samples and summarizes their preparation conditions.

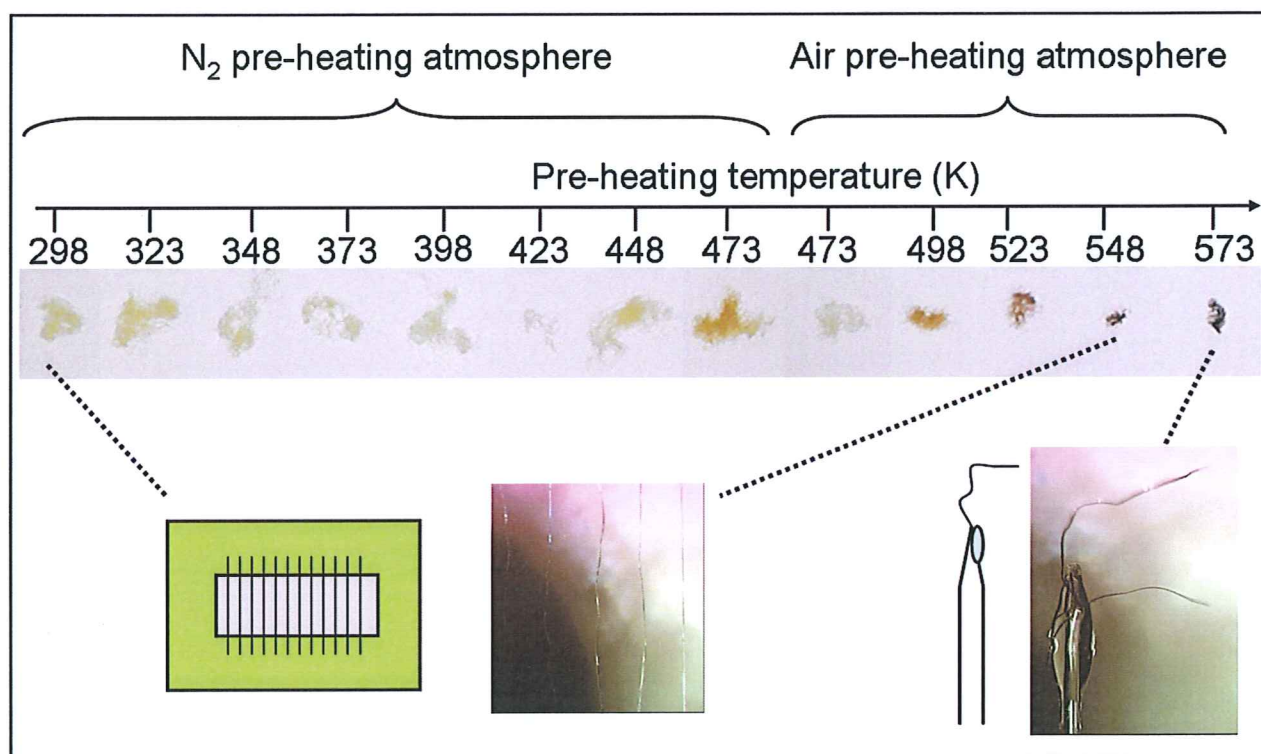


**Fig. 55:** Top: Oven pre-heating conditions. Middle: Photos of the pre-heated samples. Bottom: scheme and photos of the sample holders used in the diffraction experiments.

7 to 8 linear scans of 4  $\mu\text{m}$  step-increment were performed across each bave, spaced by 20  $\mu\text{m}$  to 100  $\mu\text{m}$  along the bave. Diffraction patterns were recorded by a MAR CCD-detector placed about 110 mm away from the sample. The sample-to-detector distance was calibrated by an  $\text{Al}_2\text{O}_3$  powder standard. Care was taken to avoid radiation damage effects by limiting the data collection time to a few seconds per pattern. Initial data reduction and analysis of individual patterns was performed using the FIT2D software package [10]. For recursive data analysis a batch processing software [12, 13] was used. The instrumental

background was corrected by subtracting a pattern recorded just outside a silk fiber during a scan. Sample statistics were improved by averaging several patterns from within the sample and from the background.



## VI.3. Results and discussion

### VI.3.1. *In situ* heating experiment

The 210, 020 and 002 reflections from the WAXS pattern of the *in situ* heated fibres have been fitted using Gaussian functions over a diffuse background made up of a large Gaussian and a first order polynomial in agreement with the structural model presented in the original publication and the Termonia model [1, 3]. In this model, the large Gaussian arises from the hydrogen bonding constraining the peptide chain in the short range order peak. The evolution of the peak positions of the strongest equatorial reflections (210 and 020) during *in situ* heating experiment is shown in Figures 56. The data obtained for the *Greige* silk (Figure 56-A) suggest that the lattice expansion follows two phases: a linear expansion phase up to 200-250 K, and an enhanced linear expansion phase at higher temperatures. In this second phase, the thermal expansions derived from linear least-squares fits are  $1 \cdot 10^{-3}$  nm/K (210 reflection) and  $1.8 \cdot 10^{-3}$  nm/K (020 reflection). This implies a lower thermal expansion along the [210] direction -which is closer to the pleated-sheet [100] direction- than to the chain-stacking [010] direction. In view of the overlap of 020 and 210 reflections, we verified that the thermal expansion derived from the 030 reflection was comparable to the 020 reflection. The position of the *B. mori* 002 reflection is practically constant across the temperature range (data not shown), which suggests that the expansion coefficient peptide bond (along the c-axis) is significantly lower than the expansion coefficient along the [210] and [010] direction. This result suggests a more important expansion of the crystallites along the hydrogen bonds linking the  $\beta$ -strand in  $\beta$ -sheets and along the direction of pleating of those  $\beta$ -sheets than along the fibre direction. Although less smooth due to poorer statistics, the results for fresh silk expansion seem to follow the same scheme (Figure 56-B).



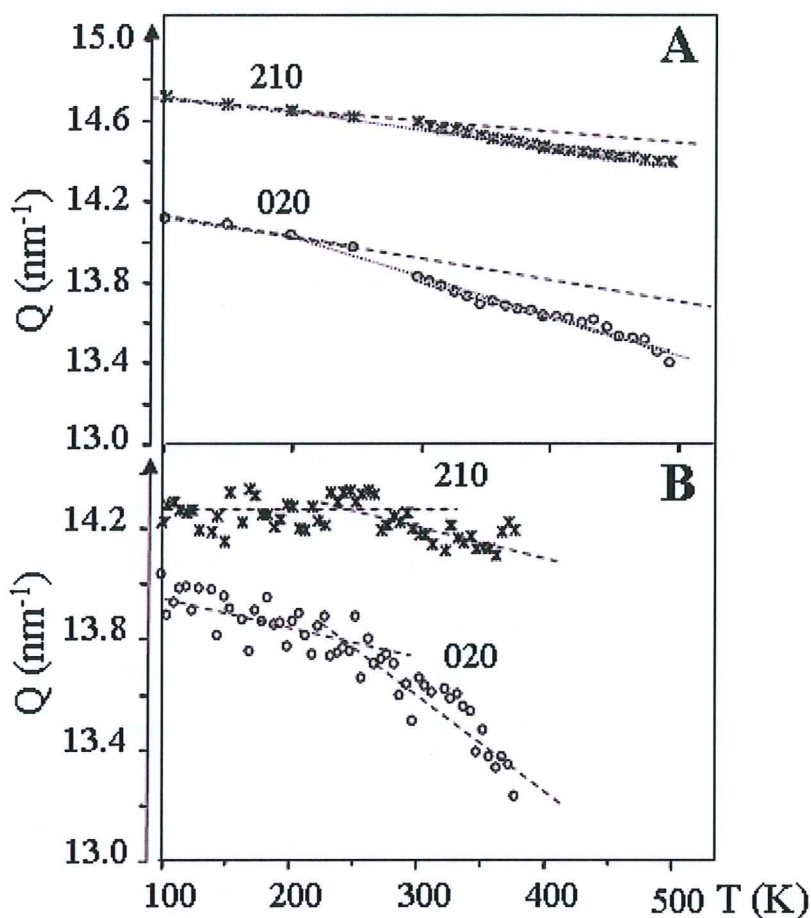


*Fig. 56: Evolution of the 210 and 020 reflections position during in situ heating of greige silk (A) and natural silk (B) single fibres.*

The origin of the onset of the enhanced thermal expansion along the [010] direction is not clear at present but could be due to an increasing side-chain mobility (e.g. onset of CH<sub>3</sub> rotation) modifying the inter-chain distance. An onset of molecular mobility at about 200 K has also been observed for dragline spider silk by inelastic neutron scattering [5] and dynamic mechanical analysis (DMA) [14]. However, the neutron scattering data are mainly due to water mobility in the amorphous fraction while the current diffraction data reflect changes occurring in the crystalline fraction.

## VI.3.2. Pre-heated Fibres Analysis

### VI.3.2.1. Silk structure stability

In the *in situ* heating experiment presented above, the Bragg peak intensity remains strikingly stable despite the temperature increase up to 500 K. The oven pre-heating experimental strategy allows to increase further the temperature up to 573 K to observe possible irreversible effects. The WAXS patterns are decomposed in order to extract information about the crystalline fraction on one hand and the short range order fraction on the other hand. Figure 57 illustrates this treatment. The patterns are azimuthally regrouped in three-dimensional patterns. The Bragg peaks are first masked and the remaining signal is fitted using a Gaussian which represents the short range order fraction signal and a second order polynomial baseline. This simulated background is subtracted from the pattern. The overall intensity of the Bragg peaks is quantified as the remaining intensity after subtraction of the model background from the pattern.

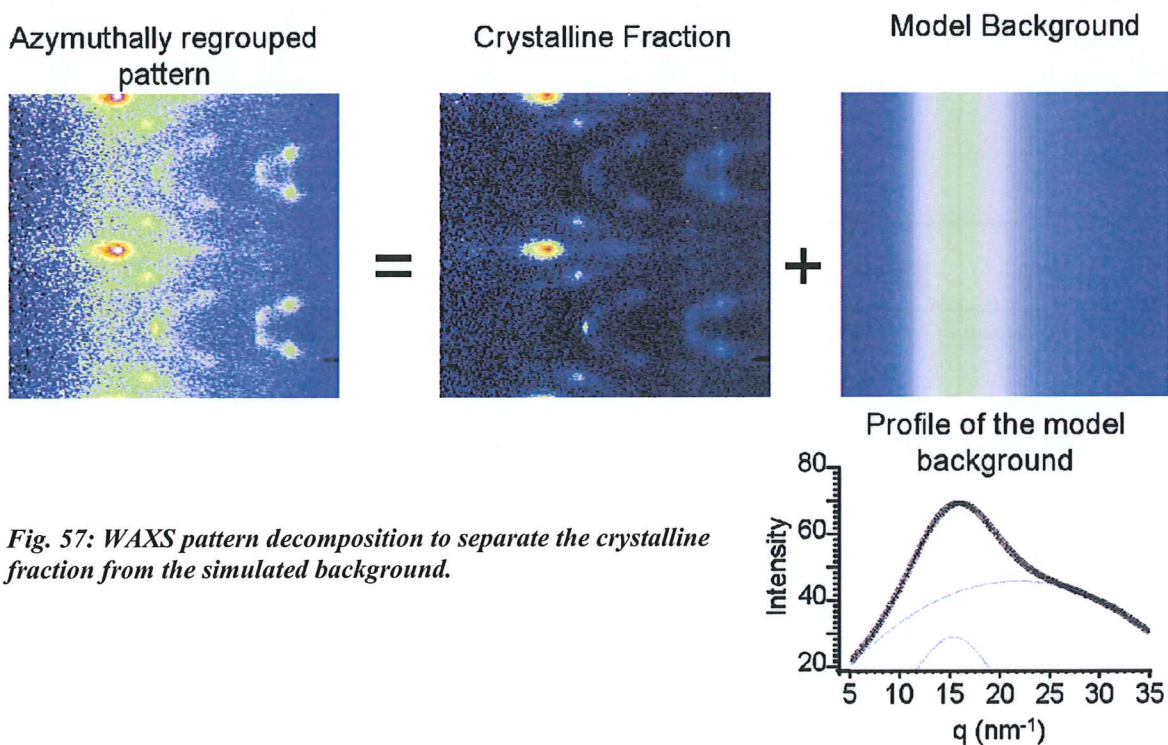


**Fig. 57:** WAXS pattern decomposition to separate the crystalline fraction from the simulated background.

A crystallinity index is calculated as the ratio of the sum of Bragg peak intensities over the total pattern intensity and scaled to 1 at room temperature. The evolution of this crystallinity index as a function of the heat treatment temperature is shown in Figure 58. The values plotted are averages of the values calculated from 7 to 8 patterns for each fiber. The error bars are the standard deviation of these values. The selected diffraction patterns show the overall degradation. An azimuthally integrated intensity profile shown to the right has been determined for the pattern obtained at the highest temperature (573 K) and fitted with 3 Gaussian profiles and a 0-order polynomial background. The d-values (nm) of the fitted peaks are indicated.

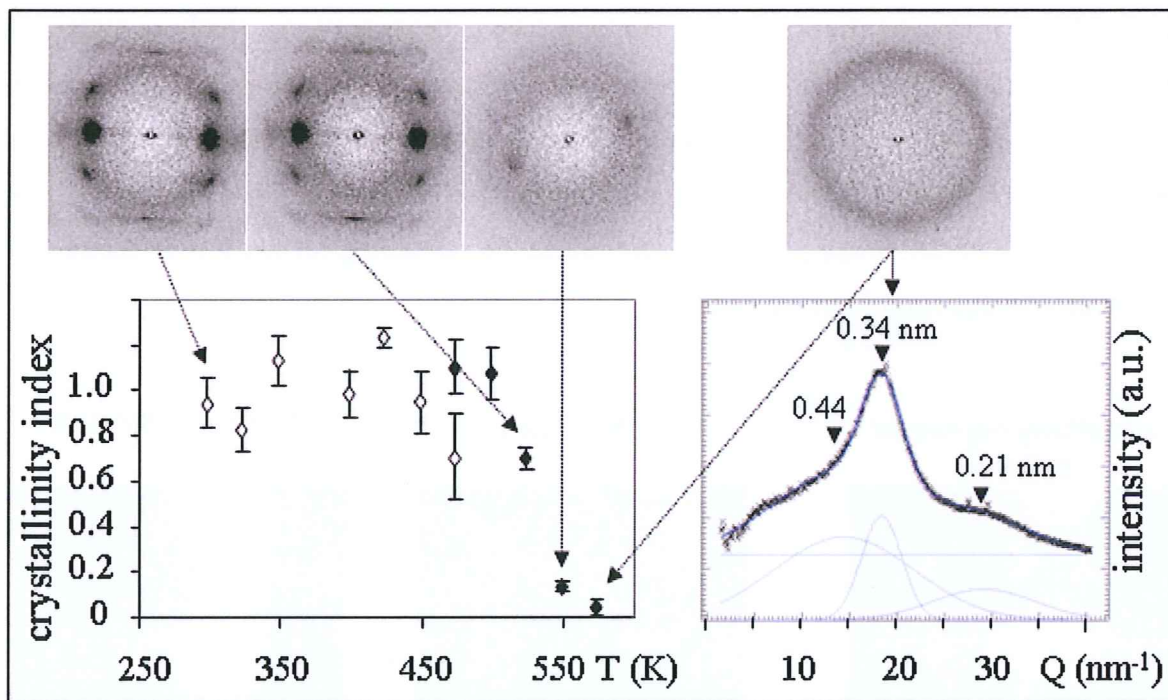
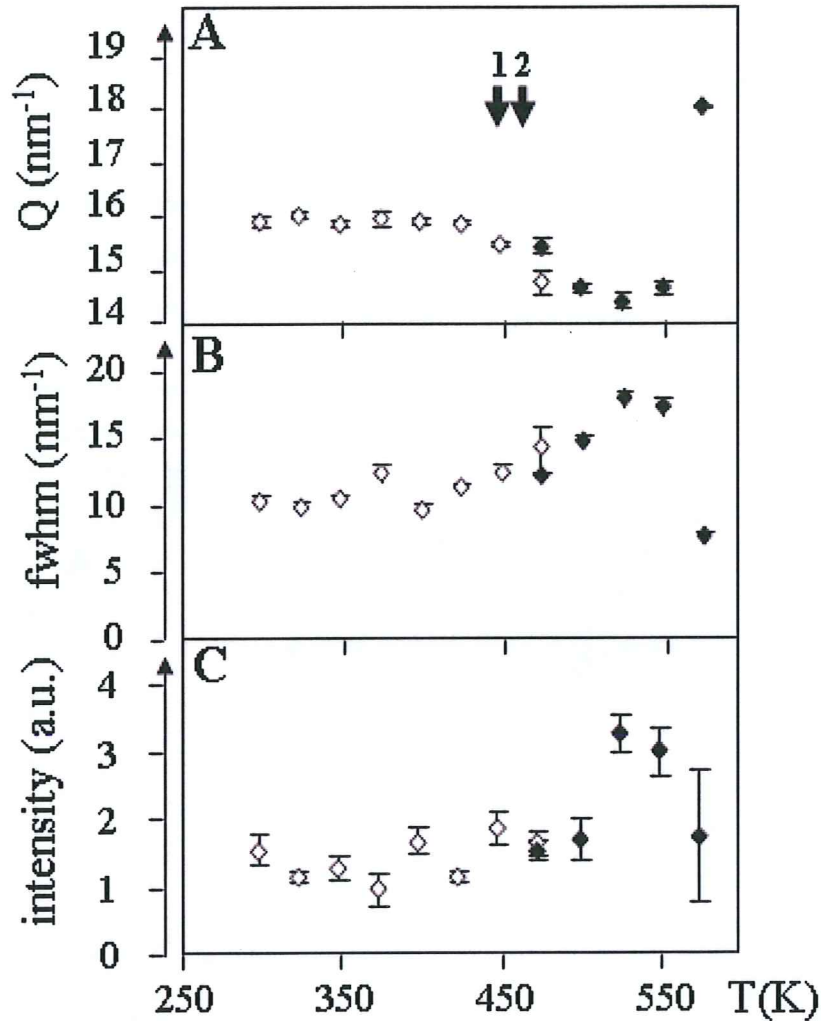


Fig. 58: Evolution of the crystallinity index in function of heat treatment temperature up to 573 K.

The crystallinity index remains constant until 498 K (225 °C). This shows an exceptional temperature stability of the semi-crystalline structure of silk. However, above 498 K, the WAXS pattern changes progressively: the Bragg peaks disappear and it remains only a diffuse ring at 573 K. The d-spacing of this ring is the same as the one of carbonized wood [15] which suggests that between 498 K and 573 K, the structural changes observed correspond to the silk carbonization. In the same temperature range, the silk fibres blacken (Figure 55).



The evolution of the short range order fraction can be followed by the parameters of the fitting Gaussian in the simulated background. Figure 59 shows the evolution of this Gaussian  $q$ -position (A), width (B, full width half maximum) and integrated intensity (C).



*Fig. 59: Evolution of the short range order fraction parameters in function of heat treatment temperature up to 573 K: the  $q$ -position (A), the full width at half maximum (B) and the integrated intensity (C) of the Gaussian fit of data from the in situ heating (white) and oven-preheated (black) experiments.*

Before carbonization, between 423 K and 473 K, the Gaussian parameters change. Its position decreases, its width increases and its intensity increases. This suggests that the structure of the short range order fraction progressively disorganizes. A degradation of intermolecular hydrogen bonding has been observed by IR-spectroscopy in the temperature range 423-453 K [16]. The vertical arrows in figure 59-A correspond to glass transition temperatures reported in literature (arrow 1: ref [16], arrow 2: ref [17]).



Therefore, a glass transition seems to occur between 423 K and 473 K, followed by the carbonization at a higher temperature. Below this temperature (which corresponds to 150 °C), the structure remains stable. The crystalline fraction remains stable up to 498 K (225 °C). This temperature stability is surprisingly high given that the silk is made of protein which is usually a relatively heat-sensitive material.

### VI.3.2.2. Degradation of Fibroin chain

The Fibroin integrity has been checked in function of the heat treatment temperature by SDS-PAGE analysis. Figure 60 shows the result of this experiment (A: photo of the gel; B: graph of the results of the band quantification performed using FIT2D).

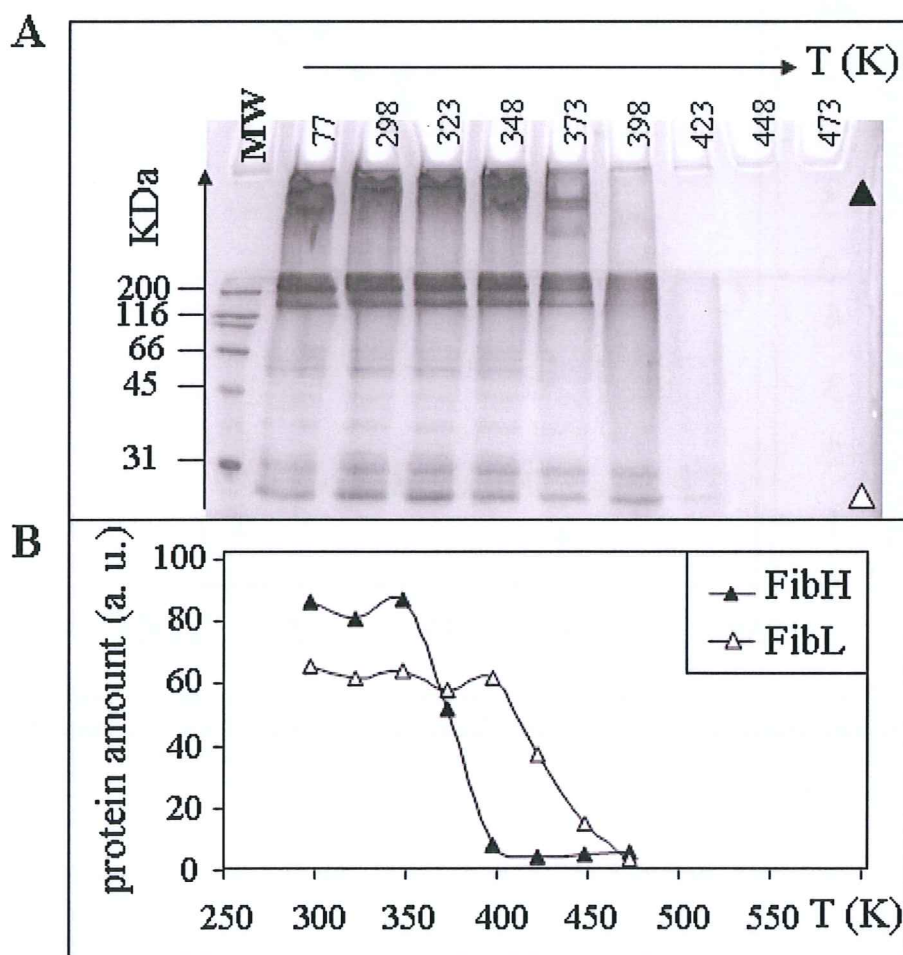


*Fig. 60: Evolution of Fibroin integrity in function of heat treatment temperature up to 473 K.*

The  $\beta$ -mercaptoethanol present in the sample buffer reduces the disulfide bond between the two peptidic chains of Fibroin (FibH and FibL), allowing their separate analysis.

FibH primary structure includes non-repetitive regions which are thought to take place in the amorphous and short range order fractions, and the GA-rich regions supposed to fold, at least partially, in the  $\beta$ -sheet composing the crystallites. The SDS-PAGE analysis shows that the FibH degradation occurs between 348 K and 398 K, that is to say at a much lower temperature than the crystallites destruction. Thus, this degradation most likely occurs in the non-crystallized parts of FibH. Fibl degradation occurs within exactly the same temperature range as the glass transition shown above. These two events could be linked as Fibl has a non-repetitive sequence and is therefore thought to be part of the amorphous matrix.

### VI.3.2.3. Degradation of Mechanical properties

The evolution of the mechanical properties of silk fibres has also been tested. Figure 61 summarizes the results of these tests.

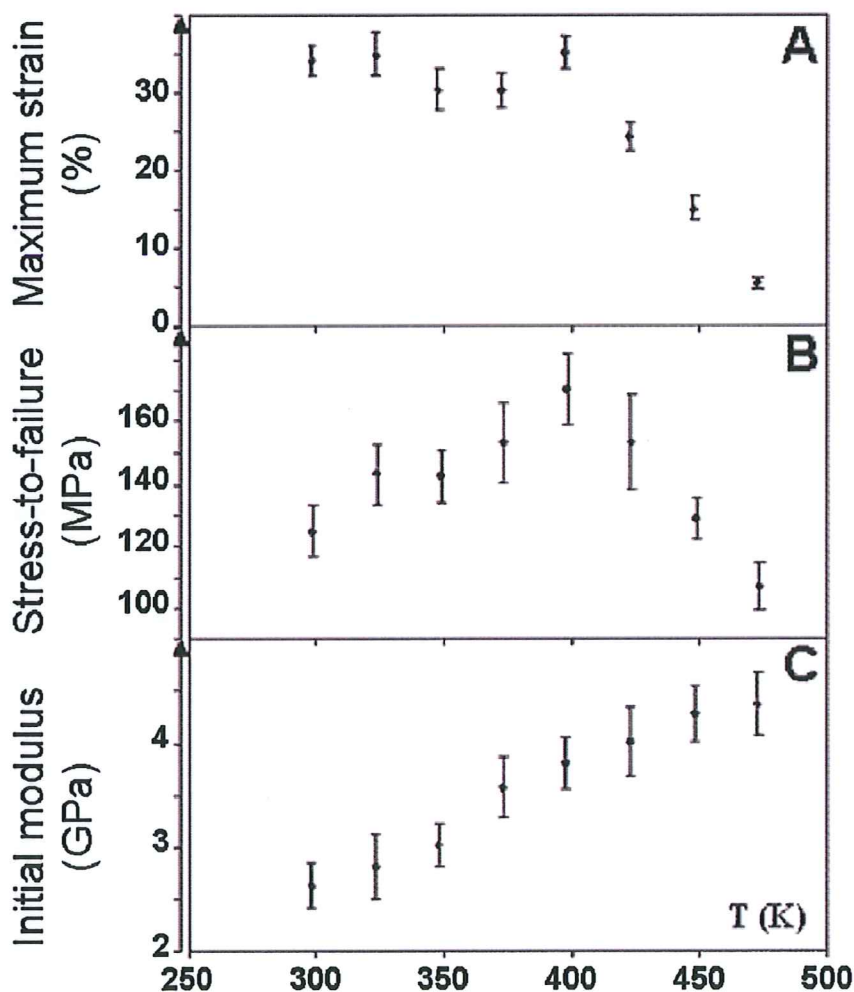


*Fig. 61: Evolution of silk fibre mechanical properties in function of heat treatment temperature up to 473 K: maximum strain (A), stress to failure (B) and initial modulus (C).*

Below 398 K, fibre strain remains stable and the stress-to-failure increases. Above this temperature, the strain and the stress to failure both decrease. The initial modulus of the stress/strain curve increases steadily with the temperature of heat treatment up to 473 K (figure 61-C). These results suggest a two-phase behaviour. Firstly, at temperatures up to 398 K, the stiffness of the fibres increases. The induced elastic deformation requires greater and greater force while the treatment temperature increases. This could result from the formation of cross-linking between peptide chains. Such an effect has been observed for collagen in which cross-linking is chemically triggered [18]. Then, above 398 K, the part of the curve representing the plastic deformation decreases revealing most likely disruptions inside the amorphous matrix. The temperature range of this second phase corresponds to that of the glass transition and Fibl degradation (see above). This experiment underlines the importance of the amorphous matrix in the mechanical properties of silk.

## VI.4. Conclusions

The present results show that the crystalline domains of *B. mori* silk start degrading only above about 500 K, which is comparable to dragline silk [2]. However, the thermal degradation of FibH and FibL molecules starts earlier in the 350-400 K range and therefore affects only the structure of the short-range order fraction. The mechanical properties such as ultimate tensile stress and strain to failure start to degrade at the onset of the FibH and FibL molecular degradation, suggesting a causal link. These results and an increase of the initial modulus up to about 475 K indicate that degradation in the amorphous fraction is accompanied by an increasing cross-linking. The close analogy to elastomeric polymers [19] suggests that models involving molecular springs [20] are not required for describing the mechanical properties.



## Bibliography

1. Martel, A., et al., *Thermal Behavior of Bombyx mori silk: Evolution of crystalline parameters, molecular structure, and mechanical properties*. *Biomacromolecules*, 2007. **8**(11): p. 3548-3556.
2. Glisovic, A. and T. Salditt, *Temperature dependent structure of spider silk by X-ray diffraction*. *Applied Physics a-Materials Science & Processing*, 2007. **87**(1): p. 63-69.
3. Termonia, Y., *Molecular Modeling of Spider Silk Elasticity*. *Macromolecules*, 1994. **27**(25): p. 7378-7381.
4. Riekel, C., et al., *Aspects of X-ray diffraction on single spider fibers*. *International Journal of Biological Macromolecules*, 1999. **24**(2-3): p. 179-186.
5. Sapede, D., et al., *Nanofibrillar structure and molecular mobility in spider dragline silk*. *Macromolecules*, 2005. **38**(20): p. 8447-8453.
6. Bram, A., et al., *X-ray diffraction from single fibres of spider silk*. *Journal of Applied Crystallography*, 1997. **30**: p. 390-392.
7. Takahashi, Y., M. Gehoh, and K. Yuzuriha, *Structure refinement and diffuse streak scattering of silk (Bombyx mori)*. *International Journal of Biological Macromolecules*, 1999. **24**(2-3): p. 127-138.
8. Sinsawat, A., et al., *X-ray diffraction and computational studies of the modulus of silk (Bombyx mori)*. *Polymer*, 2002. **43**(4): p. 1323-1330.
9. cryosystem,  
[www.oxfordcryosystems.co.uk/downloads/Cryostream%20Temp%20Profile%20along%20nozzle.pdf](http://www.oxfordcryosystems.co.uk/downloads/Cryostream%20Temp%20Profile%20along%20nozzle.pdf). access may 29, 2008.
10. Hammersley, A., *The FIT2D home page*. [www.esrf.eu/computing/scientific/FIT2D/](http://www.esrf.eu/computing/scientific/FIT2D/), accessed July 10, 2007.
11. Montes-Moran, M.A., et al., *Mechanical properties of high-strength carbon fibres. Validation of an end-effect model for describing experimental data*. *Carbon*, 2004. **42**(7): p. 1275-1278.
12. Davies, R.J., *A batch-wise non-linear fitting and analysis tool for treating large X-ray diffraction data sets*. *Journal of Applied Crystallography*, 2006. **39**: p. 262-266.
13. Davies, R.J., *A new batch-processing data-reduction application for X-ray diffraction data*. *Journal of Applied Crystallography*, 2006. **39**: p. 267-272.
14. Cunniff, P.M., et al., *Mechanical-Properties of Major Ampulate Gland Silk Fibers Extracted from Nephila-Clavipes Spiders*. *Silk Polymers*, 1994. **544**: p. 234-251.
15. Saito, Y. and T. Arima, *Cone structure of hexagonal carbon sheets stacked in wood cell lumen*. *Journal of Wood Science*, 2004. **50**(1): p. 87-92.
16. Nakamura, S., J. Magoshi, and Y. Magoshi, *Thermal-Properties of Silk Proteins in Silkworms*. *Silk Polymers*, 1994. **544**: p. 211-221.
17. Tsukada, M., et al., *Structural-Changes of Silk Fibers Induced by Heat-Treatment*. *Journal of Applied Polymer Science*, 1992. **46**(11): p. 1945-1953.
18. Yunoki, S. and T. Matsuda, *Simultaneous processing of fibril formation and cross-linking improves mechanical properties of collagen*. *Biomacromolecules*, 2008. **9**(3): p. 879-885.



19. Vollrath, F. and D. Porter, *Spider silk as archetypal protein elastomer*. *Soft Matter*, 2006. **2**(5): p. 377-385.
20. Becker, N., et al., *Molecular nanosprings in spider capture-silk threads*. *Nature Materials*, 2003. **2**(4): p. 278-283.

## **Chapter VII- PHYSICAL PROPERTIES OF SILK: The Effects of Pressure**

**Résumé de ce chapitre :**

Ce chapitre est consacré à l'étude de l'effet des hautes pressions sur la soie. Il fait suite à la révélation de la résistance de la soie à de hautes températures (jusqu'à 500 K). Très peu de données sont connues sur le comportement des protéines à hautes températures bien que ce type d'expériences soit un moyen intéressant d'observer le dépliement des protéines [2]. Les résultats préliminaires présentés ici suggèrent que l'augmentation de la pression de 2 KBar à 6 KBar entraîne une compression réversible des cristallites. Au delà de 6 KBar, la fraction cristalline disparaît progressivement témoignant probablement du dépliement des chaînes peptidiques composant les cristallites.

La compression a lieu le long des liaisons hydrogènes liant les brins  $\beta$  en feuillets. Elle est relativement faible comparée à l'expansion obtenue par chauffage (chapitre précédent). Ce résultat est comparable avec les données obtenues pour un autre peptide amyloïde : la protéine Prion sous sa forme Scrapie ( $\text{PrP}^{\text{Sc}}$ ) par Garcia *et al.* [3]. La pression de dépliement des cristallites de feuillets  $\beta$  mesurée ici (6 Kbar) correspond approximativement à la pression à laquelle  $\text{PrP}^{\text{Sc}}$  devient sensible à la protéinase K.

Ces résultats constituent les premières données chiffrées concernant le comportement de la soie aux hautes pressions. Cependant, ce sujet mériterait une investigation plus approfondie.

This chapter reports the influence of high pressure on the atomic structure of silk [4]. It has been shown by spectroscopic techniques that high pressure results in unfolding of many protein and aggregate amyloidal peptides which can start to dissociate [2]. SAXS studies under high pressure have been performed mostly on proteins in solution using hydrostatic piston-type cells [5-7]. Several high pressure experiments on protein single crystals have also been reported using diamond Anvil cells (DAC) although large-scale transformations were not addressed in these studies [8, 9]. However, very few studies have been performed on fibrous polymers using DAC [10]. The high pressure experiments on natural silk reported in this chapter could be of practical interest for understanding amyloid peptides folding. Indeed high pressure has been shown to affect the folding and consequently the infectivity of the Scrapie form of Prion protein PrP<sup>Sc</sup> [3].

## VII.1. Experiments

### VII.1.1. Sample and sample environment

Two experiments have been carried out on natural silk baves on ID13. Hydrostatic pressure was applied using a DAC, as described in [1]. This device is depicted figure 62.



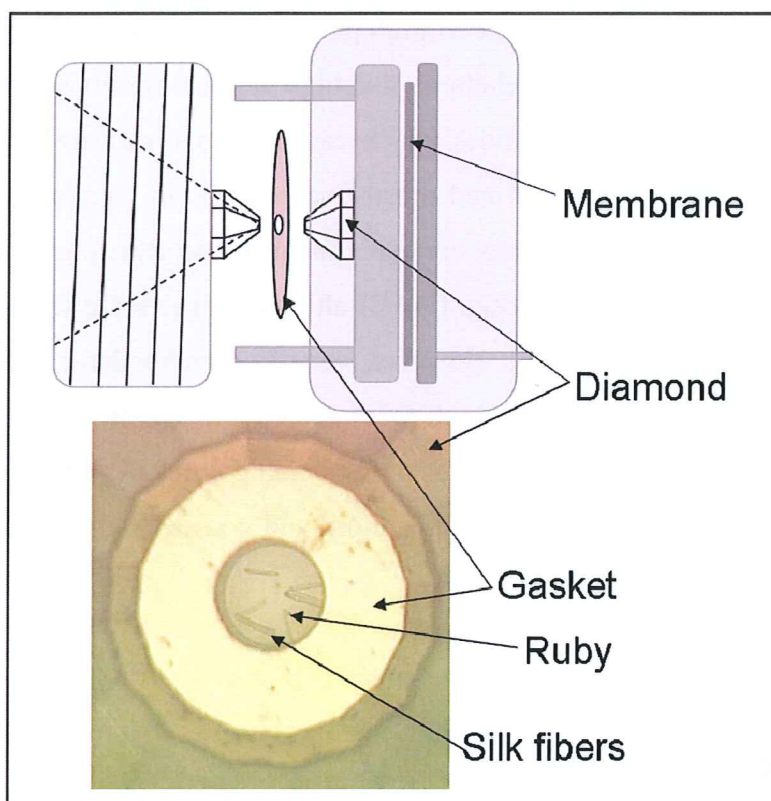


*Fig. 62: Scheme of the diamond anvil cell [1] (Top) and microscopic image of the sample inside (Bottom).*

100  $\mu\text{m}$  long silk fibers are placed in a hole of 250 $\mu\text{m}$  diameter drilled in a copper gasket by electro-erosion. The sample is surrounded by water which distributes the pressure so that it is uniform in all directions. A ruby is also placed in the gasket for pressure calibration. This gasket is placed between two cone-shaped diamonds. The cell is closed by screwing which applies an initial pressure. A larger pressure can be applied on one of the diamonds which focuses it on the gasket content.

## VII.1.2. Diffraction experiment

In both experiments, the X-ray wavelength was 0.961 Å and the detector is a Frelon camera with pixels binned to 2 x 2. For 1 mm diameter diamond windows, the transmission of the DAC at this wavelength is about 50 %. The distance between the sample and the detector is 101.4 mm in the first experiment and 61 mm in the second one. Each X-ray exposure lasts 2 s in the first experiment and 5 s in the second one. The beam measures 2.5 µm horizontally and 4.5 µm vertically.

A series of WAXS patterns recorded along each fibre with a step size of 1 µm was averaged. Two similar series of background, taken at each side of the fibres, were also averaged and subtracted from the silk averaged pattern. Patterns were recorded during progressive pressure increase and several hours after pressure release in order to estimate the reversibility of the observed phenomenon. Patterns were analyzed using the FIT2D, POI and SCM programs [11-13].

## VII.2. Results and discussion

The high pressure cell results in a high background level due to the various materials that the beam has to traverse. In particular, the scattering of water is high compared to the silk signal and the background is difficult to subtract because of shadowing effect of the rest of the cell depending on the position inside the cell. The patterns recorded in the first experiment show a weak equatorial peak. The 210 and 020 reflections could not be separated and the peak profile was fitted by a single Gaussian function. The evolution of the position and integral intensity of this Gaussian are plotted in function of pressure in figure 63.

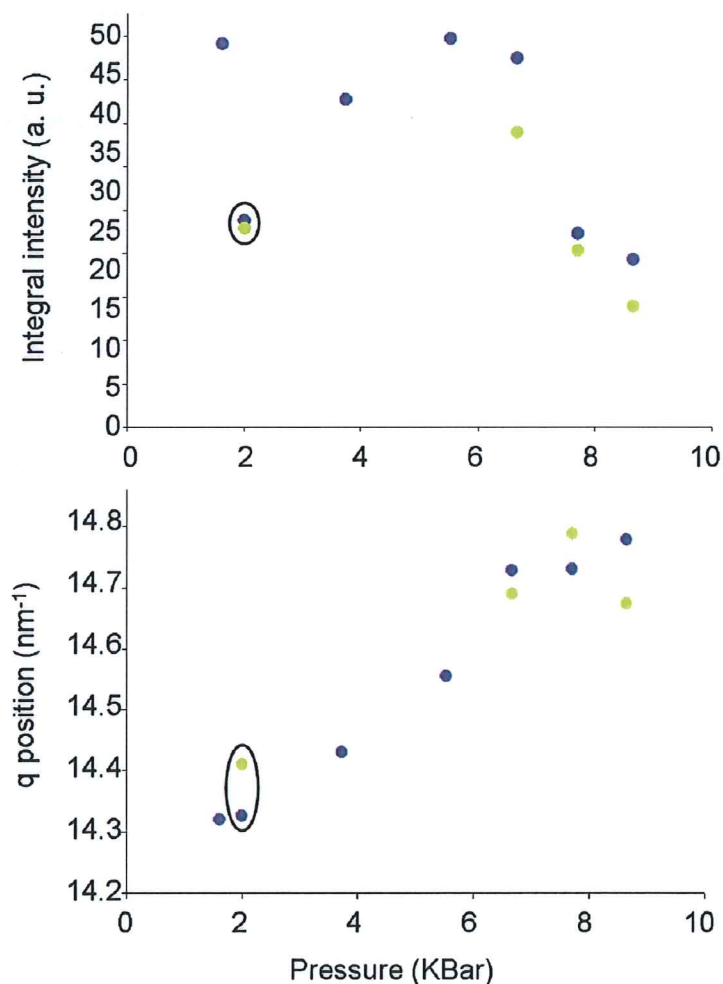


*Fig. 63: Pressure dependence of the equatorial peak integral intensity (Top) and q-position (Bottom). The two colors represent two different baves. The data marked by a circle are recorded after pressure release.*

---

The two colors represent two baves and the ringed data are recorded eight hours after pressure release. The 002 reflection position and the azimuthal width of the equatorial peak do not change. These results suggest a two-phase process: from 2 Kbars to 7 Kbars, the  $q$ -position of the equatorial peak increases, which corresponds to a compaction of the crystalline domains. Above 7 Kbars, the peak intensity decreases, which suggests a disorganization of the crystalline domains, possibly due to the unfolding of the peptide chains folded into  $\beta$ -sheets. Upon pressure release, the equatorial peak returns to its initial position showing that the remaining crystalline domains recover their initial unit cell parameters. However, the peak intensity does not return to its initial value, which implies that, within a time scale of hours, only a fraction of the unfolded peptide chains recover their pleated  $\beta$ -sheet conformation. These results suggest that, up to 7 Kbars, the crystalline domains can compact reversibly. Above this threshold, most of them unfold in an almost irreversible way.

The experiment has been repeated with an improved statistic, i. e. a better signal/noise ratio. This allowed us to fit the 210 and 020 reflections separately, and therefore, to estimate the changes of individual cell parameters. Figure 64 shows the results of this experiment.



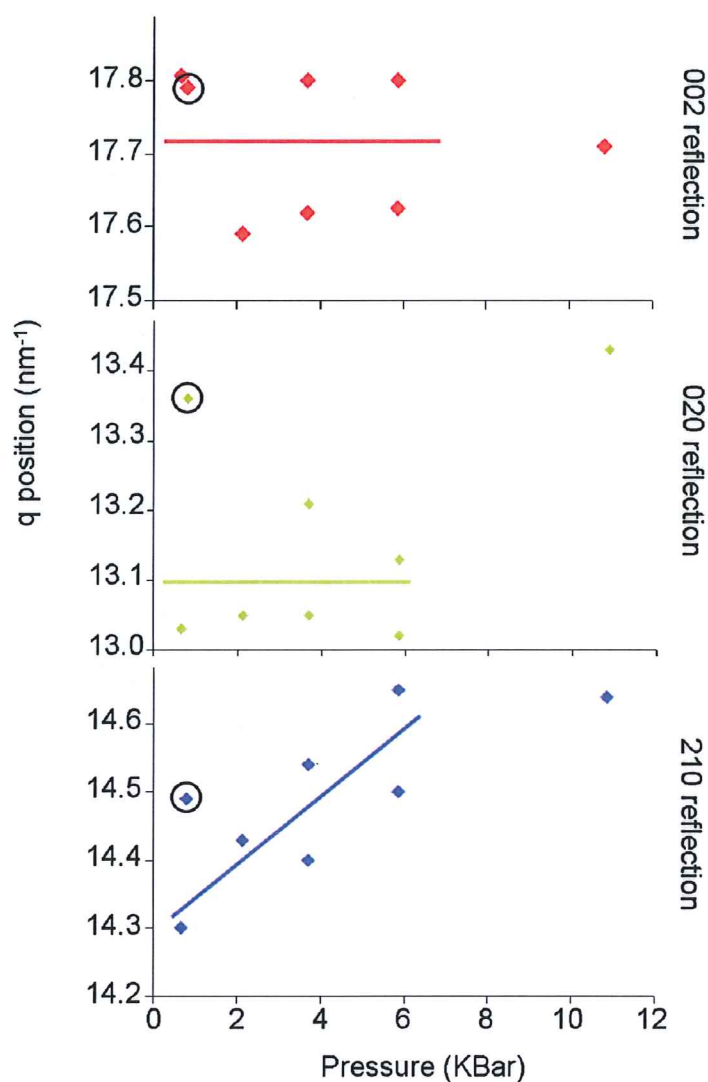


*Fig. 64: Pressure dependence of the three main reflections. The ringed data are recorded after pressure release.*

The results show that the 210 reflection is the most affected by pressure (the last point should be ignored as the advanced destruction of the crystallites does not allow a good quality fitting). This means that the crystallites are reversibly compressible along the a-axis direction of the unit cell which is the direction of hydrogen bonding between the  $\beta$ -strands constituting the  $\beta$ -sheets.

Together with the result of thermal expansion exposed in the previous chapter, these results provide information on the changes in dimensions of the crystalline domains under external forces. They can thermally expand in the direction of  $\beta$ -sheet pleating (unit cell b

---

axis) and in the hydrogen bonds direction (unit cell a axis) upon heating. However, they can only compact in the hydrogen bonds direction under pressure.

These preliminary results provide a first quantitative measurement of the silk stability to high pressure. They are in agreement with the results of Garcia *et al.* [3]. Indeed, the pressure of unfolding of the crystallites (around 6 KBar) corresponds to the pressure of increase in sensitivity to protein K of the PrP<sup>Sc</sup> protein around 5 Kbar at 60 °C. The results shown above display a large variability. The quality of the data treatment should be improved. If not possible, a large number of measurements should be taken to produce statistically reliable data.

These new insights into the physical properties of silk provide further reasons to mimic this astonishing biopolymer.

## Bibliography

1. Gebhardt, R., et al., *High-pressure potato starch granule gelatinization: Synchrotron radiation Micro-SAXS/WAXS using a diamond anvil cell*. *Biomacromolecules*, 2007. **8**(7): p. 2092-2097.
2. Meersman, F., C.M. Dobson, and K. Heremans, *Protein unfolding, amyloid fibril formation and configurational energy landscapes under high pressure conditions*. *Chemical Society Reviews*, 2006. **35**(10): p. 908-917.
3. Garcia, A.F., et al., *Reduced proteinase K resistance and infectivity of prions after pressure treatment at 60 degrees C*. *Journal of General Virology*, 2004. **85**: p. 261-264.
4. Fraser, R.D.B. and T.P. MacRae, *Conformation in fibrous proteins*. New York: Academic Press, 1973.
5. Pressl, K., et al., *High pressure cell for small-and wide-angle x-ray scattering*. *Review of Scientific Instruments*, 1997. **68**(12): p. 4588-4592.
6. Steinhart, M., et al., *High-pressure instrument for small- and wide-angle x-ray scattering. II. Time-resolved experiments*. *Review of Scientific Instruments*, 1999. **70**(2): p. 1540-1545.
7. Kato, M. and T. Fujisawa, *High-pressure solution X-ray scattering of protein using a hydrostatic cell with diamond windows*. *Journal of Synchrotron Radiation*, 1998. **5**: p. 1282-1286.
8. Fourme, R., et al., *High-pressure protein crystallography (HPPX): instrumentation, methodology and results on lysozyme crystals*. *Journal of Synchrotron Radiation*, 2001. **8**: p. 1149-1156.
9. Fourme, R., et al., *High-pressure macromolecular crystallography (HPMX): Status and prospects*. *Biochimica Et Biophysica Acta-Proteins and Proteomics*, 2006. **1764**(3): p. 384-390.
10. Czeslik, C., et al., *High pressure synchrotron X-ray diffraction studies of biological molecules using the diamond anvil technique*. *Nuclear Instruments & Methods in Physics Research Section a-Accelerators Spectrometers Detectors and Associated Equipment*, 1996. **368**(3): p. 847-851.
11. Hammersley, A., *The FIT2D home page*. [www.esrf.eu/computing/scientific/FIT2D/](http://www.esrf.eu/computing/scientific/FIT2D/), accessed July 10, 2007.
12. Davies, R.J., *A batch-wise non-linear fitting and analysis tool for treating large X-ray diffraction data sets*. *Journal of Applied Crystallography*, 2006. **39**: p. 262-266.
13. Davies, R.J., *A new batch-processing data-reduction application for X-ray diffraction data*. *Journal of Applied Crystallography*, 2006. **39**: p. 267-272.

# CONCLUSION AND PERSPECTIVES

## C&P.1. Conclusion

Scientists have been trying to mimic silk fibres and to elucidate its formation process for a long time. This pluridisciplinary thesis work contributes to this effort by observing the silk formation in a microfluidic device using synchrotron radiation and Raman spectroscopy. Silk is a biopolymer composed of fibrillar protein. Its semi-crystalline structure is composed of pleated  $\beta$ -sheet crystallites embedded in an amorphous matrix. Its mechanical properties combine a high strain with a good stress-to-failure. Silk is often compared to high performance man-made fibres such as Kevlar<sup>®</sup> although it is spun by arthropods at room temperature and without any organic solvent. Although less attractive than spider silk, *Bombyx mori* silk has been investigated in this study because of the ease with which its protein can be obtained. This choice is justified by the many similarities in formation, structure and properties that exist between *B. mori* silk and spider silk.

The microfluidic device developed in this thesis work aims to mimic natural spinning conditions of silk. It has a concentric geometry and reproduces the pH decreases and the tapering of the Fibroin flow found in the *B. mori* spinning apparatus. In addition, it responds to the technical constraints of observation by X-ray scattering.

SAXS analysis of the first steps of silk formation in the microfluidic chip shows that Fibroin undergoes an aggregation in clusters of determined size. In these clusters, it has been proved that Fibroin is in a compacted conformation compared to its form in aqueous solution. In a second step, these clusters seem to compact.

Raman spectroscopy experiments show that, if dried at this point of its structural organization, Fibroin has a silk I structure, that is to say a random coil rich conformation. However, if kept in water, it converts to the hydrated precursor of Silk II. This conversion seems to imply a conformational transition from  $3_1$ -helix and random coil structures to  $\beta$ -sheet structure and a pleating of these  $\beta$ -sheet into crystallites (as observed by WAXS). It is accompanied by a change in tyrosines' average environment from a very hydrophobic



medium to an environment where they link strong hydrogen bonds, being most likely involved in the connection between the crystallites and the amorphous matrix.

The second axis of this thesis is dedicated to the improvement of knowledge on the physical properties of natural *B. mori* silk. The investigation of structural behaviour of silk under high temperature reveals that the crystallites' structure remains stable until carbonization although the Fibroin peptide chain is already degraded. The short range order fraction analysis reveals that a glass transition occurs in the material before its carbonization. This glass transition is accompanied by changes in the mechanical properties probably due to an increase of cross linking between peptide chains in the amorphous matrix. The preliminary investigation of structural behaviour of silk under high pressures shows that the crystallites can undergo a slight compaction before their disorganization. The combined results of these two investigations underline the silk's outstanding structural resistance to high pressures and temperatures, providing further reasons to mimic this fibre.

## C&P.2. Perspectives

The main perspective of this work is to improve the microfluidic device in such a way that it becomes closer to the *B. mori* spinning apparatus. This requires implementing the sequential addition of chemicals along the mixing channel. The shearing forces which occur during natural spinning should also be mimicked. To start with, the freshly spun fibres could be wound up around rolls placed in the collection bath. In a further development, this step should be included directly in the microfluidic device by constriction of the mixing tube.

The application of this protein folding analysis method to other peptides would be of great interest. For instance, it could be directly applied to spider silk protein aggregation study and to pathogenic amyloidal peptides to better understand their misfolding mechanisms. Folding of other molecules, such as DNA packing for instance, could also be investigated using these tools.

The pressure effects on silk fibre should be further studied. In particular, it would be interesting to follow the disorganization of silk's structure simultaneously by Raman spectroscopy and WAXS to determine the secondary structure evolution.

### C&P.3. Conclusion

Les scientifiques tentent de mimer la fibre de soie et de découvrir son processus de formation. Ce travail pluridisciplinaire contribue à cet effort en observant la formation de la soie dans un système microfluidique en utilisant les techniques de diffusion des rayons X et de spectroscopie Raman. La soie est un bio-polymère constitué de protéine Fibrillaire. Sa structure semi-cristalline est composée de cristallites de feuillets  $\beta$  empilés, incluses dans une matrice amorphe. Ces propriétés mécaniques combinent une haute extensibilité et un stress maximum élevé. La soie est souvent comparée à des fibres synthétiques de haute qualité. Pourtant, sa fabrication par quelques arthropodes ne nécessite ni conditions particulières de température ou de pression, ni solvant organique. La soie de *Bombyx mori* a été choisie comme objet de cette étude en raison de la facilité d'obtention de ses protéines (Fibroïne), malgré des propriétés moins attractives que celles de la soie d'araignée. Ce choix se justifie par les similarités de formation de structure et de propriétés qui existent entre la soie de *B. mori* et la soie d'araignée.

Le système microfluidique développé au cours de ce travail de thèse afin de mimer les conditions naturelles de synthèse de la soie, possède une géométrie concentrique et reproduit la chute de pH et l'amincissement du canal observé dans l'appareil de filage du ver à soie. De plus, il répond aux contraintes techniques dictées par l'utilisation de la diffusion des rayons X comme méthode d'observation.

L'analyse par SAXS des premières étapes de la formation de la soie dans une cellule microfluidique montre que la Fibroïne subit une agrégation en particules de taille définie. Dans ces agrégats, il a été démontré que la Fibroïne adopte une conformation plus compacte que lorsqu'elle se trouve en solution aqueuse. Dans un second temps, les agrégats semblent se compacter.

Des expériences de spectroscopie Raman montrent que si la fibre ainsi formée est séchée à ce stade de son organisation structurale, la Fibroïne présente une conformation de type Silk I, c'est-à-dire une structure secondaire principalement amorphe. Cependant, si la fibre est laissée dans l'eau, sa structure se convertit en un précurseur hydraté de Silk II. Cette conversion pourrait impliquer une transition conformationnelle de structures en hélice  $3_1$  et en coude vers des feuillets  $\beta$  et l'empilement de ces feuillets  $\beta$  en cristallites (observées par WAXS). Elle est également caractérisée par le passage des tyrosines d'un environnement très



hydrophobe à un environnement où elles sont impliquées dans de fortes liaisons hydrogènes, faisant probablement le lien entre les cristallites et la matrice amorphe.

Le second axe de cette thèse est dédié à l'amélioration des connaissances des propriétés physiques de la soie. L'étude du comportement structural de la soie en conditions de hautes températures révèle que la structure des cristallites demeure stable jusqu'à la carbonisation, alors même que la chaîne peptidique de la Fibroïne est dégradée. L'analyse de la fraction partiellement ordonnée montre qu'une transition vitreuse s'opère avant la carbonisation. Cette transition vitreuse est accompagnée d'une modification des propriétés mécaniques de la fibre, sans doute expliquée par une augmentation du nombre de liaisons entre les chaînes peptidiques dans la matrice amorphe. L'étude préliminaire de l'effet des hautes pressions sur la structure de la soie montre que les cristallites peuvent se compacter légèrement avant de se désorganiser. L'ensemble de ces résultats souligne l'étonnante résistance de la structure de la soie aux hautes pressions et températures, donnant des raisons supplémentaires de tenter de mimer ce polymère.

## C&P.4. Perspectives

La principale perspective de ce travail est l'amélioration de la cellule microfluidique dans le but de se rapprocher des conditions naturelles de synthèse de la soie. Ceci requiert la possibilité d'ajouter séquentiellement des composés chimiques tout au long du canal de mélange. Les forces de cisaillement qui sont présentes lors de la synthèse naturelle de la soie doivent également être émulées. Pour commencer, la fibre fraîchement produite pourra être enroulée autour de rouleaux placés dans le bain de collection. Dans un deuxième temps, cette étape devra être incluse directement dans la cellule microfluidique par constriction du canal de mélange.

Cette méthode d'observation du repliement des protéines est applicable à d'autres peptides. Par exemple, elle pourrait être directement employée pour étudier le repliement des protéines de soie d'araignée ou des peptides amyloïdes pathogènes afin de mieux comprendre les facteurs conduisant à leur mauvais repliement. D'autres phénomènes biologiques, comme par exemple la compaction de l'ADN, pourraient être investigués grâce à ces outils.

L'effet de la pression sur la structure de la fibre de soie mériterait d'être étudié plus précisément. En particulier, il serait intéressant de combiner les techniques de WAXS et de

---

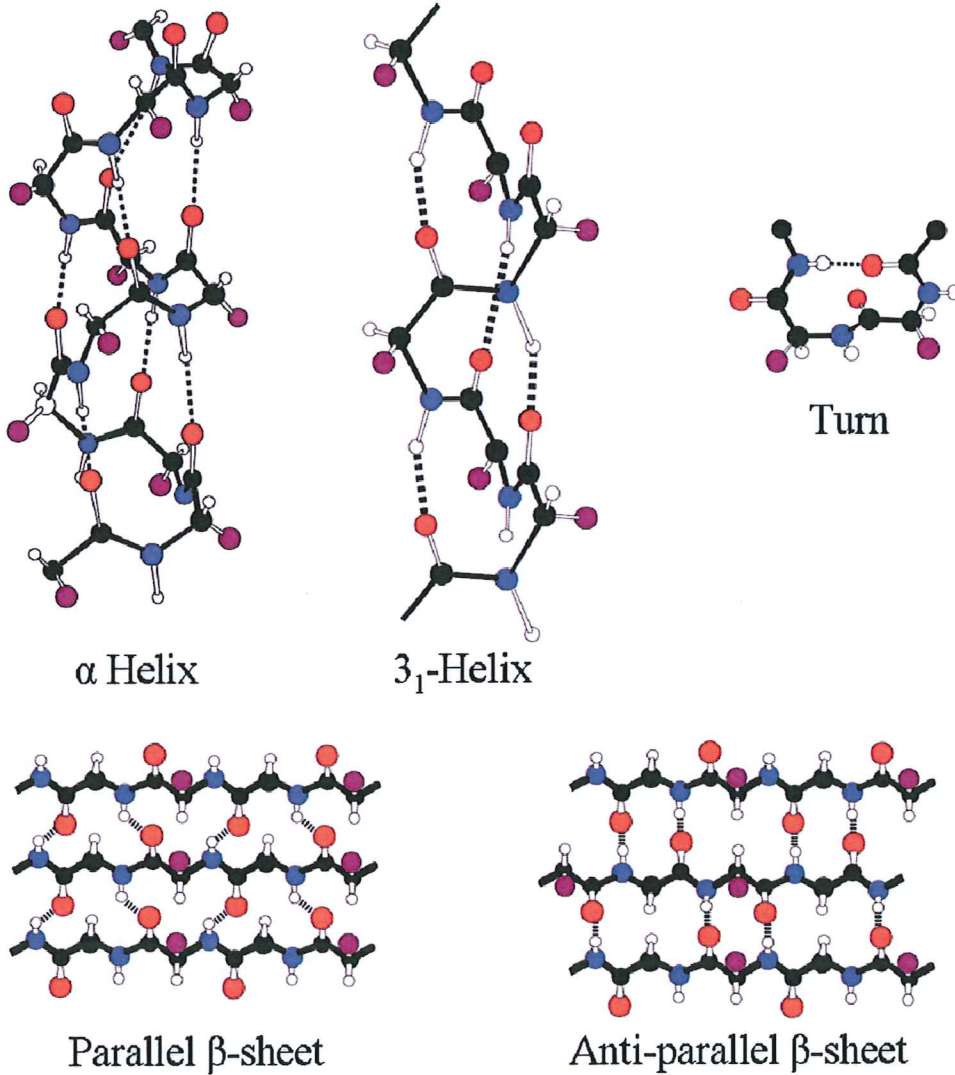
spectroscopie Raman afin de suivre l'évolution des structures secondaires lors de la désorganisation des cristallites.













# APPENDIX I

## Common Protein Secondary Structures



### Legend:

-  Peptide bond
-  Other covalent bond
-  Hydrogen bond

-  Oxygen atom
-  Nitrogen atom
-  Carbon atom
-  Lateral chain
-  Hydrogen atom



## APPENDIX II

### ID13 and ID02 beamline layouts

The SAXS and WAXS experiments mentioned in this thesis report have been done on ID02 [1] and ID13 [2] ESRF beamlines. This appendix provides a brief description of those beamlines and a layout of the equipment that have been used in this thesis work.

#### ID13 - Microfocus beamline

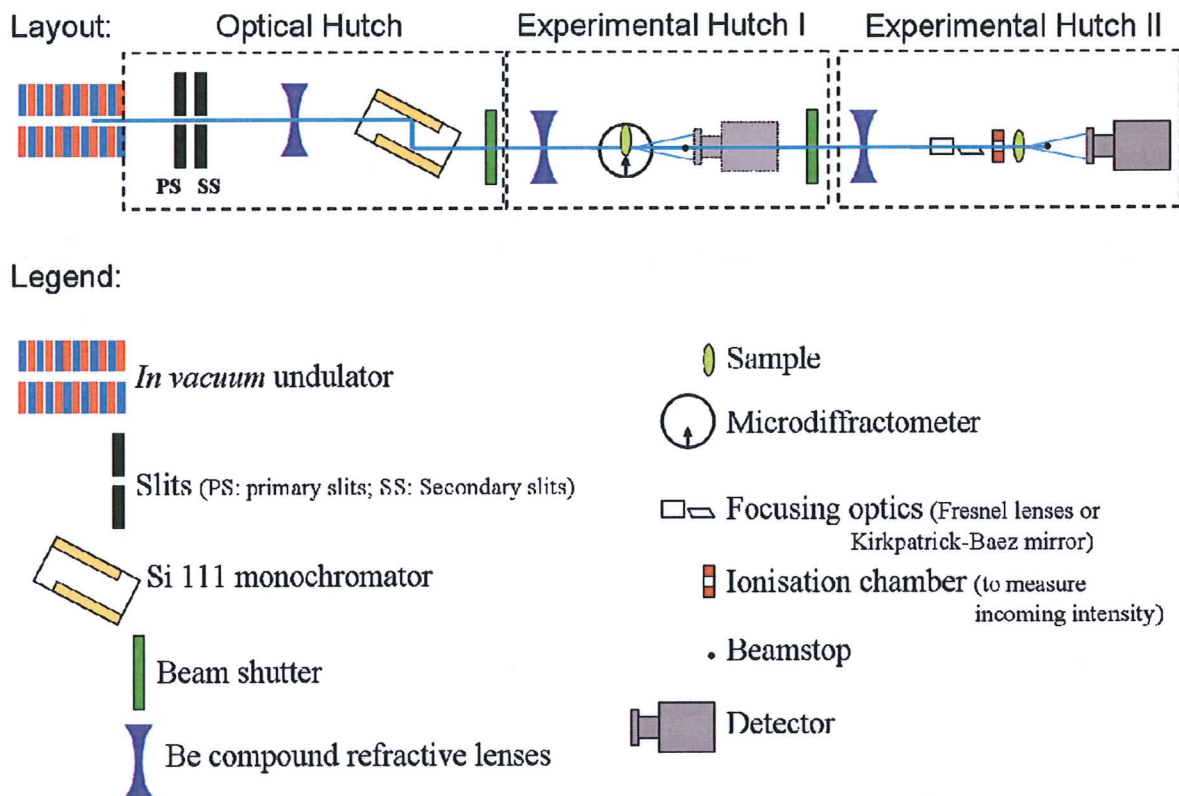


Fig. 65: Layout of ID13 equipment used in this thesis work.

The aim of ID13 beamline is to provide micron and sub-micron sized beams for a range of applications, in particular in soft matter science and biology [2]. The principal beamline components which have been used in this work are shown schematically in figure



65. An *in vacuum* low  $\beta$  undulator is used as radiation source. The optical hutch contains a Si 111 monochromator cooled by liquid  $N_2$ . The usual wavelength is around  $0.96 \text{ \AA}$ . The beam is focused in two experimental hutches (EH1 and EH2) by various optics, including refractive Be lenses [3], Fresnel lenses [4], or Kirkpatrick-Baez mirror [5], to typical sizes between  $1 \text{ \mu m}$  and  $5 \text{ \mu m}$ . EH1 contains a microdiffractometer and is used principally for single crystal diffraction. EH2 contains a scanning set up which provides a variable platform for a range of experiments with different sample environments. The detectors used in this work are a Mar165 CCD camera with a 165 mm diameter converter screen ( $2048 \times 2048$  pixels; pixel size =  $64.45 \text{ \mu m} \times 64.45 \text{ \mu m}$ ; 16 bit readout; readout speed of a few seconds per pattern) and a Frelon camera with a 110 mm diameter converter screen ( $2048 \times 2048$  pixels; pixel size =  $50 \text{ \mu m} \times 50 \text{ \mu m}$ ; 16 bit readout; readout speed up to 10 Hz [6]).

## ID02 - High brilliance beamline

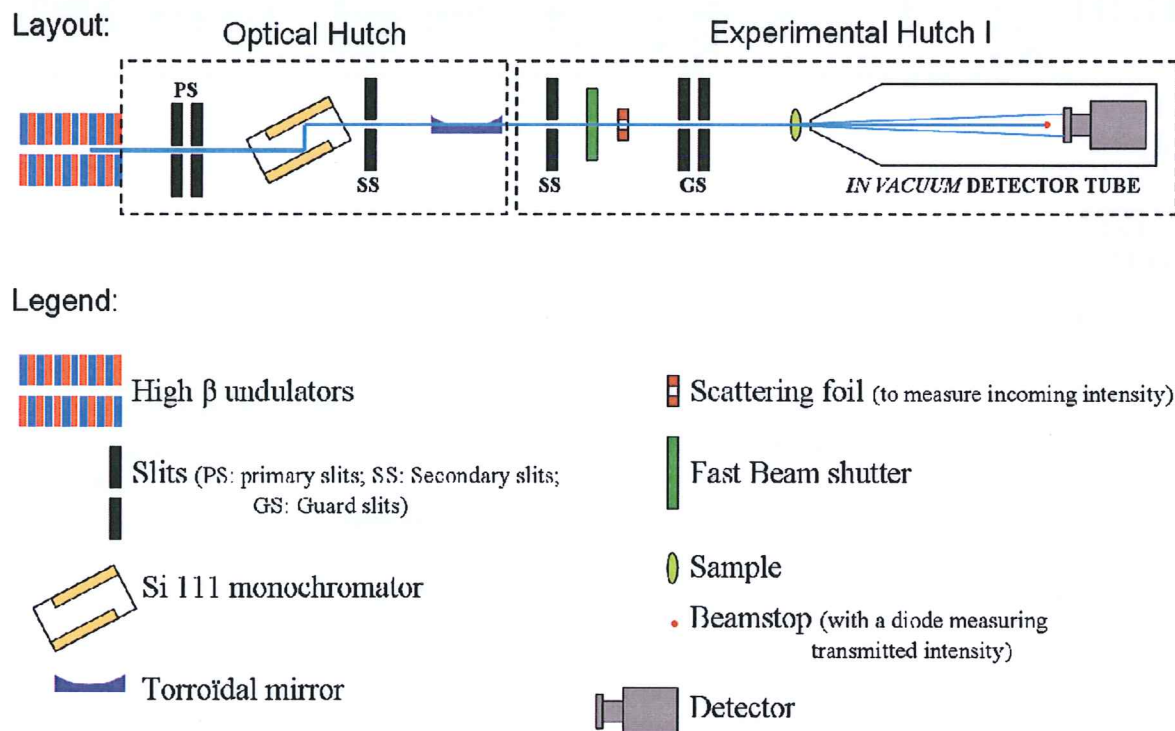


Fig. 66: Layout of ID02 equipment used in this thesis work.

---

ID02 beamline is designed for combined SAXS-WAXS and time-resolved experiments. The source is made of three high  $\beta$  undulators providing a high photon flux. The optical hutch contains a Si 111 monochromator cooled by liquid N<sub>2</sub>. The usual wavelength is around 1 Å. There are two separate experimental stations: one for combined SAXS/WAXS and the other for USAXS. In the SAXS/WAXS experimental hutch, the distance between the sample and the SAXS detector can vary from 1 m to 10 m. On this distance, scattered X-rays travel in vacuum to reduce scattering and absorption by air. The typical size of the beam is 200  $\mu\text{m}$  and the maximum photon flux  $3.0 \cdot 10^{13}$  photons/sec/100 mA. This experimental station can be combined with various sample environment such as stopped flow system and rheometer. The detector used in this work is a Frelon camera with a 110 mm diameter converter screen (2048 x 2048 pixels; pixel size = 50  $\mu\text{m}$  x 50  $\mu\text{m}$ ; 16 bit readout; readout speed up to 10 Hz [6]).

---

## Bibliography

1. Narayanan, T., O. Diat, and P. Bosecke, *SAXS and USAXS on the high brilliance beamline at the ESRF*. Nuclear Instruments & Methods in Physics Research Section a-Accelerators Spectrometers Detectors and Associated Equipment, 2001. **467**: p. 1005-1009.
2. Riekel, C., *New avenues in x-ray microbeam experiments*. Reports on Progress in Physics, 2000. **63**(3): p. 233-262.
3. Lengeler, B., et al., *Parabolic refractive X-ray lenses: a breakthrough in X-ray optics*. Nuclear Instruments & Methods in Physics Research Section a-Accelerators Spectrometers Detectors and Associated Equipment, 2001. **467**: p. 944-950.
4. Noehammer, B., et al., *Coherence-matched microfocusing of hard x rays*. Applied Physics Letters, 2005. **86**(16): p. -.
5. Hignette, O., et al., *Submicron focusing of hard X-rays with reflecting surfaces at the ESRF*. SPIE Conference Proceedings edited by McNulty, 2001: p. 105.
6. Labiche, J.C., et al., *Invited article: The fast readout low noise camera as a versatile x-ray detector for time resolved dispersive extended x-ray absorption fine structure and diffraction studies of dynamic problems in materials science, chemistry, and catalysis*. Review of Scientific Instruments, 2007. **78**(9): p. -.

## APPENDIX III

### Calculation of flow diffusion

This appendix presents an example of flow diffusion calculation and introduces important approximations used in this calculation. The chip used for the experiment presented in chapter III is made of a round tube having an inner diameter of  $D_{in} = 700 \mu\text{m}$  and an outer diameter of  $D_{out} = 870 \mu\text{m}$  (Figure 67). This tube is inserted in an outer capillary of square section having an inner diameter of  $L = 1050 \mu\text{m}$ . Before the end of the inner tube, the Fibroin flow has a cross section area of  $S_{Fib} = \pi.(D_{in}/2)^2 = 0.3848 \text{ mm}^2$  and the pH2 buffer has a cross section of  $S_{Buff} = L^2 - [ \pi.(D_{out}/2)^2 ] = 0.508 \text{ mm}^2$ . The Fibroin solution flows in the inner tube at a rate of  $R_{Fib} = 500 \mu\text{L/hr}$  which corresponds to a velocity of  $\bar{U}_{Fib} = R_{Fib} / S_{Fib} = 1300 \text{ mm/hr}$ . The buffer flows at a rate of  $R_{Buff} = 660 \mu\text{L/hr}$  which corresponds to the same velocity  $\bar{U}_{Buff} = \bar{U}_{Fib}$ . After the mixing point, the total solution flows at a rate of  $R_{Tot} = R_{Fib} + R_{Buff} = 1160 \mu\text{L/Hr}$  which corresponds to a velocity of  $\bar{U}_{Tot} = R_{Tot} / L^2 = 1052 \text{ mm/hr} = 3.10^{-4} \text{ m/s}$ .

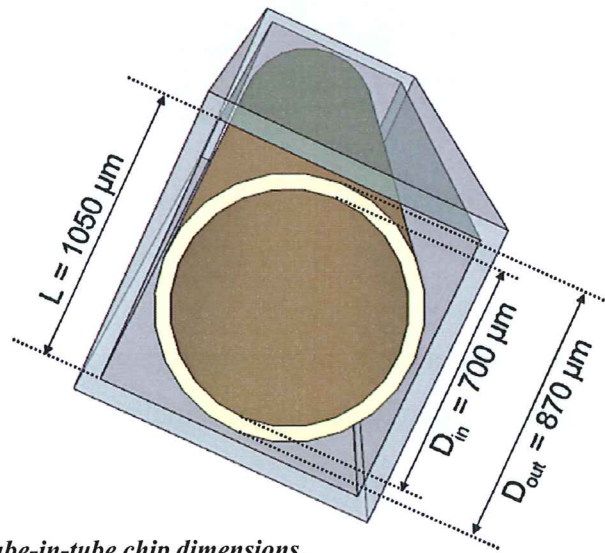


*Fig. 67 : Tube-in-tube chip dimensions.*

Assuming two important approximations: i) a flat velocity profile and ii) an equal viscosity of both solutions, then the cross section area in the mixing region is shared by the fluids in proportion of their respective flow rates  $S_{Fib}^{Mix} = L^2 \times (R_{Fib} / R_{Tot}) = 0.475 \text{ mm}^2$ . From this surface, the radius of the Fibroin flow can be deduced  $r_{Fib}^{Mix} = (S_{Fib}^{Mix} / \pi)^{1/2} = 389 \mu\text{m}$ .



The Fibroin molecule is larger than a proton. Therefore, the diffusion of Fibroin is negligible compared with the diffusion of the protons present in the pH2 buffer. The diffusion coefficient of the protons is  $D_{H^+} = 3 \cdot 10^{-9} \text{ m}^2/\text{s}$ . The half-width of the diffusion cone,  $Y$ , at a distance  $X$  from the end of the inner tube, can be calculated by  $Y = (2 \cdot D \cdot X / \bar{U}_{\text{Tot}})^{1/2}$  ( see Chapter II, Microfluidic section). At the first point of measurement  $X_{\text{start}} = 500 \text{ }\mu\text{m}$ ,  $Y_{\text{start}} = 100 \text{ }\mu\text{m}$ . At the last point of measurement  $X_{\text{end}} = 7.5 \text{ mm}$ ,  $Y_{\text{end}} = 390 \text{ }\mu\text{m}$ .  $Y_{\text{end}}$  is larger than  $r_{\text{Fib}}^{\text{Mix}}$ , which means that the protons diffused completely across the Fibroin solution, the mixing is complete (Figure 68). At the first point of measurement,  $X_{\text{start}}$ , the solutions are mixing from  $T_{\text{start}} = X_{\text{start}} / \bar{U}_{\text{Tot}} = 1.7 \text{ s}$ . At the last point, they are mixing for  $T_{\text{end}} = X_{\text{end}} / \bar{U}_{\text{Tot}} = 25.7 \text{ s}$ .

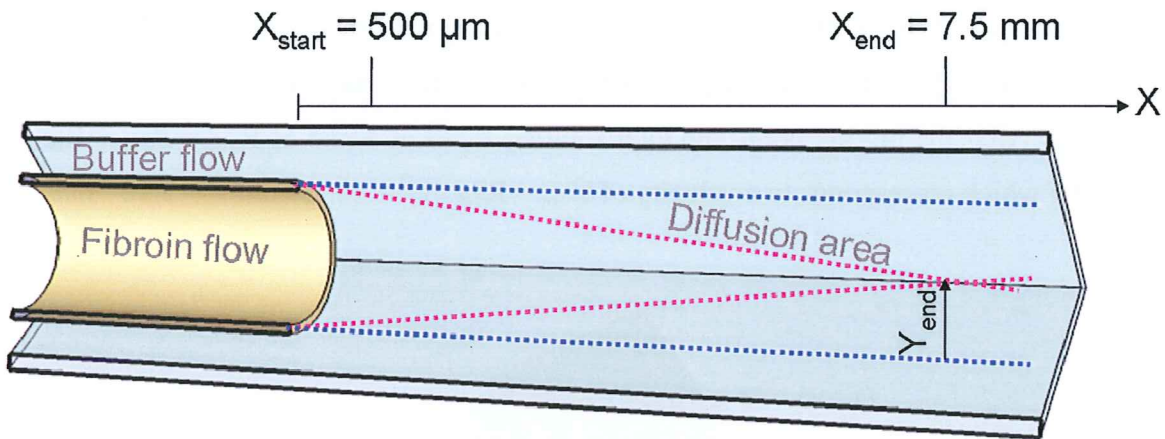


*Fig. 68: Scheme of the diffusion mixing process between the Fibroin solution and the pH2 buffer in the tube-in-tube chip.*

This calculation is very simplified: it involves important approximations. The resulting values are only indicative and were used to choose the initial experimental conditions.

## APPENDIX IV

### A microfluidic cell for studying the formation of regenerated silk by synchrotron radiation small- and wide-angle X-ray scattering

**Anne Martel<sup>1</sup>, Manfred Burghammer<sup>1</sup>, Richard Davies<sup>1</sup>, Emanuela DiCola<sup>1</sup>, Pierre Panine<sup>2</sup>, Jean-Baptiste Salmon<sup>3</sup> and Christian Riek<sup>1</sup>**

<sup>1</sup> European Synchrotron Radiation Facility, B.P. 220, F-38043 Grenoble Cedex, France

<sup>2</sup> Xenocs SAS, 19, rue Francois Blumet, 38360 Sassenage, France

<sup>3</sup> LOF, Unité mixte CNRS-Rhodia, 178 av. Schweitzer, 33608 Pessac, France

A tube-in-square-pipe microfluidic glass-cell has been developed for studying the aggregation and fiber formation from regenerated silk solution by in-situ small-angle X-ray scattering using synchrotron radiation. Acidification-induced aggregation has been observed close to the mixing point of the Fibroin and buffer solution. The fibrous, amorphous material is collected in a water bath. Micro-wide-angle X-ray scattering of the dried material confirms its  $\beta$ -sheet nature.

## I. INTRODUCTION

There is considerable interest in mimicking silk fibers produced by spiders and silk worms in view of their remarkable mechanical properties. While the structure and function of spinning ducts in spiders[1] and silk worms[2, 3] have been studied extensively, microscopic models of silk protein (Fibroin) aggregation and silk fiber formation have still to be experimentally verified.[1, 4, 5] In-situ synchrotron radiation (SR) micro-small-angle X-ray and micro-wide-angle X-ray scattering ( $\mu$ -SAXS/WAXS) experiments during forced silking of *Nephila* spiders[6] provide microstructural information on the nascent silk thread at the exit of the spigots. Information on the fiber-formation process taking place within the spinning duct can, however, not be obtained in this way and the influence of pH[7, 8], ions[9-12] and stress[13] on Fibroin aggregation have only been addressed by in-vitro studies. We also note that several molecular transformations and structural steps (e.g. silk I) have been suggested to be involved in the formation of silk II-type fibers.[3, 5, 14-16] Our aim is to mimic silk protein aggregation in a microfluidic environment and to obtain microstructural information by SR-SAXS/WAXS techniques. Silk producing microfluidic devices made of silicon[17] or PDMS[18] are, however, not optimized for in-situ X-ray scattering studies requiring a high transparency and a low scattering background. A microfluidic cell optimized for X-ray scattering during silk Fibroin aggregation made of glass will be described in the current article.



## II. MATERIALS, METHODS, AND EXPERIMENTAL SETUP

### A. Microfluidic cell

We have chosen a tube-in-tube geometry[19, 20], which allows confining the central Fibroin solution by a surrounding buffer solution and allows an easy extraction of solid material (Fig.1A,B).

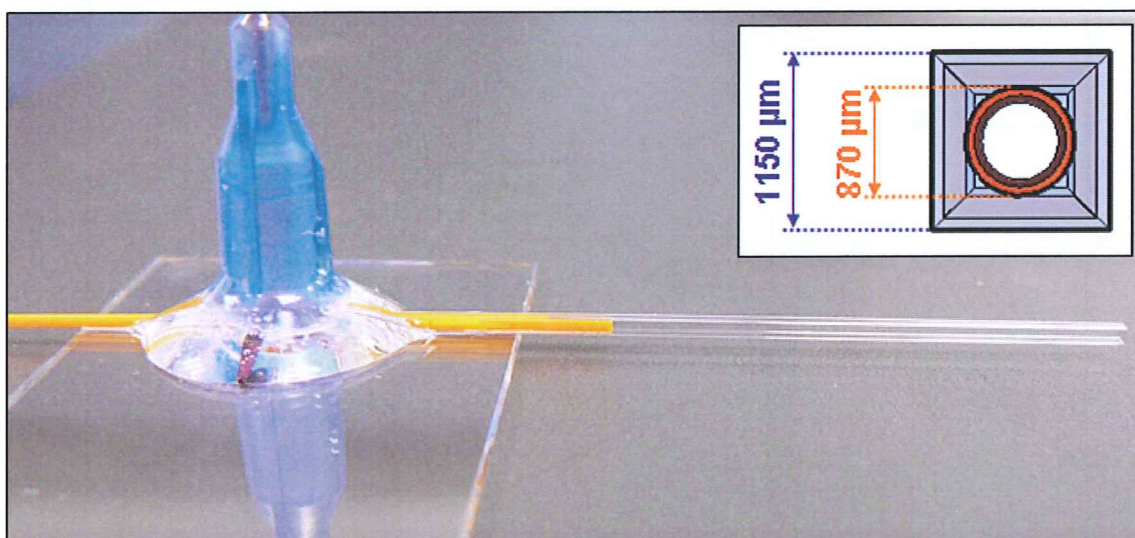


*Fig.1 Schematic design of tube-in-square-pipe microfluidic cell. The insert shows the cross section of the two tubes. Note that the inner capillary fits tightly into the outer square capillary so that it remains centered during operation.*

The inner capillary and the outer capillary of the cell are made of borosilicate glass. The outer capillary is of square section, which allows a constant X-ray path length when scanning laterally across the protein aggregation zone. By reducing the wall thickness of the outer capillary to about 50  $\mu\text{m}$  by etching with hot NaOH solution, the X-ray transmission at 13 keV (0.095 nm) is increased from about 58% to about 87%. The corresponding X-ray transmission of a 1.05 mm thick water layer is about 80%. The inner round capillary fits tightly inside the square capillary so that it stays well centered and the inner flow is surrounded by the outer flow. Another advantage of this geometry is that a symmetric flow profile is maintained around the Fibroin stream, which does not interact with the walls of the tube. This is not the case of the laminar streams obtained using the hydrodynamic focusing geometry in planar microfluidic devices, in which velocity profiles vanishes at the walls.[21, 22] Such geometries are therefore more prone to protein aggregation at the walls and may require appropriate surface films for protection.[18] A concentric mixing geometry is also closer to the geometry of the silk spinning duct[1] as compared to the geometry of planar



microfluidic devices. The capillaries are connected to motorized *Harvard Apparatus* syringe pumps by FEP tubing. (Fig.1B) The syringe pumps are controlled via a PC through an RS232 interface by a home-made control program. The fibrous material is spun from the exit of the capillary into a water bath. The set-up used for SR-experiments is shown schematically in Fig.2.

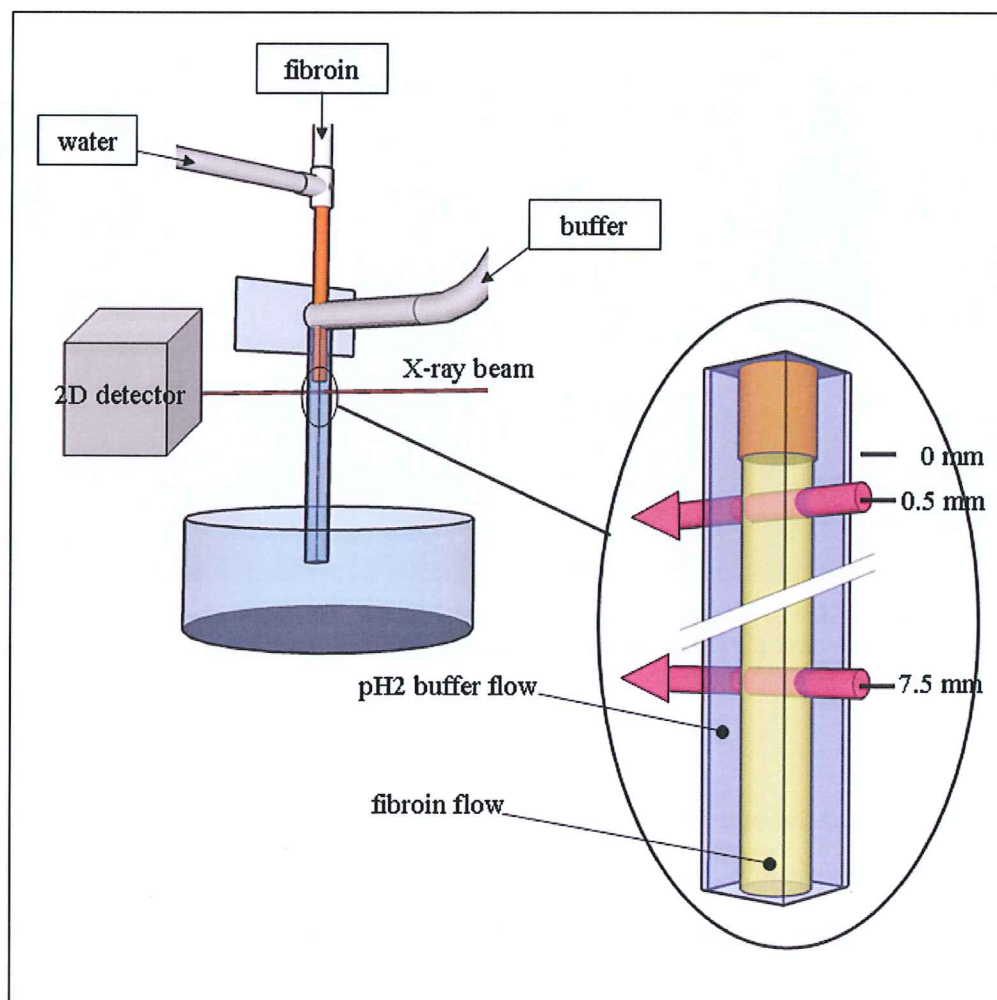


**Fig2:** Schematic setup of microfluidic cell used for synchrotron radiation scattering experiments. The insert shows a zoom of the mixing zone and the positions (mm from inner capillary exit) probed by the beam.

## B. Materials

Fresh *Bombyx mori* cocoons were provided by Stazione Sperimentale per la Seta, Milano. The cocoons were softened in an ice/water mixture for 16 hours and then degummed in 0.1%  $\text{Na}_2\text{CO}_3$  at 80 °C for 5 min. The resulting fibrous material was washed in distilled water and dried in air. The dry material was then dissolved in saturated LiSCN at 60 °C for 3 min and centrifuged for 20 min at 4 °C and  $5 \cdot 10^4$  g to remove the non-dissolved residues. The Fibroin solution was obtained by dialysis against  $\text{H}_2\text{O}$  and characterized by dynamic light

scattering (DLS) and spectrophotometry. The Fibroin concentrations used for the SR-experiments were 5-9 mg/ml. In order to induce protein aggregation analogue to the acidification conditions in the spinning duct[7, 8], a  $\text{H}_3\text{PO}_4$  20mM, NaCl 100 mM pH 2 buffer was used.

### C. Synchrotron radiation experiments

SR-SAXS experiments on Fibroin solutions were performed at the ID02 beamline of the European Synchrotron radiation Facility (ESRF).[23] This beamline is optimized for solution small angle scattering experiments. A combination of three sample-to-detector distances (1500, 3000 and 5000 mm) provided a Q-range  $\approx 2 \times 10^{-2} \text{ nm}^{-1} < Q < 4 \text{ nm}^{-1}$ , using a wavelength ( $\lambda$ ) of 0.1 nm. ( $Q=4\pi\sin\theta\lambda^{-1}$ ,  $\theta$  being  $\frac{1}{2}$  of the scattering angle) The SAXS detector was a fiber-optics coupled CCD (FReLoN)[24]. The incident and transmitted intensities were also simultaneously recorded. The Fibroin solution was measured prior to aggregation using a temperature-controlled flow-through capillary (diameter  $\approx 2$  mm), allowing sample and solvent scattering to be measured in exactly the same conditions. The 2D SAXS patterns were normalized to an absolute scale using water standard and azimuthally averaged to obtain the differential scattering cross section per unit volume,  $I(Q)$ . 100 patterns were taken during mixing of water in pH 2 buffer and averaged. The averaged pattern was subtracted from the Fibroin data as a background.

The aggregation process was studied at a fixed sample-to-detector distance of 3000 mm. The size of the beam was  $150 \times 100 \mu\text{m}^2$ . The Fibroin solution (9 mg/ml) was injected into the inner tube and the pH 2 buffer into the outer tube. (Fig.2) SAXS patterns were collected during mixing of Fibroin with the buffer at a distance of 0.5 mm and 7.5 mm from the inner capillary exit. Prior to mixing, a flow of buffer (0.66 ml/h corresponding to 0.36 mm/sec) and water (0.5 ml/h corresponding to 0.36 mm/sec) was maintained. The flow of water was stopped at a given time and replaced by a flow of Fibroin solution (0.5 ml/h). The flow-speed at the mixing point was 0.29 mm/sec. These flow rates have been chosen to minimize the risk of aggregation as Fibroin and buffer arrive at the mixing point with the same velocity. Therefore, the protein flow is not constricted by the surrounding buffer flow, as depicted by Figure 2. SAXS patterns were recorded at selected positions after the mixing point. Patterns of pure water and buffer solution collected prior to the onset of Fibroin flow were taken as background. Note that the scattering function thus obtained does not correspond to an absolute intensity scale.

The formation of crystalline  $\beta$ -sheet material was detected in the air-dried fiber by  $\mu$ -WAXS using an about  $1 \times 1 \mu\text{m}^2$  beam with  $\lambda=0.096$  nm at the ESRF-ID13 beamline. Further details of the ID13-setup are reported elsewhere.[25]

### III. RESULTS AND DISCUSSION

#### A. Characterization of Fibroin shape

In order to establish the shape of the unperturbed Fibroin molecule in pure water we determined the radius of gyration ( $R_g$ ) in the Guinier approximation.[26] The absolute scattering function  $-I(Q)-$  of a 5 mg/ml Fibroin solution is shown in Fig.3A. From the Guinier plot (insert) a value of  $R_g=10.8$  nm is extrapolated. The same  $R_g$  value is obtained for a Fibroin concentration of 9.34 mg/ml. DLS data on a 5 mg/ml Fibroin solution shows an apparent hydrodynamic radius of 15.7 nm. This value is in agreement with the  $R_g$  value as it includes the hydration shell.  $R_g$  has previously been determined for aqueous Fibroin solutions extrapolated to infinite dilution as 8.15 nm by laboratory SAXS[27] and as  $6.7 \pm 0.3$  nm from a 5 mg/ml solution by SR-SAXS.[16]  $R_g$  values derived from the present study are considered to be more accurate in view of the point focusing SAXS geometry and the flow-through cell used for measuring all solutions under the same conditions. At very low  $Q$ , the SAXS profile reaches a plateau (in the logarithmic scales representation, figure 3) which attest the absence of aggregates.

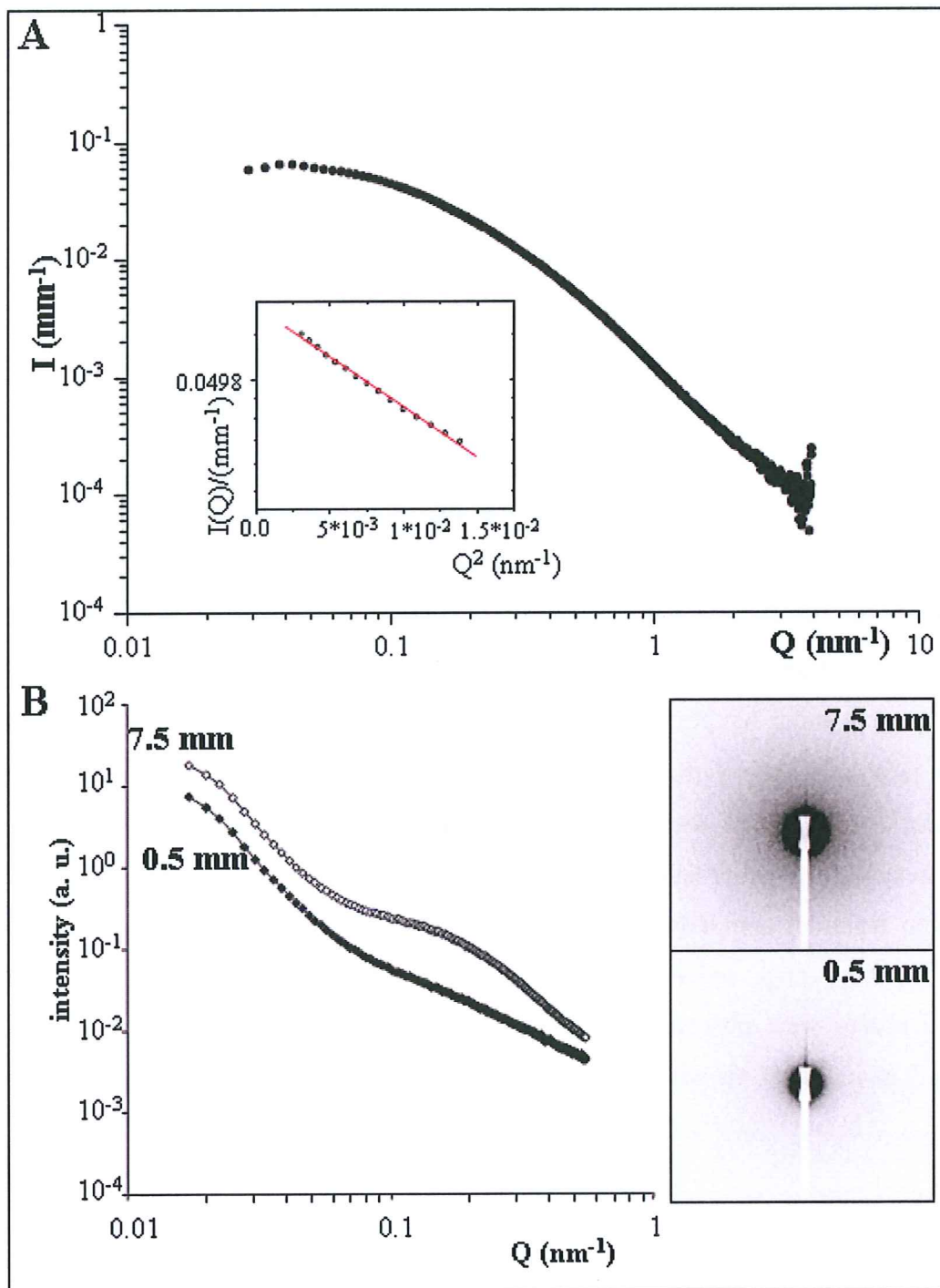


*Fig.3 A: absolute scattering function  $I(Q)$  of Fibroin solution in water (5 mg/ml). The insert shows the Guinier plot with an extrapolated  $R_g$  value of 10.8 nm; B: scattering function for aggregation at 0.5 and 7.5 mm distance from the inner capillary exit. The corresponding 2D SAXS patterns are also shown.*



## B. Protein aggregation and $\beta$ -sheet formation

2D SAXS patterns were obtained at selected positions after the inner tube. The scattering function measured at the positions shown in Fig.2 suggests the presence of an aggregate structure (Fig.3B), which is too large to allow the extrapolation of a radius of gyration as for the unperturbed Fibroin molecule.(Fig.3A) The increase in scattering intensity at low-Q with distance from the exit capillary suggests an increase in aggregate in the probed volume. We also observe a peak at the position of the Fibroin molecule. For the beam position close to the exit capillary (0.5 mm) we assume that scattering function of unperturbed Fibroin overlaps aggregate scattering. As the peak at the Fibroin molecule position becomes, however, more prominent at the larger distance from the exit capillary we assume the formation of an aggregate substructure with similar dimensions as the Fibroin molecule. A more detailed analysis of the scattering function will be presented elsewhere.<sup>[28]</sup> We note that no evidence for the formation of a crystalline  $\beta$ -sheet material from the WAXS-range is obtained at this stage of protein aggregation. However, the aggregated fibrous material can transform, upon room temperature air drying, into a semicrystalline  $\beta$ -sheet type material. Thus the  $\mu$ -WAXS pattern of a typical dried fiber (Fig.4A) shows *Bombyx mori* type silk II reflections<sup>[29]</sup> with a weak texture of the overlapping equatorial 020/210 reflections and an important short-range order halo. (Fig.4B) The azimuthally integrated pattern can be fitted by 3 Gaussian functions simulating the strongest equatorial Bragg peaks and a broad Gaussian due to the short-range order contribution. (Fig.4C) We note that intermediate hydrated structural phases were observed for aggregated Fibroin obtained by shearing in a Couette cell.[16] A similar analysis will be performed in the future on the fiber obtained in the present study.

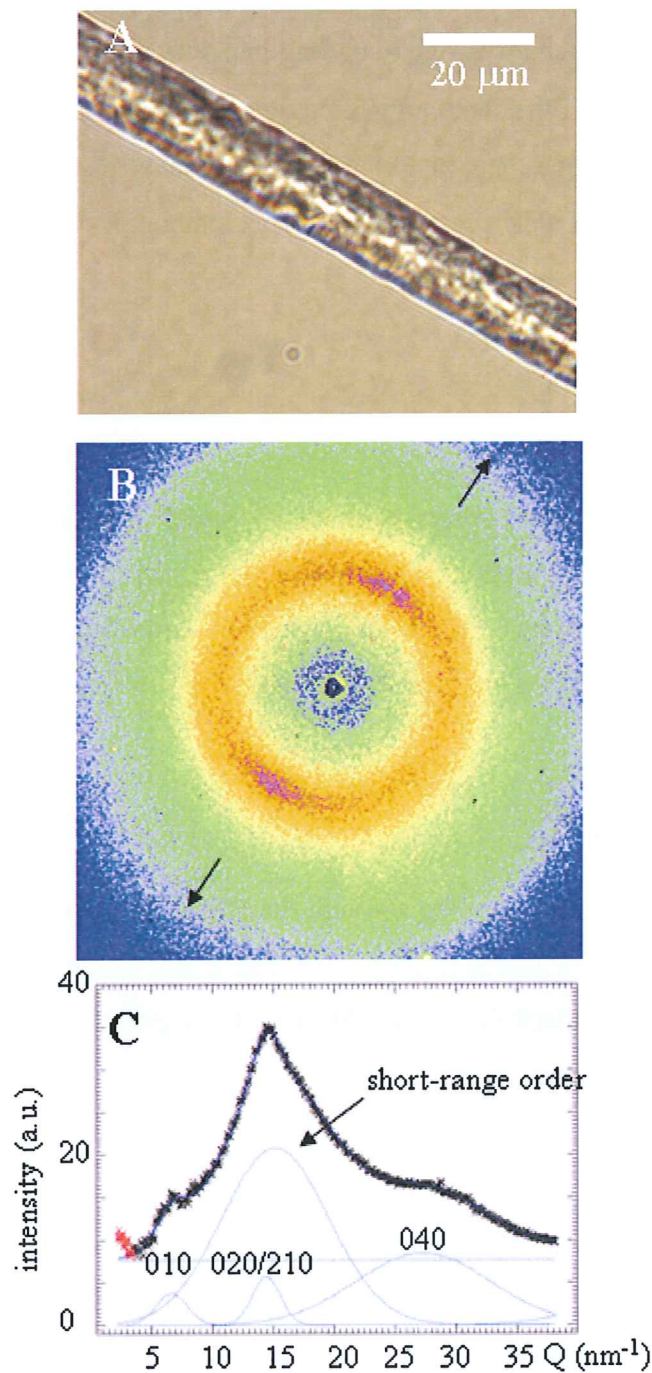


**Fig.4** A: microscope image of artificial silk; B:  $\mu$ -WAXS pattern of artificial silk. The orientation of the equator is indicated by arrows; C: azimuthally averaged equatorial pattern fitted by three narrow Gaussians for the Bragg peaks, a broad Gaussian for the short-range order and a zero-order polynomial. Miller's indices of the Bragg peaks are indicated. The data reduction was performed using the FIT2D software package.

The formation of large aggregate structure prior to  $\beta$ -sheet formation resembles a proposed mechanistic model suggesting the formation of 100-200 nm Fibroin micelles preceding the appearance of fibrillar structures due to shearing.[5] An aggregation step is also observed upon shearing of an aqueous Fibroin solution in a Couette cell.[16] The flaky

aggregate has  $\beta$ -bonding character according to FTIR spectroscopy[16], which supports the assumption of shearing-induced hydrogen-bonding interactions and fibrillation in the micellar model.[5] The conversion of the flaky aggregate to  $\beta$ -sheet material requires a further drying step[16] as for the present aggregate material. Therefore, these results do not support a direct conversion of random coil silk protein into  $\beta$ -sheet material via a nucleation-dependent aggregation mechanism.[4]

## IV. CONCLUSIONS

Fibroin aggregation has been observed in-situ by SAXS using a tube-in-tube microfluidic cell. The aggregate material suggests the presence of a large structure with a substructure retaining the size of the original Fibroin molecule. The microfluidic setup and experimental techniques could be applied to other protein aggregation or conformation studies.

## ACKNOWLEDGMENTS

ESRF gratefully acknowledges funding through the EEC FP6 project SAXIER. Microfluidic devices and applications are developed by LOF and ESRF in the context of the long-term project SC-2267. We also thank G. Freddi (Milano) for a gift of cocoons and M. Sztucki for his help in SAXS data analysis.



---

## References

1. Vollrath, F. and D.P. Knight, *Liquid crystalline spinning of spider silk*. Nature, 2001. **410**: p. 541-548.
2. Asakura, T., et al., *Some Observations on the Structure and Function of the Spinning Apparatus in the Silkworm Bombyx mori*. Biomacromolecules, 2006. **8**(1): p. 175-181.
3. Magoshi, J., Y. Magoshi, and S. Nakamura, *Mechanism of fiber formation of silkworm*, in *Silk Polymers. Materials Science and Biotechnology*, D. Kaplan, et al., Editors. 1994, American Chemical Society: Washington. p. 292-310.
4. Li, G., et al., *The natural silk spinning process: a nucleation-dependent aggregation mechanism?* Eur. J. Biochem., 2001. **268**: p. 6600-6606.
5. Jin, H.J. and D.L. Kaplan, *Mechanism of silk processing in insects and spiders*. Nature, 2003. **424**: p. 1057 - 1061.
6. Riekel, C. and F. Vollrath, *Spider silk fibre extrusion: combined wide- and small-angle X-ray microdiffraction experiments*. Int. J. Biol. Macrom., 2001. **29**(3): p. 203-210.
7. Vollrath, F., D.P. Knight, and X.W. Hu, *Silk production in spider involves acid bath treatment*. The Royal Society, 1998. **265**: p. 817-820.
8. Terry, A.E., et al., *pH Induced Changes in the Rheology of Silk Fibroin Solution from the Middle Division of Bombyx Mori Silkworm*. Biomacromolecules, 2004. **5**: p. 768-772.
9. Chen, X., et al., *Conformation Transition in Silk Protein Films Monitored by Time-Resolved Fourier Transform Infrared Spectroscopy: Effect of Potassium Ions on Nephila Spidroin Films*. Biochem., 2002. **41**: p. 14944-14950.
10. Peng, X., et al., *Further Investigation on Potassium-Induced Conformation Transition on Nephila Spidroin Film with Two-Dimensional Infrared Correlation Spectroscopy*. Biomacromolecules, 2005. **6**(302-308).
11. Zong, X.H., et al., *Effect of pH and Copper(II) on the Conformation Transitions of Silk Fibroin Based on EPR, NMR, and Raman Spectroscopy*. Biochemistry, 2004. **43**: p. 11932-11941.
12. Iizuka, E., *Silk Thread, Mechanism of Spinning and its Mechanical Properties*. 1985. **41**: p. 173-185.
13. Knight, D., M. Knight, and F. Vollrath, *Beta transition and stress-induced phase separation in the spinning of spider dragline silk*. Int. J. Biol. Macrom., 2000. **27**(3): p. 205-210.
14. Magoshi, J., Y. Magoshi, and S. Nakamura, *Crystallization, liquid crystal, and fiber formation of silk fibroin*. J. Appl. Polym. Sci., 1985. **41**: p. 187-204.
15. Viney, C., *Natural silks: archetypal supramolecular assembly of polymer fibres*. Supramolecular science, 1997. **4**: p. 75-81.
16. Roessle, M., et al., *Structural evolution of regenerated silk fibroin under shear: combined wide- and small-angle X-ray scattering experiments using synchrotron radiation*. Biopolymers, 2004. **74**: p. 316-327.
17. Liivak, O., et al., *A Microfabricated Wet-Spinning Apparatus To Spin Fibers of Silk Proteins. Structure-Property Correlations*. Macromolecules, 1998. **31**: p. 2947-2951.
18. Scheibel, T., et al., *Microfluidic Device for Controlled Aggregation of Spider Silk*. 2007, Technische Universitaet Muenchen: Germany.



19. Utada, A.S., et al., *Monodisperse Double Emulsions Generated from a Microcapillary Device*. *Science*, 2005. **308**(537-541).
20. Destremaut, F., et al., *Microfluidique et diffusion de rayons X aux petits angles : des outils pour étudier les processus sol-gel*. *La houille blanche : revue internationale de l'eau*, 2007. **6**: p. 26-33.
21. Knight, J.B., et al., *Hydrodynamic Focusing on a Silicon Chip: Mixing Nanoliters in Microseconds*. *PRL*, 1998. **80**(17): p. 3863-3866.
22. Pfohl, T., et al., *Trends in microfluidics with complex fluids*. *Chem. Phys. Chem.*, 2003. **4**(12): p. 1291-1298.
23. Panine, P., M. Gradzielski, and T. Narayanan, *Combined rheometry and small-angle x-ray scattering*. *Review of Scientific Instruments*, 2003. **74**(4): p. 2451-2455.
24. Labiche, J.C., et al., *The fast readout low noise camera as a versatile x-ray detector for time resolved dispersive extended x-ray absorption fine structure and diffraction studies of dynamic problems in materials science, chemistry, and catalysis*. *Rev. Scient. Instrum.*, 2007. **78**: p. 091301-1 - 091301-11.
25. Gebhardt, R., et al., *High-Pressure Potato Starch Granule Gelatinization: Synchrotron Radiation Micro-SAXS/WAXS Using a Diamond Anvil Cell*. *Biomacromolecules*, 2007. **8**(7): p. 2092 -2097.
26. Guinier, A. and G. Fournet, *Small-Angle Scattering of X-Rays*. 1955, New York: J. Wiley and Sons.
27. Canetti, M., et al., *CD and Small-Angle X-Ray Scattering of Silk Fibroin Solutions*. *Biopolymers*, 1989. **28**: p. 1613-1624.
28. Martel, A. and et al., in preparation.
29. Martel, A., et al., *Thermal degradation of Bombyx mori silk: evolution of molecular structure, crystalline parameters and mechanical properties*. *Biomacromolecules*, 2007. **8**(11): p. 3548 -3556.

# APPENDIX V

## SDS-PAGE Solutions

### Sample buffer

- 0.025 % coomassie blue
- 10 % v/v Methanol
- 7.5% v/v Acetic Acid
- 1.25 % v/v  $\beta$ -mercapto-ethanol

### 5% Stacking gel

- 17% v/v Acrylamide : Bis-acrylamide (37.5 : 1) solution (5% final)
- 13% v/v Tris 1 M, pH 6.8 solution (130 mM final)
- 1% v/v SDS 10% w/v solution (3.5 mM final)
- 1% v/v Ammonium persulfate 10% w/v solution (4,4 mM final)
- 0.1% TEMED (N, N, N', N' Tetramethylethylenediamine) (8.6 mM final)

### 12 % Separation gel

- 40% v/v Acrylamide : Bis-acrylamide (37.5 : 1) solution (12% final)
- 25% v/v Tris 1.5 M, pH 8.8 solution (375 mM final)
- 1% v/v SDS 10% w/v solution (3.5 mM final)
- 1% v/v Ammonium persulfate 10% w/v solution (4,4 mM final)
- 0.04% TEMED (3.4 mM final)

### Staining solution

- 0.25 % coomassie blue
- 45 % v/v Ethanol
- 10% v/v Acetic Acid

### Destaining solution

- 5 % v/v Ethanol
- 15% v/v Acetic Acid



## APPENDIX VI

### Thermal Behavior of *Bombyx mori* Silk: Evolution of Crystalline Parameters, Molecular Structure, and Mechanical Properties

**A. Martel, M. Burghammer, R. J. Davies, and C. Riekell**

European Synchrotron Radiation Facility, B.P. 220, F-38043 Grenoble Cedex, France

The thermal behavior up to degradation of *Bombyx mori* silk has been studied by scanning synchrotron radiation microdiffraction, gel electrophoresis, and mechanical testing. The diffraction patterns from single baves can be separated into scattering from anisotropic crystalline  $\beta$ -sheet domains and random short-range order. In contrast to dragline silk, scattering from oriented, short-range-order Fibroin is not observed. The sheath of sericin proteins can be selectively probed by a microbeam and shows also principally random short-range-order domains with a small crystalline  $\beta$ -sheet fraction. Microdiffraction experiments on single baves from 100 to 573 K show an increase in lattice expansion along the [010] chain-stacking direction above 200-250 K, which could be due to an increase in side-chain mobility. Degradation of the crystalline fraction commences at approximately 500 K, and the fibers have become amorphous at about 570 K with an onset of carbonization. Gel electrophoresis shows that the degradation of FibH molecules starts already at about 350 K, while FibL molecules start degrading at about 400 K. The mechanical properties of single baves such as strain-to-failure and tensile strength also start degrading at about 400 K, while the initial modulus increases up to about 475 K. It is proposed that this is due to the development of cross-linking in the short-range-order chain fraction.



## I- INTRODUCTION

The aim of the current work is to determine the thermal behavior of *B. mori* silk up to degradation and to correlate microstructural parameters with macroscopic mechanical behavior. A thermal degradation study has recently been performed for dragline silk showing a surprisingly high structural stability of  $\beta$ -sheet domains.[1] X-ray structural studies are, however, limited by the semicrystalline nature of silk fibers to the determination of lattice parameters, low-resolution structural modeling, orientation or nanofibrillar morphology.[1, 4-7] Molecular models for the macroscopic mechanical behavior of silks use on the other hand concepts such as a network of flexible, hydrogen-bonded chains reinforced by crystalline domains[8], which is only partially accessible to X-ray diffraction analysis. The article will therefore develop in addition to a crystallographic analysis, methods of separating the short-range order scattering due to the random chain fraction from the Bragg reflections, using a concept introduced for dragline silk.[6] This will be complimented by a protein analysis on the thermal stability of silk Fibroin. Structural studies will be performed by state-of-the art synchrotron radiation (SR) microdiffraction, which allows maximizing the Fibroin contribution (see below). The article will introduce several technical advances such as scanning microdiffraction during in-situ heating experiments of single brins and baves, the separation of sericin from Fibroin scattering at the edge of a bave and the recursive separation of crystalline and short-range order peaks in the diffraction patterns.

## II- MATERIALS AND METHODS

### A- Samples

Fresh *Bombyx mori* cocoons were provided by INRA, Unité Séricicole, Lyon, France and were used as received. SR microdiffraction experiments were performed on single baves (composed of two brins with sericin coating) in order to maximize Fibroin scattering. Such experiments require a high brilliance synchrotron radiation source[6, 9] while experiments with laboratory X-ray sources are limited to fiber bundles.[10, 11] The baves were separated from the cocoons with microscissors. Care was taken not to introduce mechanical strain. A scanning electron microscopy (SEM) image of two brins enveloped partially by a sericin layer is shown in Figure 1A. The cross-section of a bave -produced by laser microdissection- is shown in Figure 1B. Degummed *B. mori* silk was provided by the Stazione Sperimentale per la Seta, Milano.[12] *Greige* silk fibers were provided by Le Musée de la Soie, St Hippolyte du

Fort, France. The sericin layer has been softened and partially removed by boiling the silk fibers in a soap solution (Savon de Marseille). (Figure 1C)

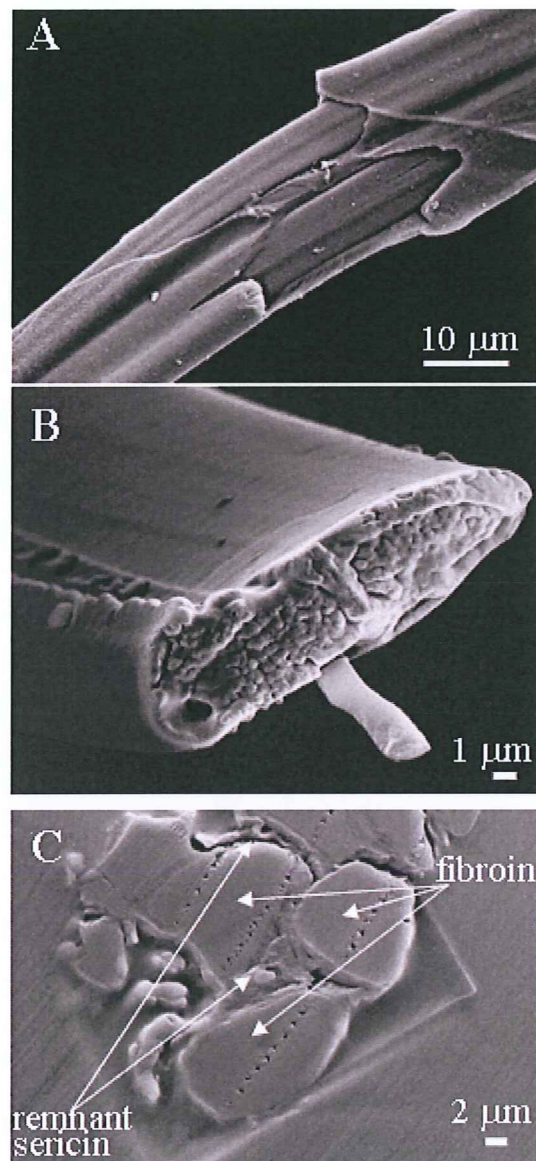


*Figure 1: Scanning electron microscopy (SEM) images (ZEISS-LEO 1530; 10 kV HT) of B. mori silk samples shadowed by a thin gold-layer A: two brins, partially covered by an about 2 μm thick sericin layer; B: section of bave cut by a Zeiss/P.A.L.M. microdissection system. The surface cross section is 175 μm<sup>2</sup> taking a fiber tilt angle of 45° into account; C: Greige silk containing residual sericin. The sample has been embedded in polymerized (2-hydroxyethyl)-methacrylate resin and cut by an ultramicrotome.*

## B- Heating conditions

Two kinds of heat treatment have been applied, which allow both reversible and irreversible temperature effects to be observed. For *in-situ* synchrotron radiation diffraction experiments under anaerobic conditions, the bave temperature was controlled in the range  $100 < T \text{ (K)} < 500$  by an Oxford Cryosystems Cryostream 700 system with 5 liters/min nitrogen flow. The distance of the bave from the nozzle was about 10 mm. The nitrogen gas temperature at the sample position is within 1 K of the cryoflow set-temperature for a range of  $10 \pm 5$  mm.[13] Other baves from a cocoon were initially oven-heated before their characterization by electrophoresis, synchrotron radiation diffraction and mechanical tests. Heating was performed under anaerobic conditions ( $N_2$ ) up to 473 K and in air for higher temperatures. For protein analysis, mechanical tests and complimentary diffraction experiments, baves were pre-heated in an oven for 6 hours either under a nitrogen atmosphere ( $298 < T \text{ (K)} < 473$ ) or in air ( $473 < T \text{ (K)} < 573$ ) and then cooled to room temperature.

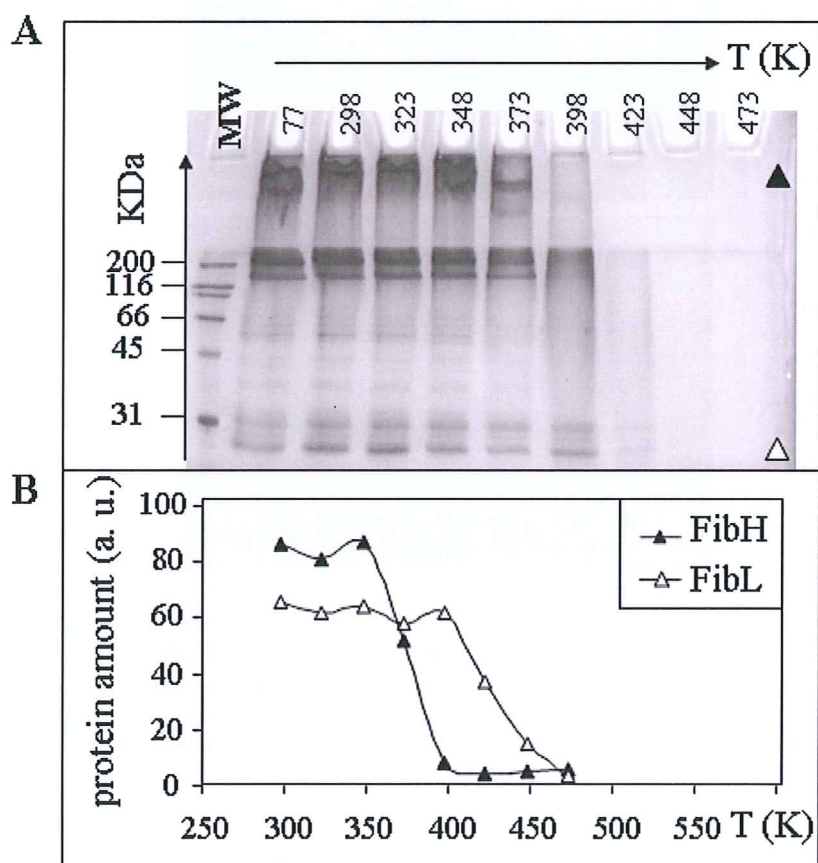


Figure 2: A: protein degradation with the temperature from a denaturing 12% poly-acrylamide gel electrophoresis (SDS-PAGE); B: quantification of data shown in Figure 2A: (MW: molecular weight standard). Black triangles represent FibH, and white triangles, FibL.



### C- Gel electrophoresis

After heating in a nitrogen atmosphere (as described above), 15 mg of cocoons were partially dissolved in 600  $\mu\text{L}$  of saturated LiSCN under shaking at 60 °C for 3 minutes. 3  $\mu\text{L}$  were denatured by boiling 5 min in a 4%  $\beta$ -mercapto-ethanol solution, and loaded on a 12% denaturing acrylamide gel. The migration lasted 90 min at 120 V. After coomassie blue staining, an image of the gel was digitized in order to quantify the relative amount of protein using the Fit2D software.[14] A background line, close to each signal line and having the same size, was subtracted. The results (Figure 2A) are based on the average of 3 similar experiments. The molecular weight standard is the SDS-PAGE standard, broad range, from Biorad. This method reveals the length of the peptides present in the sample, which means, in this case, the integrity of the peptidic chains of FibH and FibL. (Figure 2B)

### D- Mechanical test

Stress/strain curves of single baves were obtained *ex-situ* using a custom-built stretching cell comprising a force sensor and PC-controlled linear translation stage. A 4 mm long bave was fixed within a cardboard window using cyanoacrylate adhesive. This was then secured to the stretching cell's clamps, between the stage and force sensor. The baves were deformed in tension at a constant rate of extension (10  $\mu\text{m/s}$ ) with the force and extension recorded every 0.5 s. The resulting data were then used to calculate fiber stress and strain. For the stress calculation, the cross sectional area including the sericin coating was approximated using a rectangle, an approximation supported by the SEM micrographs shown in Figure 1B. The rectangle's dimensions were determined microscopically using the AnalySIS5<sup>TM</sup> software package (Soft Imaging System GmbH, Germany), and averaged between three fibers for each temperature. The strain-to-failure, tensile strength and Young's modulus, were derived from an average of 9 to 15 stress/strain curves for each temperature. We did not find a significant influence of a shorter gauge length on these mechanical parameters.

### E- Synchrotron radiation scattering

Experiments on single *B. mori* baves and brins were performed at the ESRF-ID13 beamline.<sup>[15]</sup> For the *in-situ* heating experiments a microgoniometer set-up was used.<sup>[16]</sup> The monochromatic synchrotron radiation beam (wavelength:  $\lambda=0.095$  nm; band pass  $\Delta\lambda/\lambda \approx 2 \cdot 10^{-4}$ ) was focused and collimated to 4  $\mu\text{m}$  for the fresh baves and 10  $\mu\text{m}$  for the greige silk by a combination of compound refractive Be-lenses<sup>[17]</sup> and apertures. A single *B. mori* bave



was glued to a thin metal ring, which was attached to a support and aligned in the beam. The temperature of the cryoflow system was ramped in steps of 10 K in the range  $100 < T \text{ (K)} < 500$ . At every temperature plateau, a linear scan across the bave with 5  $\mu\text{m}$  steps was performed. Consecutive linear scans with increasing temperature were performed displaced by a 13  $\mu\text{m}$  step-increment along the bave in order to avoid possible radiation damage by neighboring scans. The same data collection method was applied to the preheated baves at room temperature. The sample was composed in this case of 12 baves heated at 12 temperatures from 298 K to 548 K and glued by both ends on a cardboard, which was fixed to the goniometer support. A further bave -heated at 573 K- was too fragile to be fixed in this way and was therefore glued to the end of a tapered capillary. 7 to 8 linear scans of 4  $\mu\text{m}$  step-increment were performed across each bave, spaced by 20  $\mu\text{m}$  to 100  $\mu\text{m}$  along the bave. Complimentary mesh-scanning experiments on fresh or degummed baves and brins were performed at room temperature using a focused beam of approximately 1  $\mu\text{m}$  fwhm (full-width-half-maximum) from crossed mirrors or 3  $\mu\text{m}$  fwhm from a tapered glass capillary.[15] These beam sizes are too large to resolve banding effects observed in degummed *B. mori* silk by TEM[18] but should be accessible to nanodiffraction SR-experiments.[19, 20] Diffraction patterns were recorded by a slow-scan 16-bit readout MAR CCD-detector. The sample-to-detector distance was calibrated by an  $\text{Al}_2\text{O}_3$  or Ag-behenate powder[21] standard. Care was taken to avoid radiation damage effects by limiting the data collection time to a few seconds/pattern. Initial data reduction and analysis of individual patterns was performed using the FIT2D software package.[14] For recursive data analysis a batch processing software[22] and a specialists software (see supporting information) were used. The instrumental background was corrected by subtracting a pattern recorded just outside a silk fiber during a scan. Sample statistics was improved by averaging several patterns from within the sample and from the background patterns.

### III- RESULTS AND DISCUSSION

#### A- Microdiffraction from single baves and brins

The Fibroin pattern from the centre of a degummed *B. mori* brin obtained at room temperature with a 1  $\mu\text{m}$  fwhm beam shows the Bragg peaks of the silk II structure corresponding to the antipolar-antiparallel  $\beta$ -sheet structure.[10, 23, 24] (Figure 3A) We note that this pattern is typical of all other patterns recorded and that in particular no evidence for a different unit cell or sharper reflections due to larger crystallites, as proposed for dragline silk [25], was obtained. The pattern can be indexed for a monoclinic  $P2_1$  space group with the unit cell [10]:  $a=0.938$  nm,  $b=0.949$  nm,  $c=0.698$  nm (fiber axis);  $\gamma \approx 90^\circ$ . In the following we will limit the discussion to the 010, 020, 210, 030 equatorial reflections, which are the only ones observed in diffraction experiments on doubly oriented samples.[10]

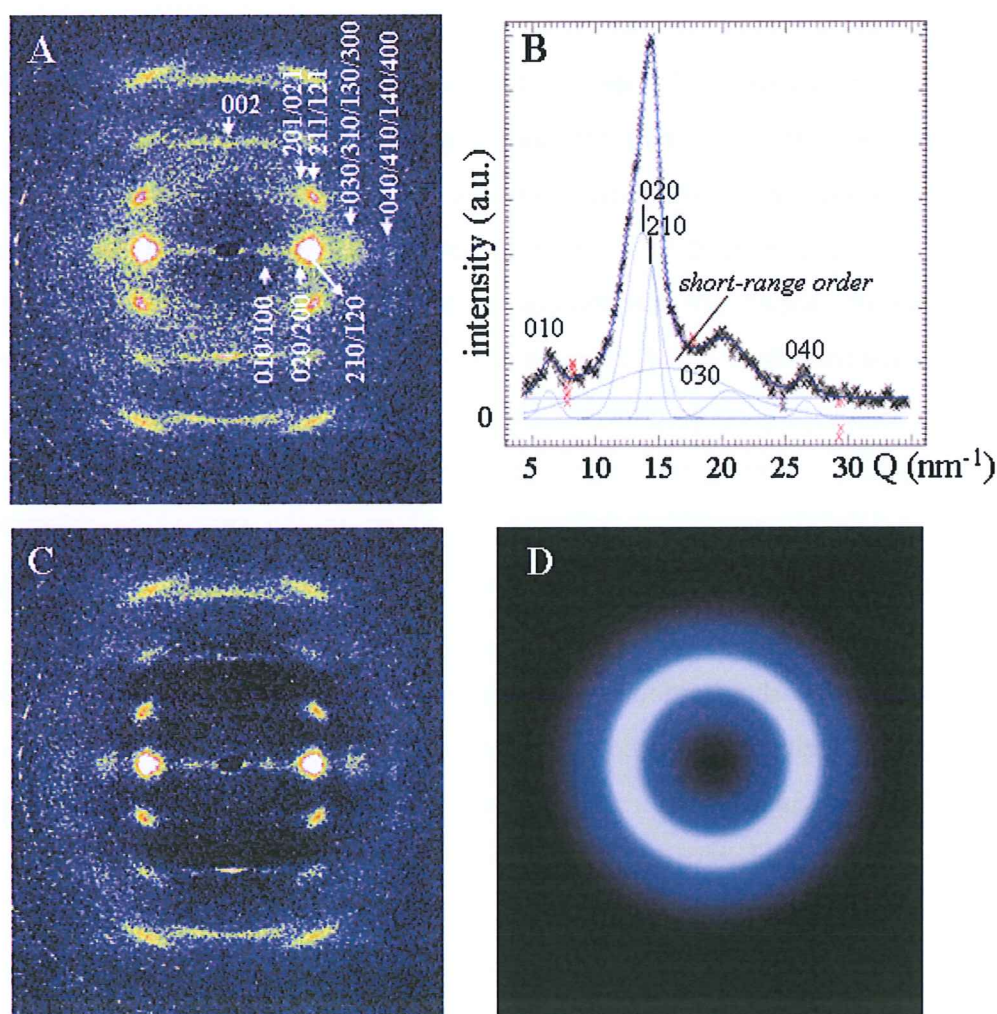


**Figure 3:** A: degummed *B. mori* pattern with Miller's indices for the strongest Bragg peaks. Overlapping reflections are indicated with the most intense equatorial reflections in bold (see text); B: azimuthally integrated equatorial pattern (crosses) fitted by 4 narrow Gaussian profiles for the most intense Bragg peaks, a broad Gaussian profile for the short-range order halo and a 0-order polynomial (blue lines); C: degummed *B. mori* pattern after subtraction of the amorphous halo; D: simulated short-range order halo (same intensity scale for all patterns; the "red" data points were masked during refinement)



One of the aims of the present paper is to determine the evolution of the crystalline and amorphous Fibroin fractions with temperature. A quantitative determination of the crystallinity can be performed for two-phase polymers of known composition based on global fit to a 1D-profile.[26] This approach is, however, not adapted to multiple pattern analysis and for the *B. mori* samples where the amino acid composition of amorphous and crystalline fractions is not well defined. The approach taken in this work is to separate Bragg peaks and short-range order scattering by a recursive fit of Gaussian functions, which provides information on the profile parameters peak position, peak width and integrated peak intensity but neglects the contribution of incoherent scattering. The sum of the Bragg peak intensities ( $\sum I_{Bragg}$ ) will be assumed to be proportional to the crystalline fraction.

For the model of a flexible protein chain matrix, reinforced by crystalline  $\beta$ -sheet domains[8], one expects a diffuse powder ring due to short-range order and Bragg peaks. This holds also for short-segment nanofibrils[7] as reinforcing elements. The expected diffuse ring is observed for dragline silk[4, 27] and also for the *B. mori* pattern. (Figure 3A) The short-range order peak is related to chain-chain correlation constrained by inter-chain hydrogen bonding, which may explain that the short-range order peak position is close to the  $\beta$ -sheet 210 peak position. We note that the short-range order peak position changes at higher temperatures as the hydrogen-bonding network breaks down. (see below) The short-range order peak can be enhanced in *B. mori* by graft-copolymerization of molecules such as methylacrylamide, which are incorporated into the random chain fraction.[12] We have therefore chosen to include the short-range order peak in the peak profile fitting procedure, in contrast to a recent study on dragline silk.[1]

The quality of this approach will be shown below for a single pattern while details of the specialists' batch processing software are given in the supporting information. The equatorial intensity distribution is first azimuthally integrated over an angular range of  $\approx 4^\circ$ , which covers completely the equatorial reflections and a segment of the diffuse ring. The resulting 1D-intensity distribution is fitted by Gaussian profiles for the Bragg peaks and the diffuse peak as well as a 0-order polynomial background for the residual background scattering from the sample. (Figure 3B) The use of a homogeneous 210-reflection profile[28] does not result in a stable profile fit to the asymmetric 200/210 intensity profile including the short-range order background.

The apparent particle size ( $L$ ) determined by Scherrer's equation[6, 29] for the 020 reflection ( $L=1.8$  nm) and the  $\beta$ -sheet 210 reflection ( $L=4.2$  nm) show an increased coherence

length along the hydrogen-bonded [210] direction as compared to the  $\beta$ -sheet stacking [010] direction, which is also the case for single dragline silk fibers analyzed according to the same protocol.[6] The L-values for *B. mori* (this work) and for *Nephila dragline silk*[6, 27] fit well with molecular modeling predictions for a flexible network reinforced by nanocrystalline domains.[8] It is interesting to compare these particle size values with other values from literature. X-ray microdiffraction results on *Nephila* dragline silk neglecting the short-range order scattering suggest values of  $L \approx 5$  nm at room temperature for both the [010] and [210] directions.[1] (note the exchange of a/b in Ref.[1] as compared to the present axis choice for *Nephila*[6]) TEM dark field (DF) images based on the 020 reflection reveal significantly larger lateral sizes of  $\beta$ -sheet crystallites of about 10 nm.[18] It cannot, however, be excluded that TEM sample preparation (embedding, sectioning) and/or sample exposure to vacuum (dehydration) induces lateral aggregation across the [010]  $\beta$ -sheet stacking direction via van der Waals forces. It has already been noted that L-values determined from dry *Nephila* silk fibers[4] by X-ray diffraction are systematically larger than L-values determined during in-situ extrusion.[27] We tentatively assume that the nanocrystalline Fibroin domains can assemble axially through a short-range order interface into nanofibrils but lack the driving force for lateral aggregation, presumably due to a hydration of the nanofibrillar surface. We note in this respect the formation of the *B. mori* silk structure from regenerated sheared Fibroin solution through at least one intermediary hydrated phase.[30] Dehydration could therefore result in a further lateral aggregation through van der Waals forces. This scheme is speculative at present but could be tested by systematic aggregation studies.

The axial sizes of  $\beta$ -sheet crystallites in *B. mori* observed by TEM DF images show a large spread from about 20 to 160 nm.[18] The deduction of rodlike aggregates with axial dimensions of about 170 nm for *Nephila* dragline silk from SANS data[7] suggest that the axial dimensions of *B. mori* crystallites derived by TEM DF[18] are not affected by aggregation.

The diffuse peak ( $d \approx 0.41$  nm) is attributed to randomly distributed, short-range order domains. The 1D Gaussian profile parameters of the short-range order peak in Figure 3B allow generating a 2D Gaussian profile. (Figure 3D) The subtraction of this profile from the *B. mori* pattern provides a pattern, which is a good approximation to a completely crystalline pattern. The intensity of the short-range order peak (Figure 3D) corresponds to 44% of the total integrated intensity of the raw *B. mori* pattern (Figure 3A), which implies an integrated intensity value of  $\approx 56\%$  for the Bragg peaks. We note that the value of  $\approx 56\%$  -as other values



reported in literature based on more or less extensive peak separation procedures[11, 31-35]-do not correspond to an exact determination of crystallinity.

It is also interesting to verify the presence of axially-oriented, short-range order domains, which have been proposed connecting the crystalline domains of the nanofibrils in *Nephila* dragline silk.[4-7] The analysis was performed for the cake-regrouped pattern (transformation of radial and azimuthal scales into orthogonal scales) *B. mori* pattern covering the strongest equatorial and 1<sup>st</sup> layer-line reflections. (Figure 4A) The pattern can be fitted by four 2D Gaussian profiles for the Bragg peaks and a Gaussian profile for the equatorial diffuse scattering extending from the position of the equatorial peaks to smaller Q-values. (Figure 4B) No evidence for additional short-range order scattering at the position of the 210 reflection is, however, observed in contrast to the 210 reflection of a *Nephila* silk fiber.[6] (see remark on unit cell choice above) We attribute this to a lower volume fraction of short-range order domains in *B. mori* as compared to dragline silk[27], presumably due to its higher crystallinity.[4] This implies in the frame of the nanofibrillar model[7] longer crystalline domains and shorter short-range order interface domains, which agrees to SAXS analysis of *B. mori* silk[36] and SAXS/WAXS data of dragline silk (see discussion particle size values above and Ref [27]).

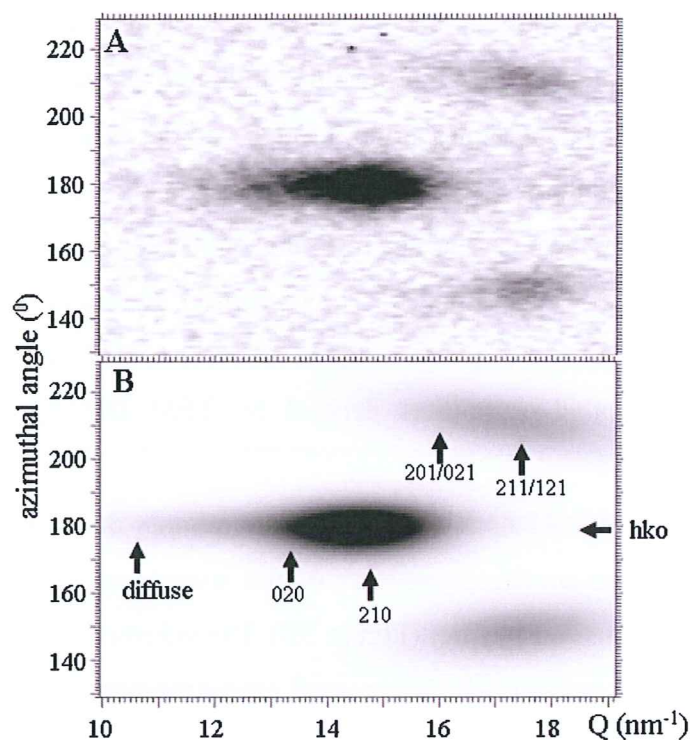


**Figure 4:** A: cake regrouped degummed *B. mori* pattern covering the range of the strongest equatorial and 1<sup>st</sup> layer line reflections; B: simulated cake regrouped pattern fitted by four 2D-Gaussian profiles for 020; 210 and 201/021+211/121-reflections. An equatorial Gaussian profile extending towards the 010 position simulates residual diffuse scattering. (same intensity scale for both patterns)

The pattern from a *B. mori* cocoon bave contains in addition scattering from sericin. The sericin volume fraction dominates the pattern obtained with a  $1 \times 1 \mu\text{m}^2$  fwhm beam at the edge of a bave. (Figure 5A). The azimuthally averaged pattern can be fitted by two broad Gaussian profiles ( $d_1=0.391 \text{ nm}$ ;  $d_2=0.223 \text{ nm}$ ). The interpretation as short-range order sericin scattering is corroborated by the fact that no evidence for such peaks has been obtained with a similar experiment on a degummed *B. mori* brin (not shown). A weak Gaussian profile at the position of the Fibroin 020/210 peaks could be due to a small crystalline  $\beta$ -sheet fraction in sericin but a small fraction of Fibroin chains cannot be excluded. (Figure 5B) It is, however, interesting to note that highly crystalline  $\beta$ -sheet material can be obtained by drying concentrated sericin-solutions[37]. In addition, the high  $\beta$ -sheet content of recombinant sericin-like protein has been attributed to a long-range ordered material.[38] This suggests that sericin might become amenable to single crystal structure analysis by optimizing the crystallization conditions.

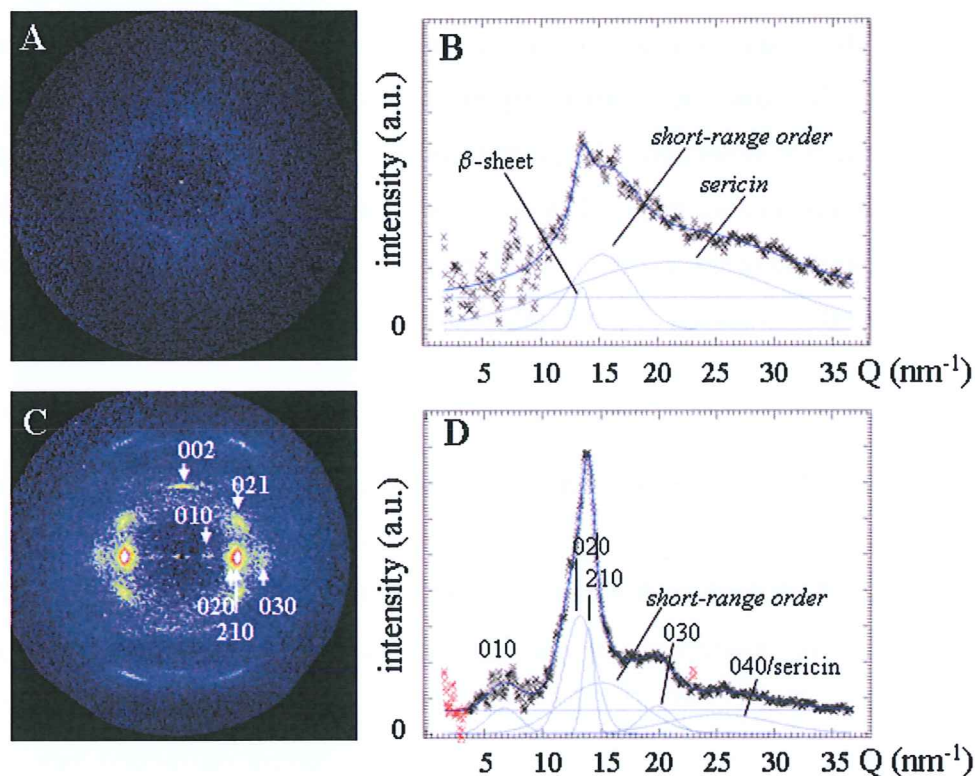


**Figure 5:** *A: Bombyx mori* pattern from very edge of bave; *B: 360<sup>o</sup>* azimuthal average of Figure 5A. The pattern is fitted by a narrow Gaussian for the residual Bragg scattering, 2 broad Gaussians for the sericin short-range order halo and a 0-order polynomial for the random background; *C: pattern from center of one of the two brins in the bave*; *D: azimuthal average across the equatorial peaks. The pattern is fitted by narrow Gaussians for the Bragg peaks, broad Gaussians for the short-range order scattering and a 0-order polynomial for the random background. (the “red” data points were masked during refinement)*



The pattern from the center of the bave (Figure 5C) will be dominated by Fibroin scattering as the volume fraction of sericin in the microbeam gauge volume is only a few percent. The crystalline Fibroin fraction will at any rate not be affected by the sericin scattering, which will contribute principally to the short-range order peak. The 1D profile was fitted by 4 Gaussian profiles for the Bragg peaks, two broad peaks and a 0-order polynomial background. (Figure 5D) The broad peak at  $Q \approx 15 \text{ nm}^{-1}$  corresponds to the sum of Fibroin and (weak) sericin short-range order scattering. The second sericin peak in Fig.5.B overlaps with other diffuse and crystalline Fibroin scattering contributions including the 040 Bragg peak.

Evolution of peak positions. The evolution of the peak positions of the strongest equatorial reflections during *in situ* heating experiment is shown in Figures 6A,B. The data obtained for the *Greige* silk (Figure 6A) suggest that the lattice expansion follows two phases: a linear expansion phase up to 200-250 K, and an enhanced linear expansion phase at higher temperatures. In this second phase, the thermal expansions derived from linear least-squares fits are  $1 \cdot 10^{-3} \text{ nm/K}$  (210 reflection) and  $1.8 \cdot 10^{-3} \text{ nm/K}$  (020 reflection). This implies a lower thermal expansion along the [210] direction -which is closer to the pleated-sheet [100] direction- than to the chain-stacking [010] direction. In view of the overlap of 200 and 210 reflections, we verified that the thermal expansion derived from the 030 reflection was comparable with the 020 reflection. The position of the *B. mori* 002 reflection is practically constant across the temperature range (data not shown), which suggests that the peptide chain expansion coefficient along the c-axis expansion is significantly below the [210] and [010] expansion coefficients. Although less smooth due to a poorer statistics, the results for fresh silk expansion seem to follow the same scheme. (Figure 6B)

The origin of the onset of the enhanced thermal expansion into the [010] direction is not clear at present but could be due to an increasing side-chain mobility (e.g. onset of  $\text{CH}_3$  rotation) modifying the interchain distance. An onset of molecular mobility at about 200K has also been observed for dragline spider silk by inelastic neutron scattering[7] and dynamic mechanical analysis (DMA).[39] The neutron scattering data are, however, mainly due to water mobility in the amorphous chain fraction while the current diffraction data reflect the crystalline fraction.

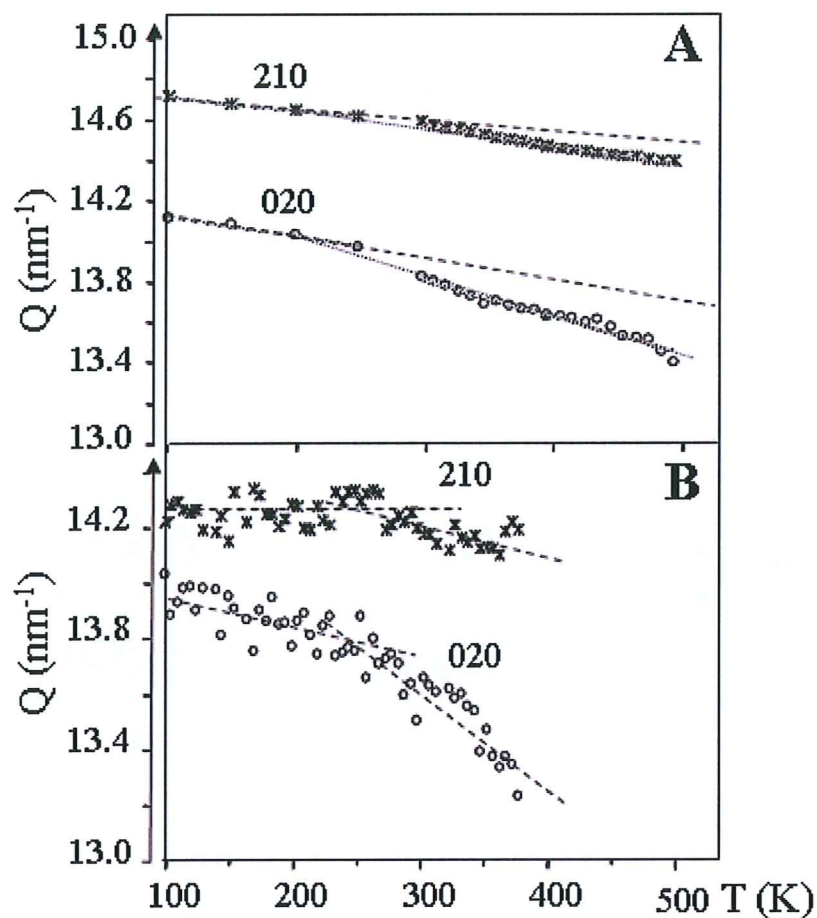


Figure 6: A: evolution of the position of the 210 (black stars) and 020 reflections (white circles) during the *in situ* heating of Greige silk; B: same for fresh cocoon silk. Lines depicted are guide-lines to the eye.

### B- Evolution of crystalline fraction

The sum of intensities of the Bragg peaks ( $\sum I_{Bragg}$ ), corresponding to the crystalline fraction, was separated from the short-range order scattering by fitting Gaussian and polynomial profiles to the sequence of patterns. (see supporting information)  $\sum I_{Bragg}$  remains practically constant during the *in situ* heating experiment up to 500 K. The data points shown in Figure 7 were scaled to the average of the values up to 450 K (=1.0), which will be called a crystallinity index. This shows a high thermal stability of the crystalline fraction. There is notably no evidence for an increase in 210-intensity in this range, which excludes a contribution from the amorphous, random-coil Fibroin to crystalline  $\beta$ -sheet transition at about 463 K.[2, 40] This supports the assumption of a low random-coil volume fraction in *B. mori* silk fibers.[41] At  $\approx 550$  K, the short-range order scattering becomes dominant and only



the strongest equatorial Bragg peaks remain visible. At about 570 K, the equatorial Bragg peaks have disappeared and the short-range order peak has transformed into a more narrow powder ring, which has moved to a larger Q-value. The azimuthally integrated intensity profile of this pattern can be fitted by 3 Gaussian peaks and a 0-order polynomial background, suggesting the presence of residual diffuse halo and two new peaks, which will be discussed below. (Figure 7) The loss in crystalline fraction coincides with a weight loss determined by thermogravimetry and CO<sub>2</sub> liberation due to chain scission determined by evolved gas detection.[42]

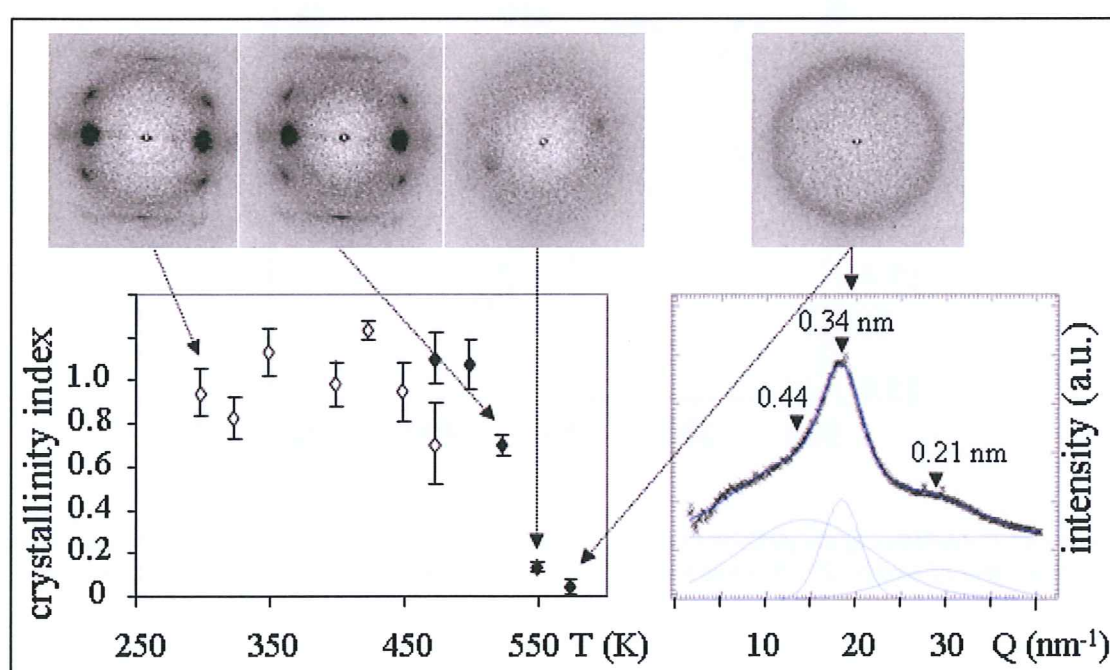


*Figure 7: Evolution of crystallinity index (see text) of the *B. mori* bave with temperature. The data were obtained from silk preheated in a N<sub>2</sub> atmosphere (white diamonds) or in air (black diamonds). The values plotted are averages of the values calculated from 7 to 8 patterns for each fiber. The error bars are the standard deviation of these values. The selected diffraction patterns show the overall degradation. An azimuthally integrated intensity profile shown to the right has been determined for the pattern obtained at the highest temperature and fitted with 3 Gaussian profiles and a 0-order polynomial background. The d-values (nm) of the fitted peaks are indicated.*

### C- Evolution of the amorphous fraction

Figures 8A-C show the evolution of the Gaussian peak attributed to the short-range order fraction with temperature. (see Figure 5D) The peak position remains practically constant up to about 430K and decreases then up to 550 K. (Figure 9A) At about 570 K the sample has turned black and the two new peaks shown in Figure 7 appear with lattice spacing of  $d=0.34$  nm (strong) and  $d=0.21$  nm (weak), overlapping a remaining short-range order peak ( $d=0.44$  nm). This supports carbonization as discussed for wood where the appearance of similar peaks has been attributed to the formation of turbostratic carbon.[43]

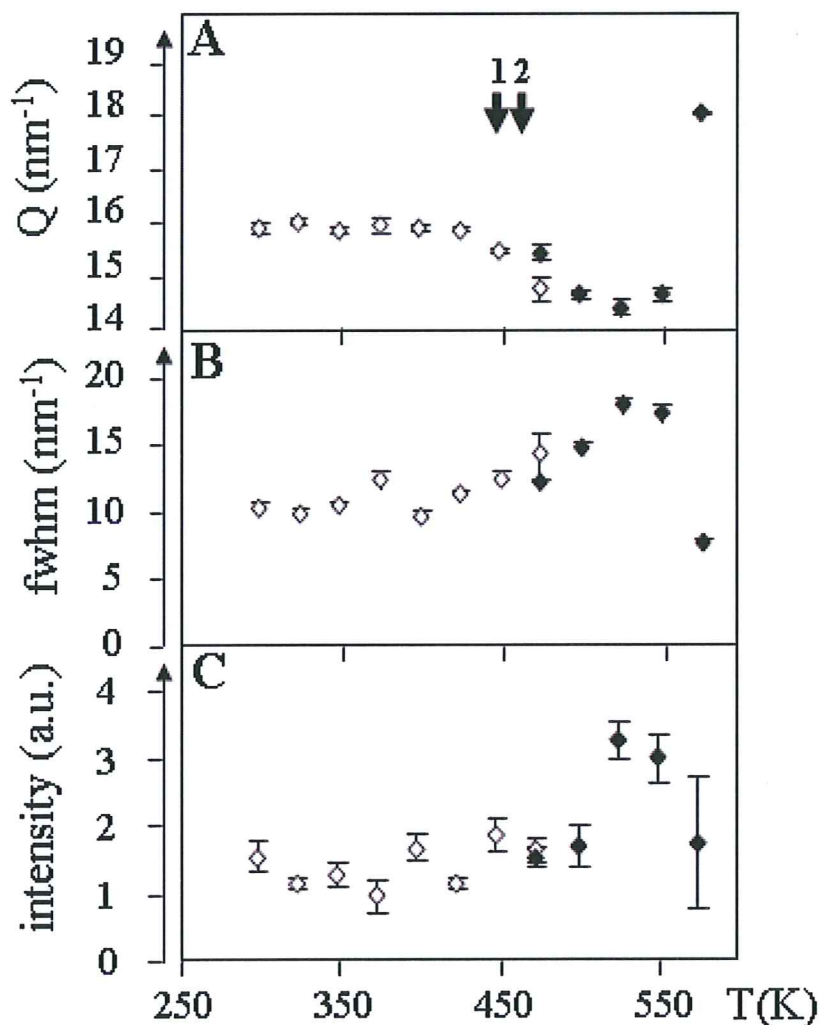


*Figure 8: Evolution of profile parameters of short-range order halo, shown in Figure 5D. The peak was fitted by a Gaussian profile with a polynomial background. A: evolution of peak position; B: evolution of peak width (fwhm); C: evolution of the integrated intensity. The open rhomboids correspond to samples, which were heated in air and the measured at room temperature; the filled rhomboids correspond to samples heated in nitrogen and then cooled to room temperature (see text) The vertical arrows in Figure 8A corresponds to reported glass transitions; 1: ref[2] ,2: ref[3]*

The evolution of the peak width shows an increase in the transition range  $430 < T$  (K)  $< 550$  and then a significant reduction as the new peak is formed at about 570 K. (Figure 8B) The transition range shows also a slight increase in integrated peak intensity. (Figure 8D) The origin of the transition range of  $430 < T$  (K)  $< 550$  could be complex as the glass transition temperature for *B. mori* of 448 K[2] or 463 K[3] and an onset of weight loss[44] fall within this range. A degradation of intermolecular hydrogen bonding has been observed by IR-spectroscopy in the temperature range 423-453 K.[2] This suggests that the decrease of the peak position (Figure 8A) reflects a destruction of  $\beta$ -sheet bonding and hence an increasing [100] interchain distance, preceding carbonization.

#### **D- Protein stability**

The result of protein analysis is shown in Figures 2B. FibH starts to degrade above  $\approx 350$  K. This protein contains the (Gly-Ala) rich sequences, which fold into crystalline  $\beta$ -sheet domains. As the crystal structure survives the molecular degradation (Figure 7), it is reasonable to assume that the degradation is limited to the random chains, connecting the crystalline domains. At 373 K, a degradation product of FibH can be observed as a light band under the native size FibH band, which suggests the existence of a site particularly sensitive to the thermal degradation. (Figure 2B) An SDS-PAGE (5% of acrylamide) without stacking gel suggests a molecular weight of about 305 KDa for the degradation product. This degradation product could be due to one or several cleavages. FibL starts to degrade above about 400 K. This peptidic chain does not contain the (Ala-Gly) rich regions folding into  $\beta$ -sheet domains. It is assumed to be part of the amorphous matrix embedding and linking them together and it is more thermally stable than FibH. It is linked to FibH by a disulfide bond and probably contains numerous hydrogen-bonds that maintain the cohesion of the fiber.

#### **E- Evolution of mechanical properties**

*B. mori* and dragline silks have been classified as protein elastomers.[45] The temperature dependent stress/strain curves of *B. mori* baves heated in a nitrogen atmosphere resemble therefore the transition from an elastomeric to a hard, ductile polymer.[46] (Figure 9)



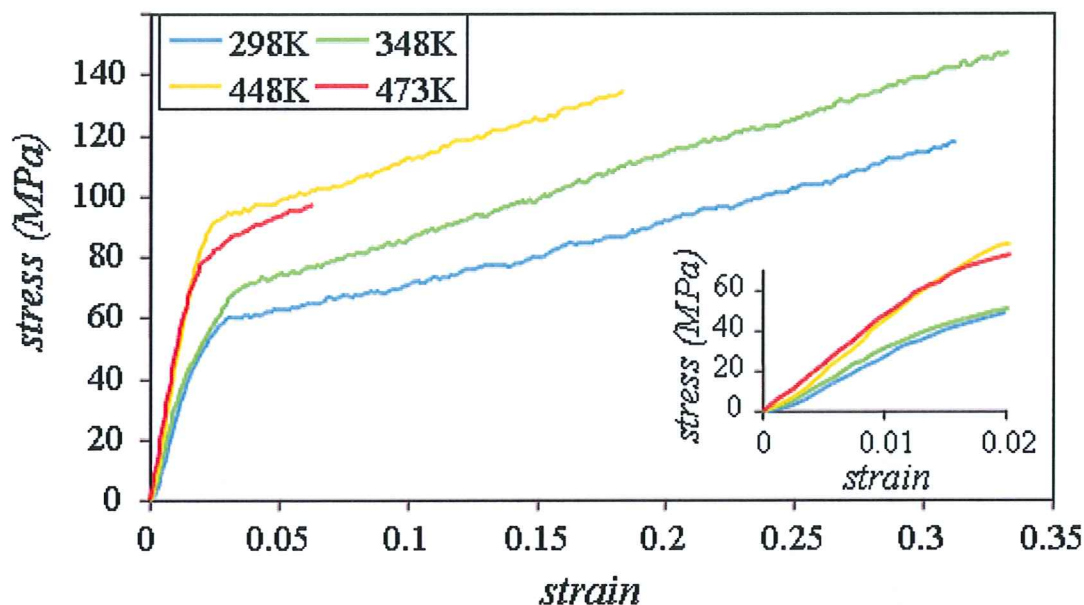
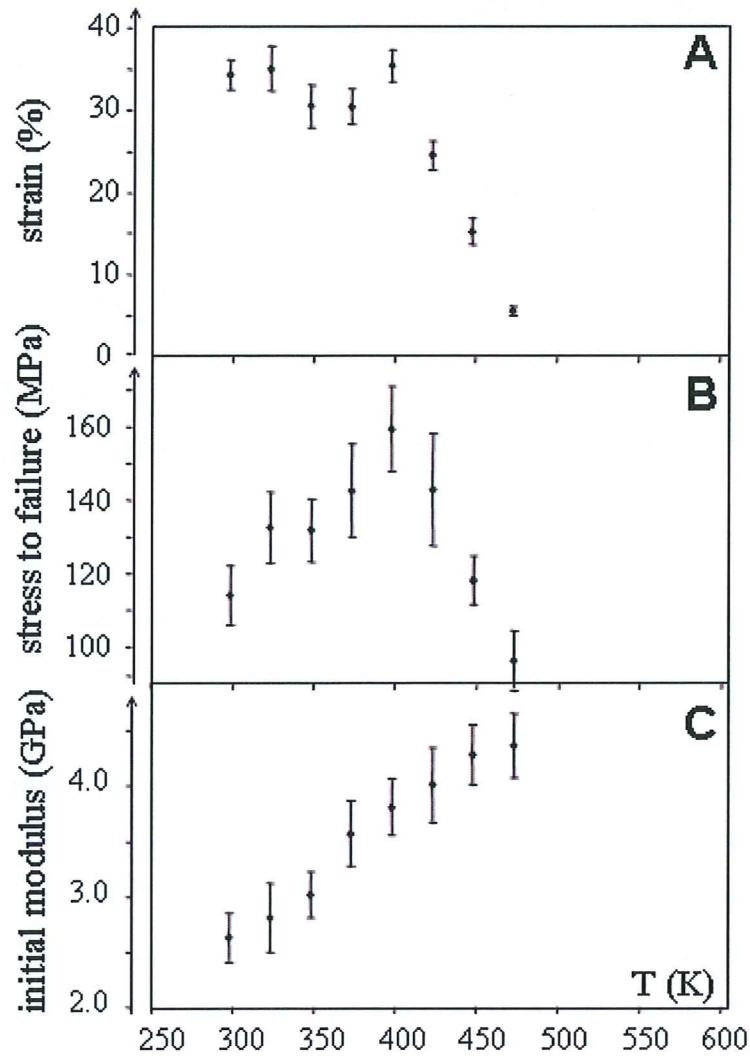


Figure 9: Stress/strain curves of a *Bombyx mori* silk bave after heating in a nitrogen atmosphere (see experimental section).

The linear onset (Figure 9; insert) is attributed in analogy to dragline silk[7, 8] to the deformation of a network of flexible, hydrogen-bonded chains, reinforced by crystalline domains. The decrease of the strain-to-failure for thermal treatments above about 350 K is reflected on the molecular scale by a degradation of the Fibroin proteins. (Figure 2B) A more detailed analysis of the mechanical parameters over a larger temperature range is shown in Figures 10A-C. The room temperature values are similar to values reported in literature.[32] It has, however, been shown that significantly higher mechanical parameters, such as the initial modulus, can be obtained if the cross-section is corrected for the sericin contribution.[47] We note that both strain-to-failure and tensile strength decrease above about 400 K while the modulus continues to rise up to nearly 500 K, which is at the onset of crystallinity decay. (Figure 7) The 400 K limit of stress- and strain-increase corresponds about to the onset of FibL degradation. (Figure 2B) The origin of these changes is located in the amorphous chain fraction as the crystalline domain fraction is not affected. (Figure 7). It is suggested that cross-linking is starting at about 400 K due to chain scission observed by protein analysis, resulting in  $-\text{NH}_2$  and  $-\text{OH}$  end groups. The reaction of these groups could result in cross-linking of neighboring chains. An increasing cross-link density with temperature can explain in analogy to elastomeric polymers[46] the increasing modulus while an increasing density of defects



will reduce the strain and stress-to-failure at the onset of cross-linking. The higher strain-to-failure and lower tensile modulus observed in this study with respect to previous studies can be attributed to the contribution of end effects over such short gauge lengths.



*Figure 10: Evolution of mechanical properties of cocoon silk bave after heat treatment. A: strain-to-failure; B: tensile strength; C: initial modulus. The values plotted are averages of measures from 9 to 15 baves for each temperature. The error bars correspond to the standard deviations of the individual samples divided by the square root of the number of samples.*

## IV- CONCLUSION

The structural data obtained on *Bombyx mori* brins and baves support the model of a network of flexible polymer chains with hydrogen-bonding interactions, reinforced with crystalline  $\beta$ -sheet domains as for dragline silk.[7] A similar model has been proposed for *B. mori* silk based on electron diffraction/imaging[18] and used to model the mechanical properties of dragline silk.[8] The axial aggregation of  $\beta$ -sheet domains via short-range order interface domains into nanofibrils[7] could not be verified but remains possible in view of SAXS[36, 48] and TEM results.[18] A lateral aggregation of  $\beta$ -sheet units through van der Waals bonding is proposed to occur under conditions of drying and vacuum exposure. *B. mori* silk differs therefore from dragline silk by the lack or low amount of a short-range order fraction in the (hypothetical) nanofibrils.

Short-range order sericin scattering has been observed for the first time by SR microdiffraction at the edge of a bave. A small sericin crystallinity and results from other crystallization experiments suggest that single crystal growth and structure analysis of sericin might become possible.

The present results show that the crystalline domains of *B. mori* silk start degrading only above about 500 K, which is comparable to dragline silk.[1] The thermal degradation of FibH and FibL molecules starting already in the range 350-400 K affects thus only the short-range order chain fraction. The mechanical properties such as ultimate tensile stress and strain to failure start to degrade at the onset of the FibH and FibL molecular degradation, suggesting a causal link. This and an increase in Young's modulus up to about 475 K indicate that degradation in the amorphous fraction is accompanied by an increasing cross-linking. The close analogy to elastomeric polymers suggests that models involving molecular springs[49] are not required for describing the mechanical properties.

## Acknowledgement

The authors wish to thank G. Chavancy (Unité Nationale Séricicole, INRA Lyon) for a gift of *B. mori* cocoons, G. Freddi (Stazione sperimentale per la Seta, Milano) for a gift of degummed *B. mori* silk and N. Zafeiropoulos (Dresden) for helpful discussions. We gratefully acknowledge the help provided by L. Terradot-Piot (*Partnership for Structural Biology* unit; Grenoble) with protein electrophoresis experiments, C. Koenig (ESRF) for help with laser microdissection and I. Snigireva (ESRF) for the SEM images.

Supporting Information Available. Specialist batch processing software for analyzing a sequence of diffraction patterns.

## References

1. Glišovic, A. and T. Salditt, *Temperature dependent structure of spider silk by X-ray diffraction*. J. Appl. Phys. A, 2007. **87**(1): p. 63-69.
2. Nakamura, S., J. Magoshi, and Y. Magoshi, *Thermal properties of silk proteins in silkworms*, in *Silk Polymers. Materials Science and Biotechnology*, D. Kaplan, et al., Editors. 1994, American Chemical Society: Washington. p. 211-221.
3. Tsukada, M., et al., *Structural-changes of silk fibers induced by heat-treatment*. Journal of applied polymer science, 1992. **46**(11): p. 1945-1953.
4. Grubb, D.T. and L.W. Jelinski, *Fiber Morphology of Spider Silk: The Effects of Tensile Deformation*. Macromolecules, 1997. **30**(10): p. 2860-2867.
5. Yang, Z., D.T. Grubb, and L.W. Jelinski, *Small-Angle X-ray Scattering of Spider Dragline Silk*. Macromolecules, 1997. **30**: p. 8254 - 8261.
6. Riekkel, C., et al., *Aspects of X-ray diffraction on single spider fibers*. Int. J. Biol. Macrom., 1999. **24**(2-3): p. 187-195.
7. Sapede, D., et al., *Nanofibrillar structure and molecular mobility in spider dragline silk*. Macromolecules, 2005. **38**(20): p. 8447-8453.
8. Termonia, Y., *Molecular Modelling of Spider Silk Elasticity*. Macromolecules, 1994. **27**: p. 7378-7381.
9. Bram, A., et al., *X-ray diffraction from single fibres of spider silk*. J. Appl. Cryst., 1997. **30**: p. 390-392.
10. Takahashi, Y., M. Gehoh, and K. Yuzuriha, *Structure refinement and diffuse streak scattering of silk (Bombyx mori)*. Int. J. Biol. Macrom., 1999. **24**: p. 127-138.
11. Sinsawat, A., et al., *X-ray diffraction and computational studies of the modulus of silk (Bombyx mori)*. Polymer, 2002. **43**: p. 1323-1330.
12. Freddi, F. and M. Tsukada, *Silk Fibers (Grafting)*, in *Polymeric Materials Encyclopedia*, J.C. Salamone, Editor. 1996, CRC Press: Boca Raton. p. 7734-7744.
13. [www.oxfordcryosystems.co.uk/downloads/Cryostream%20Temp%20Profile%20along%20Nozzle.pdf](http://www.oxfordcryosystems.co.uk/downloads/Cryostream%20Temp%20Profile%20along%20Nozzle.pdf).
14. Hammersley, A., *FIT2D-V10.3*, in [www.esrf.fr/computing/scientific/FIT2D/](http://www.esrf.fr/computing/scientific/FIT2D/).
15. Riekkel, C., *New Avenues in X-ray microbeam experiments*. Rep. Prog. Phys., 2000. **63**: p. 233-262.
16. Perrakis, A., et al., *Protein microcrystals and the design of a diffractometer: current experience and plans at EMBL and ESRF/ID13*. Acta Cryst., 1999. **D55**: p. 1765-1770.
17. Schroer, C.G., et al. *Beryllium parabolic refractive X-ray lenses*. 2002: SPIE.
18. Shen, Y., M.A. Johnson, and D.C. Martin, *Microstructural Characterization of Bombyx mori Silk Fibers*. Macromolecules, 1998. **31**: p. 8857-8864.
19. Müller, M., et al., *Microcrystallography with an X-ray waveguide*. J. Appl. Cryst., 2000. **33**: p. 1231-1240.



20. Schoeck, J., et al., *Na-cellulose formation in a single cotton fiber studied by synchrotron radiation microdiffraction*. *Biomacromolecules*, 2007. **8**(2): p. 602-610.
21. Blanton, T.N., et al., *JCPDS-International Centre for Diffraction Data round robin study of silver behenate. A possible low-angle X-ray diffraction calibration standard*. *Powder Diffraction*, 1995. **10**(2): p. 91-95.
22. Davies, R., *A new batch-processing data-reduction application for X-ray diffraction data*. *J. Appl. Cryst.*, 2006. **39**: p. 267-272.
23. Marsh, R.E., R.B. Corey, and L. Pauling, *An investigation of the structure of silk Fibroin*. *Biochim. Biophys. Acta*, 1955. **16**: p. 1-34.
24. Fraser, R.D.B. and T.P. MacRae, *Conformations of Fibrous Proteins*. 1973, New York: Academic Press.
25. Thiel, B.L., D. Kunkel, and C. Viney, *Physical and Chemical Microstructure of Spider Dragline: A Study by Analytical Transmission Electron Microscopy*. *Biopolymers*, 1994. **34**: p. 1089-1097.
26. Ruland, W., *X-ray determination of crystallinity and diffuse disorder scattering*. *Acta Cryst*, 1961. **14**: p. 1180-1185.
27. Burghammer, M., M. Müller, and C. Riekel, eds. *X-ray synchrotron radiation microdiffraction on fibrous biopolymers like cellulose and in particular spider silks*. *Recent Research Developments in Macromolecules*, ed. S.G. Pandalai. Vol. 7. 2003, Research Signpost: Trivandrum, India. 103-125.
28. Somashekar, R., R.G. Urs, and M.S. Madhava, *Crystal size and Distortion Parameter of Natural Pure Mysore Silk Fibers (Bombyx Mori)*. *J. of Appl. Polym. Sci.*, 1992. **44**: p. 2161-2165.
29. Klug, H.P. and L.E. Alexander, *X-ray diffraction procedures for polycrystalline and amorphous materials*. 2<sup>nd</sup> ed. 1974, New York, N.Y.: Wiley Interscience.
30. Roessle, M., et al., *Structural evolution of regenerated silk Fibroin under shear: combined wide- and small-angle X-ray scattering experiments using synchrotron radiation*. *Biopolymers*, 2004. **74**: p. 316-327.
31. Iizuka, E., *Degree of crystallinity and modulus relationships of silk threads from Bombyx mori*. *Biorheology*, 1965. **3**: p. 1-8.
32. Kaplan, D.L., et al., eds. *Silks: Chemistry, Properties and Genetics*. *Biomaterials, Novel Materials from Biological Sources*, ed. D. Byrom. 1991, Stockton Press: New York. 1-53.
33. Kennedy, C.J., K.v. Lerber, and T.J. Wess, *Measuring Crystallinity of Laser Cleaned Silk by X-ray Diffraction*. *e-PRESERVATIONScience*, 2005. **2**: p. 31-37.
34. Nadiger, G.S. and V.G. Halliyal, *Relation between structure and properties of natural silk*. *Colourage*, 1984. **31**(20): p. 23-32.
35. Yanagi, Y., Y. Kondo, and K. Hirabayashi, *Deterioration of Silk Fabrics and Their Crystallinity*. *Textile Research Journal*, 2000. **70**(10): p. 871-875.
36. Londono, J.D., et al., *Morphological Parameters in Varieties of Silk Fibers Determined by Small-Angle X-Ray Scattering*. *J. Appl. Polym. Sci.*, 2002. **85**(11): p. 2382-2388.
37. Knight, D. and C. Riekel, unpublished.
38. Huang, J., et al., *Cloning, Expression, and Assembly of Sericin-like Protein*. *J. Biol. Chem.*, 2003. **278**(46): p. 46117-46123.
39. Cunniff, P.M., et al., *Mechanical properties of major ampulate gland silk fibers extracted from Nephila clavipes spiders*, in *Silk Polymers. Materials Science and Biotechnology*, D. Kaplan, et al., Editors. 1994, American Chemical Society: Washington. p. 234-251.



40. Magoshi, J.M., Yoshiko; Nakamura, Shiego; Kasai, Nobutami; Kakudo, Masao, *Physical Properties and Structure of Silk. V. Thermal Behavior of Silk Fibroin in the Random-Coil Conformation*. Journal of Polymer Science: Polymer Physics Edition, 1977. **15**: p. 1675 - 1683.
41. Yao, J., Y. Nakazawa, and T. Asakura, *Structures of Bombyx mori and Samia cynthia ricini Silk Fibroins Studied with Solid-State NMR*. Biomacromolecules, 2004. **5**: p. 680-688.
42. Tsukada, M., *Thermal Decomposition Behavior of Sericin Cocoon*. J. Appl. Pol. Sci., 1978. **22**: p. 543-554.
43. Saito, Y. and T. Arima, *Cone structure of hexagonal carbon sheets stacked in wood cell lumen*. J. of Wood Science, 2004. **50**(1): p. 87-92.
44. Shirakashi, K., T. Takubo, and Y. Takahashi, Y. Sen-i Kogyo Gakkaishi, 1942. **8**: p. 119.
45. Vollrath, F. and D. Porter, *Spider silk as archetypical protein elastomer*. Soft Matter, 2006. **2**: p. 377-385.
46. Nielsen, L.E. and R.F. Landel, *Mechanical Properties of Polymers and Composites*. Mechanical Engineering, ed. L.L. Faulkner. 1994, New York: Marcel Dekker Inc.
47. Perez-Rigueiro, J., et al., *Mechanical Properties of Single-Brin Silkworm Silk*. J. of Appl. Polym. Sci., 2000. **175**: p. 1270-1277.
48. Miller, L.D., et al., *Investigation of the nanofibrillar morphology in silk fibers by small angle X-ray scattering and atomic force microscopy*. Int. J. Biol. Macrom., 1999. **24**: p. 159-165.
49. Becker, N., et al., *Molecular nanosprings in spider capture-silk threads*. Nature Materials, 2003. **2**: p. 278-283.

---

## Acknowledgments

I thank the many people who helped me during my thesis:

Murielle Salomé, Marine Cotte and Margaret Rak, from ESRF-ID21, who taught me the basics of EXAFS and FTIR spectroscopy.

Harald Müller and Irina Snigireva, from ESRF, who helped me in chemistry and electronic microscopy.

Andrei Fluerasu, Muriel Mattenet and Ray Barrett, from ESRF, for the friendly collaboration that we have around microfluidics.

Laurent Terradot and the ESRF team of the CIBB, who allowed me to use their equipment to prepare Fibroin protein.

Emanuela DiCola, Michael Sztucki and Pierre Panine, from ESRF-ID02, for their support in SAXS.

Jean-Baptiste Salmon, Fanny Destremault and Chloé Masselon who taught me microfluidics.

Above all, I thank ID13 team:

Christian Riekkel who has supervised this thesis. I greatly appreciated his philosophy of suggesting ideas and leaving me all the freedom to experiment and interpret them. He knows how to encourage pluridisciplinarity, and it gives surprising results.

Manfred Burghammer helped me a lot for experiments and data treatment all along these three years. He was an essential support technically and scientifically, but also psychologically.

Richard Davies, who taught me Raman spectroscopy and mechanical tests. His permanent good mood generates a nice working atmosphere.

Lionel Lardière, Manuel Pérez and Hervé Gonzalez, who helped me with setup and technical problems.

Charlotte Vendrely for the shared work on Silk and microfluidics.

Aurélien Gourrier who helped me in writing this manuscript.

Finally, I thank the members of the jury and particularly the reporters for their constructive remarks and their encouragements.

